# First-principles modelling of functional perovskites

A Thesis

Submitted for the Degree of

DOCTOR OF PHILOSOPHY

by

**Shivani Grover**

Research supervisors:
Dr Ricardo Grau-Crespo
Dr Keith Butler

Department of Chemistry
School of Chemistry, Food and Pharmacy
United Kingdom

OCTOBER 2022

**To my parents**

# Declaration

I confirm that this is my own work and the use of all material from other sources has been properly and fully acknowledged.

Shivani Grover

# Acknowledgements

I take this opportunity to thank my supervisors Dr Ricardo Grau-Crespo and Dr Keith Butler for their continuous support and guidance throughout my PhD at University of Reading. I enjoyed intense scientific discussions with them which has always motivated me to pursue new scientific ideas, get involved into it actively and solve it efficiently. I am thankful for their valueable comments and instructions in preparing for seminars and writing papers.

I would like to express my gratitude to my collaborators Gregor Kieslich, Umesh Waghmare, Eduardo Menéndez-Proupin, Ana L Montero-Alejo, A. G. A. Nisbet, Stefan Burger for the interesting and fruitful scientific collaborations, support and insightful suggestions. I have been greatly benefitted from their expertise and learned a lot during discussions.

I am extremely grateful to Felix trust for the doctoral scholarship, and to the supercomputing facilities, ARCHER/ARCHER2, the UK's national high-performance computing service, via the UK's HPC materials chemistry consortium and Young supercomputer, via the UK's materials and molecular modelling hub.

I am thankful to my past and present lab members, Scott, Vikram, Victor, Pablo, Ivan, Katya, Charlotte, Frances for many academic, non-academic and fun interactions at various occassions.

I take this opportunity to thank all my teachers at various stages of education. I thank my grandparents for their unconditional love and support at all stages of life. I have been blessed to have friends like Silvi, Yashica, Auroni, Ishita, Shreekant, Swarna, Meenakshi, and I thank them for their unconditional love and support at all stages of life.

Last but not the least, to the people I owe the most: my parents for their unconditional love, affection and support. To my siblings Garima and Gautam, and brother-in-law Prince for their unconditional love and support at all stages of my life. I have been truly blessed with my family, their unwavering patience, inspiration, constant motivation and belief in me has made this all possible. I will be grateful to them forever. Thank you.

# Abstract

The perovskite structure is common to a wide range of materials which exhibit a rich variety of physical properties, such as ferroelectricity, antiferromagnetism, piezoelectricity, giant magnetoresistance, etc. along with different types of phase transition (metal-insulator, magnetic, ferroelectric and structural transitions). The control of the physical properties of perovskites by varying temperature, pressure, composition, and external fields give rise to novel phases. With continued advances in computational power, algorithms and simulation techniques, computational research has become increasingly effective in understanding and complementing experiments. In particular, density functional theory (DFT) based simulations provide fundamental insights into structural stability and properties of a material under the influence of external stimuli. On the other hand, classical and quantum atomistic modelling of materials helps in the study of their properties at long length and time scales by using molecular dynamics. In this thesis, I use DFT and ab initio molecular dynamics (AIMD) to model functional perovskites. This thesis deals with various types of perovskites based on the kind of atomic/molecular species constituting the perovskite structure and explains the complex interplay between structure and properties in these materials. Starting with an inorganic multiferroic perovskite, $BiFeO_3$, the effect of cobalt doping in $BiFeO_3$ on its structural, electronic, ferroelectric and thermodynamic properties is explored, in the context of potential photocatalytic applications. I present an AIMD investigation of the structural, electronic, vibrational and thermodynamic properties of mixed-cation mixed-anion perovskite solid solution of $FAPbI_3$ and $MAPbBr_3$ for photovoltaic applications. Finally, I study molecular perovskites and the phase transitions observed in them, which can be employed for solid-state refrigeration applications based on the barocaloric effect. The effect of different metal cations on the mechanical properties is calculated, which provides a starting point for rational design of molecular perovskites with strong barocaloric behaviour. This work illustrates the rich diversity in behaviour of perovskite-based materials and how first principles simulations can make substantial contributions to understanding and controlling their functional properties.

# List of Publications

(1) S. Grover, K. T. Butler, U. Waghmare, R. Grau-Crespo. Co-substituted $BiFeO_3$: thermodynamic, electronic and ferroelectric properties from first principles, preprint available on arXiv:2201.11161
Status: Manuscript under review in Advanced Theory and Simulations (2022).

(2) S. Grover*, S. Burger*, K. T. Butler, K. Hemmar, P. Vervoorts, G. Kieslich, R. Grau-Crespo. Tuning the mechanical properties of dicyanamide-based molecular perovskites, manuscript under preparation. *Equal contributions

(3) E. Menéndez-Proupin, S. Grover, A. L. Montero-Alejo, S. D. Midgley, K. T. Butler, R. Grau-Crespo. Mixed-anion mixed-cation perovskite $(FAPbI_3)_{0.875}(MAPbBr_3)_{0.125}$: an ab initio molecular dynamics study, Journal of Materials Chemistry A, **10**, 9592-9603 (2022).

(4) S. Burger*, S. Grover*, K. T. Butler, H. L. B. Boström, R. Grau-Crespo, G. Kieslich. Tilt and shift polymorphism in molecular perovskites, Materials Horizons, **8**, 2444-2450 (2021). *Equal contributions

(5) A. G. A. Nisbet, F. Fabbrizi, S. C. Vecchini, M. Stewart, M. G. Cain, T. Hase, P. Finkel, S. Grover, R. Grau-Crespo, S. P. Collins. Intrinsic and extrinsic nature of the giant piezoelectric effect in the initial poling of PMN-PT, Physical Review Materials, **5**, L120601 (2021).

# Contents

# List of Abbreviations

| | |
|---|---|
| DFT | Density functional theory |
| AIMD | Ab initio molecular dynamics |
| NREL | National renewable energy laboratory |
| HOIP | Hybrid organic inorganic perovskite |
| LDA | Local density approximation |
| GGA | Generalized gradient approximation |
| PAW | Projector augmented wave |
| DFPT | Density functional perturbation theory |
| BEC | Born effective charge |
| CPMD | Car-Parrinello molecular dynamics |
| BOMD | Born-Oppenheimer molecular dynamics |
| VASP | Vienna ab initio simulation package |
| PCE | Power conversion efficiency |
| PSC | Perovskite solar cell |
| PBE | Perdew Burke Ernzerhof |
| SOD | Site occupancy disorder |
| SQS | Special quasi-random structure |
| PDF | Pair distribution function |
| VDOS | Vibrational density of states |
| LD | Lattice dynamics |
| LFSE | Ligand field stabilisation energy |
| ML | Machine learning |
| GULP | General utility lattice program |

# Chapter 1

# Introduction

The discovery of functional materials that exhibit exotic properties and can be grown easily is one of the driving forces to accelerate technological growth. With the increasing energy demand, environmental degradation and climate change associated with the usage of non-renewable resources, there is an utmost need to develop new materials which allow harvesting clean affordable alternative energies. Developments in computing resources and algorithms based on quantum mechanics, allows us to predict new materials with desired functionalities, as well as their response to external stimuli. First-principles density functional theory (DFT) [1,2] (see Chapter 2) has evolved as a powerful tool that is widely used in condensed matter theory and materials science for the calculation of structural, electronic, vibrational and magnetic properties of solids with reliable accuracy. DFT provides fundamental insights into the structural stability and properties of a material under the influence of an external stimuli. To study the properties of materials at long length and time scales (temperature-dependent transition properties, phase transitions), classical or quantum atomistic modelling through use of Monte Carlo simulations [3] (with a first-principles based effective Hamiltonian) or ab initio molecular dynamics (AIMD) [4] can be used. The objective of this thesis is to study various functionalities of perovskite materials and engineer their properties using first-principles DFT and molecular dynamics. The impressive range of structure and property interplay of perovskite materials makes

them an excellent research field for materials science, physics and solid state chemistry. This chapter begins with a brief introduction to perovskite materials.

The discovery of calcium titanate ($CaTiO_3$) in 1839 by the Russian mineralogist L. A. Perovski marked the origin of perovskite materials. In a conventional perovskite oxide structure with the chemical formula $ABO_3$, A is divalent ($A^{2+}$) cation, B is tetravalent ($B^{4+}$) cation and O is oxide ($O^{2-}$). Other combinations of oxidation states are possible for perovskite oxides, as long as the sum of the oxidation states of the cations is six: *e.g.* III-III in most ferrite perovskites like $BiFeO_3$, or solid-solution II-(V,II) perovskites like $PbMg_{1/3}Nb_{2/3}O_3$. In this thesis, I will meet these inorganic oxides, as well as other perovskites with different cations and anions. The $BO_6$ octahedra form a corner-sharing network and A cation sits in the cuboctahedral cavity (Figure 1.1). The ideal symmetry of a perovskite is cubic with space group $Pm\bar{3}m$ as shown in Figure 1.1. The high-symmetry cubic perovskite structure is inherently unstable and typically appears as a dynamical average structure at high temperatures.

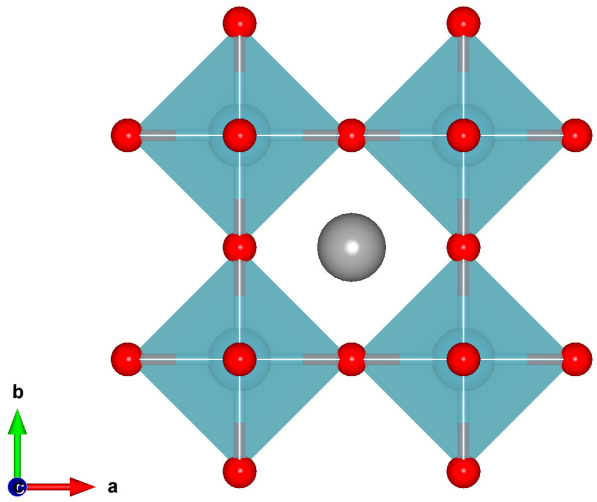


Figure 1.1: Unit cell of a $CaTiO_3$ perovskite in cubic phase ($Pm\bar{3}m$). The crystal coordinates are taken from Ref. [5]. Colour scheme: Ca: Grey, Ti: Blue, and O: Red.

At low temperatures, perovskites are prone to distortion, and the nature of the lower-symmetry crystal structure can be predicted on the basis of a tolerance factor (Eq. 1.1). Goldschmidt's tolerance factor ($t$) is an indicator for the stability and distortion of crystal

structures [6]. It is a dimensionless number that is calculated from the ratio of the ionic radii:

$$t = \frac{r_A + r_O}{\sqrt{2}(r_B + r_O)} \tag{1.1}$$

where $r_A$ is the radius of A cation, $r_B$ is the radius of the B cation and $r_O$ is the radius of the anion. The ideal cubic perovskite is observed at room temperature in perovskites with $t \approx 1$, *e.g.* $SrTiO_3$ [7]. Table 1.1 shows various perovskite symmetries possible depending on the tolerance factor. The distortions from the ideal cubic structure can be attributed to the following mechanisms:

- Distortions of the octahedra
- Displacements of the cations within the octahedra
- Octahedral tilting

The first two mechanisms are driven by electronic instabilities of the octahedral metal ion (B cation). For instance, the Jahn-Teller distortion observed in $KCuF_3$ [8] is an example of an electronic instability that leads to octahedral distortions. The ferroelectric perovskite $BaTiO_3$ [9, 10] is an example of an electronic instability (pseudo Jahn-Teller effect [11]) that leads to cation displacement (displacement of Ti atoms). There has been significant research on understanding the distortion in perovskites, whereby they have been classified based on the polyhedral volumes of the A and B cation [12, 13], which is useful when both cation displacement and octahedral tilting occur simultaneously. The most common distortion mechanism is the octahedral tilting, which is a tilting of the $BO_6$ octahedra keeping the corner-sharing connectivity. When an octahedron in the perovskite structure is tilted in a particular direction, it causes tilting of the neighbouring octahedra. This type of distortion is observed at lower $t$ values when the A cation is too small for the cubic $BO_3$ corner-sharing octahedral network.

Table 1.1: Perovskite structure and the corresponding tolerance factor [14, 15].

| $t$ | Structure | Explanation | Example |
|---|---|---|---|
| >1 | Hexagonal/ Tetragonal | A ion too big or B ion too small | $BaNiO_3$, $BaTiO_3$ ($t$ =1.0617) |
| 0.9-1 | Cubic | A and B ions have ideal relative sizes | $SrTiO_3$ |
| 0.71-0.9 | Orthorhombic/ Rhombohedral | A ions is too small or B ion is too big | $GdFeO_3$(Orthorhombic), $CaTiO_3$(Orthorhombic) |
| ∼0.71 | Different structures | A and B have similar ionic radii | Ilmenite, $FeTiO_3$ (Trigonal) |

The work by Glazer [16] contains a complete description of all possible octahedral tilt systems existing in perovskite materials. The tilts are indicated symbolically by a set of three letters referring to the axes in the order [100], [010], [001], which in general case of unequal tilts is denoted as *abc*. Equality of tilts is denoted by repeating the same letter, *e.g. aac* means equal tilts about [100] and [010] with a different tilt about [001]. A superscript is used to indicate zero-tilt (0), in-phase tilt (+) or anti-phase tilt (-) of subsequent layers of octahedra. For instance, the cubic structure is represented as $a^0a^0a^0$, tetragonal as $a^0a^0c^+$ or $a^0a^0c^-$ and orthorhombic as $a^+b^-b^-$ or $a^+a^-a^-$ or $a^0b^-b^-$. The octahedral tilting in [100] direction leads to orthorhombic symmetry in $CaTiO_3$ [5, 17] and trifold tilting of octahedra leads to hexagonal symmetry. There are 23 possible tilt systems leading to different symmetry space groups, a complete list of these can be found in Ref. [16].

These structural distortions, cation displacements and octahedral tilts are of interests because they have important effects on the physical properties of perovskite compounds, particularly their electronic, ferroelectric and magnetic properties. The diversity in perovskite compositions and structures leads to various functional properties such as (anti)ferroelectricity [10, 18], (anti)ferromagnetism [19], piezoelectricty [20, 21], colossal magnetoresistance [22], charge and orbital ordering [23].

Based on the kind of A, B and X ions, perovskites can be primarily divided into three classes:

- Inorganic perovskites

- Hybrid organic-inorganic perovskites
- Molecular perovskites

A brief introduction to each of them is given below.

## 1.1 Inorganic perovskites

In inorganic perovskites, A and B are inorganic metal ions and X is a charge balancing anion. The area of inorganic perovskites is a broad and growing field due to their technologically-relevant properties such as ferroelectricity (as observed in $BaTiO_3$ [9,10]), piezoelectricity (as observed in $PbZr_xTi_{1-x}O_3$ [18]), colossal magnetoresistance [22], non-linear optics (as observed in $LiNbO_3$ [24, 25]). The coupling between orbital, lattice and spin degrees of freedom in these perovskites makes them interesting, both at fundamental and applied perspectives. In this context, perovskite multiferroics, which exhibit coupled electric, magnetic and/or structural order parameters in the same structural phase are of fundamental interest. A brief description of ferroelectricity and ferromagnetism is given below.

Ferromagnetic materials undergo a phase transition from a high-temperature paramagnetic phase (where the magnetic dipole moments of atoms are randomly aligned) to a low-temperature ferromagnetic phase (which exhibits a non-zero spontaneous magnetisation in the absence of magnetic field). These magnetic dipole moments are aligned parallel to each other for a ferromagnet, but can also be aligned anti-parallel to each other in what is called an antiferromagnet. A ferroelectric material exhibits a phase transition from a high-temperature paraelectric phase (an ordinary dielectric) to a low-temperature ferroelectric phase that has a spontaneous polarisation whose direction can be switched by an applied electric field. In perovskite ferroelectrics, there is a structural distortion to a lower-symmetry phase accompanied by the off-centre shifting of the A cation (as in $BiFeO_3$ [19]) or the B cation (as in $BaTiO_3$ [9]), below the Curie temperature. The spontaneous polarisation derives largely from this shift.

A multiferroic material exhibits two or more "ferro" properties (ferroelectricity, ferromagnetism, and/or ferroelasticity) in the same phase. The coupling between the magnetic and ferroelectric order parameter gives rise to magnetoelectric effects, where the magnetisation can be tuned by applied electric field and vice versa. These materials present opportunities for potential applications in information storage, spintronics, and sensors. There has been very active recent research on multiferroic perovskites, for instance, $YMnO_3$ (antiferromagnetic ferroelectric in hexagonal phase [26, 27] used in non-volatile memory devices [28]), $BiMnO_3$ (ferromagnetic ferroelectric in monoclinic phase [29–31] used in data storage [32] and spintronics [33]) and $BiFeO_3$ (antiferromagnetic ferroelectric in rhombohedral phase [19]). In the present thesis, I focus on bismuth ferrite perovskite which is the most widely studied multiferroic as it exhibits a ferroelectric Curie temperature $T_c$ of 1103 K, and an AFM Néel temperature $T_N$ of 643 K, making it a promising room-temperature multiferroic [19], with potential applications in data storage, spin valves, spintronics and sensors [34]. The ferroelectric property of $BiFeO_3$ can be exploited for effective separation of oppositely charged photogenerated charge carriers, making it suitable for photovoltaic and photocatalytic applications. A brief introduction to the principles of photocatalysis is given later in the chapter. The band gap of $BiFeO_3$ in its rhombohedral ground state is a bit too wide for visible-light photocatalysis. In Chapter 3, I discuss routes to engineer this band gap via $BiCo_xFe_{1-x}O_3$ solid solutions whilst conserving the ferroelectric properties.

In the same context, piezoelectric materials, which can generate electric field/charges by subjecting to a mechanical force (direct piezoelectric effect), or exhibit a mechanical strain under an applied electric field (converse piezoelectric effect) are important for numerous applications, *e.g.*, ultrasonic medical imaging, underwater acoustics and actuators etc. Relaxor ferroelectrics such as $Pb(Mg_{1/3}Nb_{2/3}O_3)$-$x$$PbTiO_3$ (PMN-PT), a solid-solution of relaxor $Pb(Mg_{1/3}Nb_{2/3}O_3)$ (PMN) and ferroelectric $PbTiO_3$ (PT), shows a giant piezoelectric response across the morphotropic phase boundary and thus has potential applications in capacitors and piezoelectric devices [35,36]. The term morphotropic

phase boundary refers to the phase transition between the tetragonal and the rhombohedral ferroelectric phases as a result of changing the composition or by applying mechanical pressure. In this thesis (end of chapter 3), I will attempt to explain the tetragonal to monoclinic phase transition in PMN-PT, which is accompanied by a giant piezoelectric response. This part of my work was in collaboration with Dr. Gareth Nisbet (at Diamond Light Source, Didcot) who performed the experiments.

## 1.2 Hybrid organic-inorganic perovskites

Hybrid organic-inorganic perovskites (HOIP) includes an organic cation such as $CH_3NH_3^+$ ($MA^+$, methylammonium cation), $HC(NH_2)_2^+$ ($FA^+$, formamidinium cation) at the A site, an inorganic metal at the B site ($Pb^{2+}$, $Sn^{2+}$) and a halogen ($F^{-1}$, $Cl^{-1}$, $Br^{-1}$, or $I^{-1}$) or an organic anion $(CHOO)^{-1}$, $(C_2N_3)^{-1}$ at the X site. Since the organic cation must fit into the cuboctahdedral cage formed by the $BX_6$, the selection of organic molecules for the A site is limited. An estimate based on the tolerance factor for a cubic perovskite ($t = 1$) with B cation as $Pb^{2+}$ ($r_{Pb} = 1.19$ Å) and X anion as $I^{-1}$ ($r_I = 2.20$ Å) [37], gives that the radius of the A cation should be $\sim 2.6$ Å. Given that C-C or C-N bond lengths are of order 1.4 Å, the organic molecules consisting of two or three atoms will fit into the perovskite structure, making the $MA^+$ cation an appropriate choice for the HOIP structure. In fact, the most widely studied HOIP is methylammonium lead iodide (MAPI) due to its high power conversion (photon to current) efficiency of ∼19.3% [38]. MAPI exhibits useful optoelectronic properties such as high carrier mobility, long carrier diffusion lengths [39, 40], high absorption coefficients and widely tunable band gap (from 1.5 to 2.3 eV) [41,42]. HOIPs are easy to synthesise from solution based methods enabling cost-effective and scalable production with remarkable optoelectronic properties [43].

However, a limitation on large-scale commercialization of these HOIP in photovoltaic industry is imposed by the inherent material instability. $MAPbI_3$ films are known to be quite sensitive to moisture causing decompositon into lead iodide and methylamine iodide,

leading to fast device degradation [44, 45]. The mixed-cation HOIP, where the A-site is randomly occupied by a combination of different cations, *e.g.* $MA^+$, $FA^+$ or the inorganic $Cs^+$, show improvement in stability whilst maintaining the power conversion efficiency [46]. In Chapter 4, an initio molecular dynamics study of the mixed-cation mixed-halide perovskite $(FAPbI_3)_{0.875}(MAPbBr_3)_{0.125}$ is presented. The structural, thermodynamic and vibrational properties are calculated and compared with the pure compounds $FAPbI_3$ and $MAPbBr_3$.

## 1.3 Molecular perovskites

The use of molecular ions at both the A and X sites leads to new geometric and structural degrees of freedom. The use of molecular X-site anions increases the size of the $BX_6$ octahedra, such that molecular A-site cations with varying compositions and sizes can be used to form these molecular perovskites. The use of molecular moieties has important ramifications for the perovskite properties. For instance, molecular A-site cations enable the temperature and pressure dependent order-disorder phase transitions related to the disorder of the molecular A cation [47, 48]. In Chapter 4, I study the structural and thermodynamic properties of molecular perovskite series $[(nPr)_3(CH_3N)]M(C_2N_3)_3$ with M = Mn, Co, Ni, nPr = n-propyl and $(C_2N_3)^-$ = dicyanamide ion, and connect my results to the experiments performed by Dr. Gregor Kieslich's group (at Technical University of Munich, Germany). Using this molecular perovskite series (with M = Mn, Co, Fe, Ni, Zn, Cd, Ba, Sr, Ca, Hg, or Mg) as a model system, I study the effect of the $M^{2+}$ metal species on the mechanical properties via lattice dynamics calculations. A relationship between geometric factors and mechanical properties that agree with chemical intuition is observed which allows us to contribute to the long-term goal, the rational design of materials with targeted macroscopic properties.

## 1.4 Applications of perovskites

In this section, I briefly discuss some of the applications of perovskites studied in this thesis. I focus on photocatalytic, photovoltaic, and barocaloric applications, which are relevant to the work presented in chapters 3, 4 and 5, respectively.

### 1.4.1 Perovskite materials for photocatalysis

The solar water splitting is an uphill and nonspontaneous reaction because the Gibbs free energy is positive, 237.3 kJ/mol under standard temperature and pressure [49]. Photocatalytic water splitting reaction involves excitement of electrons from the valence band (VB) to conduction band (CB) by absorption of a photon of energy greater than the band gap ($E_g$) of the material. The generated electrons and holes migrate to the surface. The water molecules get oxidised by holes to give oxygen gas (oxygen evolution reaction, OER) and protons. The protons then get reduced by electrons to give hydrogen gas (hydrogen evolution reaction, HER).

$$\begin{aligned} H_2O &\longleftrightarrow 2H^+_{(aq)} + \frac{1}{2}O_{2(g)} + 2e^- \quad \text{(OER)} \\ 2H^+_{(aq)} + 2e^- &\longleftrightarrow H_{2(g)} \quad \text{(HER)} \end{aligned} \tag{1.2}$$

The overall water splitting reaction is shown schematically in Figure 1.2. When using a single-semiconductor photocatalyst for the water splitting reaction, the conduction band minimum (CBM) should be more negative than the redox potential of $H^+/H_2$ (0 V vs. normal hydrogen electrode (NHE)) and the valence band maximum should be more positive than the redox potential of $O_2/H_2O$ (1.23 eV vs. NHE). Thus, the minimum band gap to drive water splitting is 1.23 eV. However, the band gap and band alignment requirements are different for other photocatalytic set ups, like Z-schemes, tandem photolectrochemical cells, etc. A more detailed discussion of these requirements will be given in Chapter 3, in the context of our study on $BiFeO_3$. In addition to the appropriate band alignment, a good photocatalyst material should be:

- a good absorber of light to generate electron-hole pairs;
- capable of carrier separation;
- stable in water;
- inexpensive and non-toxic.

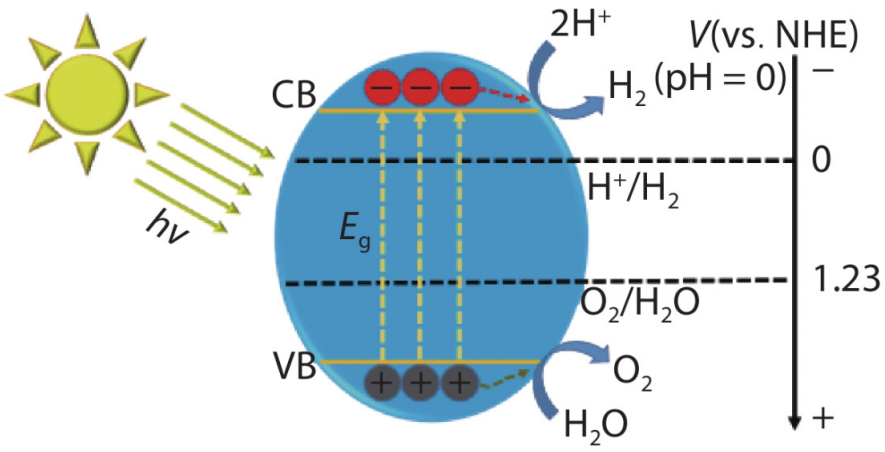


Figure 1.2: Schematic representation of overall water splitting reaction on a semiconductor. Reproduced with permission from Ref. [50].

Perovskite materials can be used as photocataysts for water splitting as some of the perovskites have suitable band structure that are favourable for either half reaction or the overall water splitting reaction. The flexible compositions and constituent elements in A or B site offer electronic structure and band gap engineering. The electronic structure of a perovskite photocatalyst can be engineered by substitution and doping. For instance, Rh-doped $SrTiO_3$ can be used for visible light photocatalysis [51]. The band gap of $SrTiO_3$ (3.2 eV) is reduced by doping Rh at the Ti site, resulting in $H_2$ evolution under visible light irradiation. Some of the perovksites have ferroelectric and/or piezoelectric properties which can further enhance their photocatalytic abilities by promoting effective charge separation [52,53]. For instance, introducing a ferroelectric perovskite material ($BaTiO_3$) in $TiO_2/BaTiO_3$ heterojunctions is a potential strategy to improve photoelectrochemical cell performance [54].

### 1.4.2 Perovskite materials for photovoltaic solar cells

The rapid increase in the power conversion efficiency (PCE) of perovskite solar cells (PSC) has made them a rising star in the photovoltaic industry. Figure 1.3 (taken from the national renewable energy laboratory (NREL) solar cell efficiency chart) demonstrates the efficiencies achieved with perovskite-based devices over recent years, in comparison to various other photovoltaic technologies. The graph shows a spectacular rise for perovskites based solar cells compared to other photovoltaic technologies over a relatively short period of time. In 2020, perovskite based solar cells reached PCE of 25.5 %, which is comparable to silicon-based solar cells.

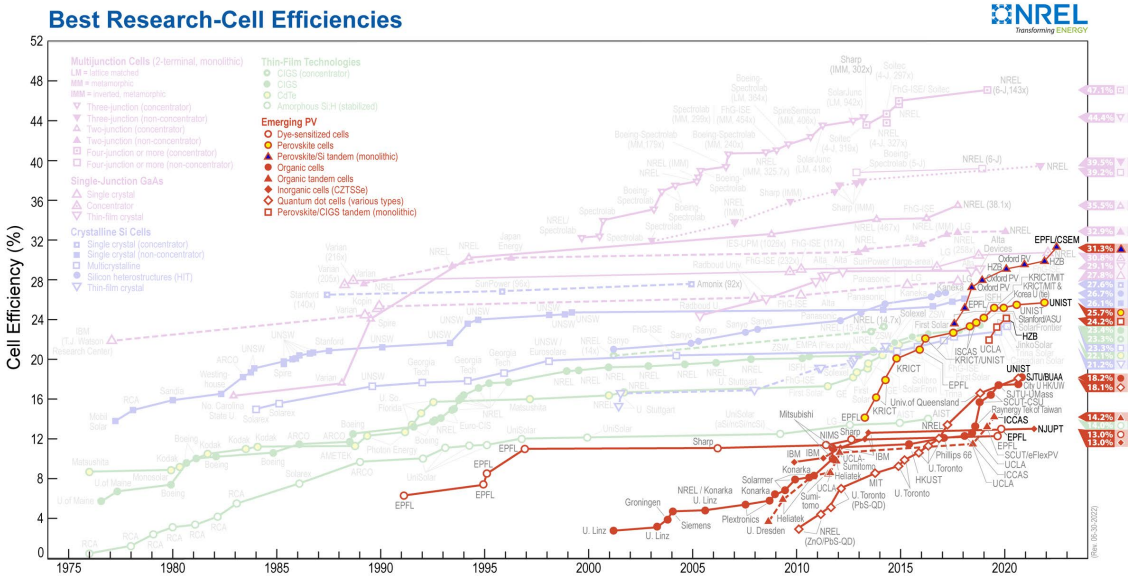


Figure 1.3: PCE of solar cells over years for a range of photovoltaic technologies. This figure is taken from Ref. [55].

Typically, a PSC consists of five parts and can be classified into two types depending upon the arrangement of the electron transport layer (ETL) and hole transport layer (HTL), where the electrons and holes are injected into: $n-i-p$ (conventional) or $p-i-n$ (inverted) structure (Figure 1.4). The function of ETL is to enable efficient electron collection and transportation from the perovskite layer to its respective electrodes. The most commonly used ETL is $TiO_2$ as it has a band alignment that favours transfer of electrons. Perovskites are used as the light-absorbing layer that creates excitons or free

carriers. Lastly, there is a counter electrode (gold, silver or carbon) to ensure an ohmic contact.

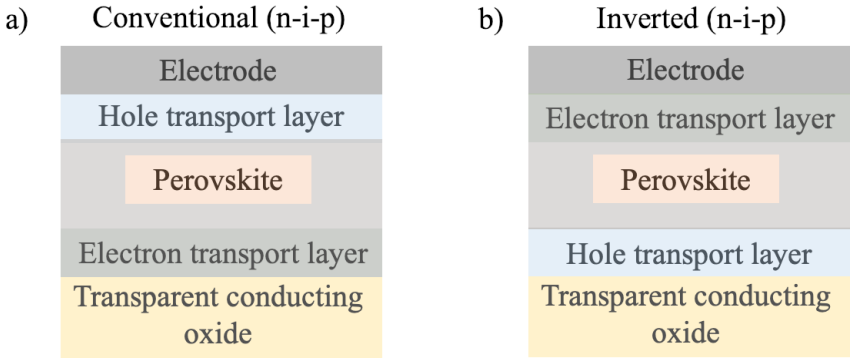


Figure 1.4: Schematic representation of a) conventional, and b) inverted perovskite based solar cells

The first use of a HOIP as a light absorber for solar cell dates back to 2009 by Kojima *et al.* [56]. HOIPs feature low-cost solution-based processability and excellent optoelectronic properties. They exhibit a high absorption coefficient of $10^5$ $cm^{-1}$ in the visible wavelength range [57], low exciton binding energy (∼20 meV) [58], and a finely tunable bandgap [59]. In order to enhance the device performance and structural stability, cation and halide substitution are a convincing approach. A variety of possible HOIPs employed for photovoltaic applications and their corresponding PCE parameters is nicely tabulated in Ref. [60].

### 1.4.3 Perovskite materials for barocalorics

Materials with large solid-state caloric effects induced by external field (mechanical, electric or magnetic field) are needed for the development of eco-friendly solid-state refrigeration technologies [61, 62]. The refrigeration capacity is associated with a large isothermal entropy change or with a large temperature change induced by external stimuli, such as mechanical stress-namely, uniaxial strain (elastocaloric effect) [63] or hydrostatic pressure (barocaloric effect) [64] or electric field (electrocaloric effect) [65, 66] or magnetic field (magnetocaloric effect [67]), effects that are enhanced near to phase transitions [61, 68].

The presence of organic moieties in molecular perovskites enhance their chemical diversity, structural richness and flexibility, giving rise to novel multi-functional properties. Molecular perovskite [TPrA][Mn(dca)$_3$] (TPrA = tetrapropylammonium cation, $(CH_3CH_2CH_2)_4N^+$; dca = dicyanamide anion, $[N(CN)_2]^-$) exhibits a giant barocaloric effect (*i.e.* a large isothermal entropy change driven by applied pressure) near room temperature and under easily accessible pressure (P<70 bar) [68]. [TPrA][Mn(dca)$_3$] shows a phase transition from polymorph I to polymorph II at $T_t \sim 330$ K, accompanied by a large entropy change ($\Delta S$), see Figure 1.4 taken from Ref. [68].

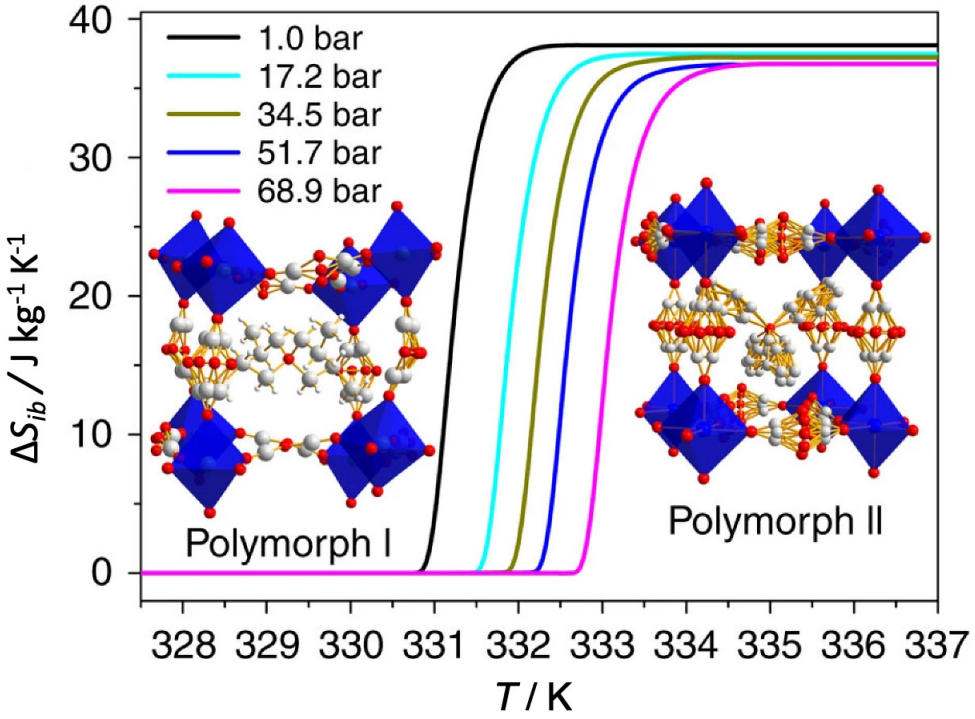


Figure 1.5: Isobaric entropy change as a function of temperature in the low pressure range, related to the first-order phase transition from polymorph I or II. Reproduced with permission from Ref. [68]

The phase transition temperature ($T_t$) gets progressively displaced towards higher temperature when increasing pressure. This variation of $T_t$ with pressure gives the barocaloric coefficient ($\delta T_t/\delta P$). The entropy curves shift towards higher temperatures as pressure increases. The associated barocaloric effect for this material can then be defined as the isothermal entropy change induced by hydrostatic pressure. A similar giant reversible barocaloric effect in $[(CH_3)_4N]Mn[N_3]_3$ near its cubic-monoclinic structure transition has

also been reported [69]. Thus, molecular perovskites offer new interesting opportunities for the solid-state cooling applications due to promising barocaloric effects.

## 1.5 Overview of the thesis

The overall objective of this thesis is to understand the functional behaviour of a range of perovskites from a knowledge of their crystal and electronic structures, via quantum mechanical calculations. The perovskites studied here are of fundamental importance and exhibit various technological applications. The chapters of the thesis are organised based on the kind of perovskites explored for various technological applications and we connect our results to experiments wherever possible. After a brief introduction to the work here, I give an overview of methods and formalism used in this thesis in Chapter 2.

In Chapter 3, I present a detailed analysis on electronic, ferroelectric and thermodynamic properties $BiCo_xFe_{1-x}O_3$ solid solutions, with $0 < x < 0.13$, using density functional theory. I also discuss the potential of this perovskite solid solution in visible-light photocatalysis by computing the band alignment and comparing it with the redox potentials for water-splitting. The later sections of this chapter focuses on the phase transitions observed in relaxor ferroelectric PMN-PT accompanied with a giant piezoelectric response.

In Chapter 4 and 5, I focus on HOIPs and molecular perovskites respectively. In Chapter 4, I present an AIMD investigation of the structural, thermodynamic and vibrational properties of the mixed-cation mixed-anion perovskite $(FAPbI_3)_{0.875}(MAPbBr_3)_{0.125}$. In Chapter 5, I focus on a new series of molecular perovskite and study its structural, thermodynamic and mechanical properties.

Finally, I summarise this thesis in Chapter 6 and present an outlook to opportunities for future work.

# Chapter 2

# Methods and Formalism

The interactions between electrons, between nuclei, and between electrons and nuclei, determine the ground state and excited state properties of atoms, molecules, thin-films, surfaces and bulk materials. Most physical properties can be determined by calculating the first and second derivatives of total energy, which is the sum of many-electron quantum ground state energy and classical electrostatic nuclear interaction energy. For example, first derivatives of energy with respect to atom positions, strain and magnetic field gives forces, stress and magnetisation, and their second derivatives gives inter-atomic force constants, elastic constants and magnetic susceptibility, respectively. The main problem lies in determination of the quantum mechanical ground state of the many-electron system. In this context, the development of DFT proposed by Walter Kohn [1, 2], which maps an interacting electron system to a system of independent electrons within an effective potential, has lead to significant advances in the theoretical study of the material properties with remarkably good agreement with experiment.

In this chapter, I briefly discuss the theoretical background and the computational methods employed in this thesis. Section 2.1-2.6 gives a formal description for calculating the total energy as prescribed within the DFT. The linear response theory used to determine the response of a system to external perturbation is described in Section 2.7. It further describes the frozen phonon method to calculate vibrational frequencies. For

real physical systems, atoms are in constant motion and their trajectories are of practical interest. Therefore, the time and temperature dependence ($T > 0$ K) of atomic motion needs to be taken into account to calculate dynamic properties of the system. We briefly discuss AIMD methods at the end of this chapter (Section 2.9).

## 2.1 First-principles methods

The Hamiltonian of a system of interacting electrons and nuclei is given by:

$$\hat{H} = -\frac{\hbar^2}{2m_{\mathrm{e}}}\sum_i \nabla_i^2 - \sum_{i,I}\frac{Z_I e^2}{|r_i - R_I|} + \frac{1}{2}\sum_{i\neq j}\frac{e^2}{|r_i - r_j|} - \sum_I \frac{\hbar^2}{2M_I}\nabla_I^2 + \frac{1}{2}\sum_{I\neq J}\frac{Z_I Z_J e^2}{|R_I - R_J|} \quad (2.1)$$

where $\hbar$ is Planck's constant, $m_{\mathrm{e}}$ and $M_I$ are the masses of electron and the $I^{\mathrm{th}}$ nucleus respectively, $e$ is electronic charge, and $Z_I$ is the atomic number of the $I^{\mathrm{th}}$ nucleus. $r_i$ and $R_I$ are the position vectors of the $i^{\mathrm{th}}$ electron and $I^{\mathrm{th}}$ nucleus respectively. The first and the third term of Equation 2.1 represent the kinetic ($T_{\mathrm{e}}$) and potential energies ($V_{\mathrm{ee}}$) of electrons respectively, fourth and fifth terms are the kinetic and potential energies of nuclei respectively. The Coulomb interaction energy between nuclei and electrons is included in the second term, which acts like an external potential ($V_{\mathrm{ext}}$) to the electronic system. Thus, one can determine the ground state properties of a system by solving a time-independent Schrödinger equation:

$$\hat{H}\psi(R, r) = \epsilon\psi(R, r) \quad (2.2)$$

where $\epsilon$ and $\psi$(R,r) are the eigenvalue and the corresponding eigenfunction of the system. Since, the mass of the nuclei ($M_I$) is significantly larger than the mass of electron ($\frac{M_I}{m_e} \simeq 1836$), the kinetic energies of the nuclei are small and can be ignored. Thus, the time scales associated with the motion of the nuclei are much slower than those associated with the electrons. The electrons and nuclei are decoupled within this approximation, called as the *Born-Oppenheimer approximation*. The many-body wavefunction can now

be written as a product of electronic and nuclear wavefunction.

$$\psi(R,r) = \chi(R)\phi(R,r) \tag{2.3}$$

Substituting Eq. 2.1 and Eq. 2.3 in Eq. 2.2,

$$\Big[\frac{-\hbar^2}{2m_e}\sum_i \nabla_i^2 - \sum_{i,I}\frac{Z_I e^2}{|r_i - R_I|} + \frac{1}{2}\sum_{i\neq j}\frac{e^2}{|r_i - r_j|} + \frac{1}{2}\sum_{I\neq J}\frac{Z_I Z_J e^2}{|R_I - R_J|}\Big]\phi(R,r) = E(R)\phi(R,r) \tag{2.4}$$

and

$$\Big[-\sum_I \frac{\hbar^2}{2M_I}\nabla_I^2 + E(R)\Big]\chi(R) = \epsilon\chi(R) \tag{2.5}$$

$$\begin{aligned} E[\phi] &= \frac{\Big\langle \phi \Big| \hat{H}_{\mathrm{e}} \Big| \phi \Big\rangle}{\big\langle \phi | \phi \big\rangle} \\ \hat{H}_e &= \hat{T} + \hat{V}_{\mathrm{ee}} + \hat{V}_{\mathrm{ext}} \end{aligned} \tag{2.6}$$

The ground state wavefunction or the lowest energy state $\phi_0(r)$ is determined by finding the minimum of total energy (Eq. 2.6) with all the parameters defining $\phi(r)$, with the constraint that $\phi$ must obey the particle anti-symmetry and conservation laws. The Born-Oppenheimer approximation hence reduces the problem to solving for the electronic ground state (Eq. 2.4) for a given set of nuclei positions. However, for a system with $N_{\mathrm{e}}$ number of electrons, $\phi(R,r)$ is a many body wavefunction which cannot be solved exactly, and hence further approximations have to be employed to solve the many body Hamiltonian.

## 2.2 Hohenberg and Kohn theorems

The work of Hohenberg-Kohn in 1964 [1], and Kohn-Sham in 1965 [2] led to the formulation of the DFT, a theory of correlated many-body systems. Hohenberg and Kohn proposed two theorems to formulate the DFT as an exact theory for ground state of many-body fermionic systems.

**Theorem I**

*For any system of interacting particles in an external potential $V_{\text{ext}}(r)$, the potential $V_{\text{ext}}$ is determined uniquely, except for a constant, by the ground state particle density $n_0(r)$. Therefore all properties of the system are completely determined if $n_0(r)$ is known.*

**Theorem II**

*A universal functional for the energy $E[n]$ in terms of the density can be defined for any external potential $V_{\text{ext}}(r)$. For any particular $V_{\text{ext}}(r)$, the exact ground state energy of the system is the global minimum value of this functional, and the density $n(r)$ that minimises the functional is the ground state density $n_0(r)$.*

These two theorems reduce the number of variables of a function from $3N$ to 3 variables (in $n(r)$). As the total energy is a *functional* of ground state electron density, the theory is known as *density functional theory.* The total energy functional is given by,

$$E_{\text{HK}}[n] = T[n] + E_{\text{ee}} + \int dr V_{\text{ext}}(r) n(r) \tag{2.7}$$

where, $T[n]$ and $E_{\text{ee}}[n]$ are the kinetic and potential energies of interacting electron system. These theorems by Hohenberg and Kohn make a significant contribution towards calculating the ground state energy by reducing the minimization problem from $3N$ to 3 dimension. However, these theorems do not provide a practical scheme for determining the ground state electron density or energy of an interacting electron system. Kohn and Sham proposed an ansatz to determine the ground state energy density $n_0(r)$.

## 2.3 Kohn-Sham ansatz

In Kohn-Sham formalism [2], an interacting many-body system is mapped onto a fictitious non-interacting system with same ground state energy density. The ground state density

of electrons in the Kohn-Sham formalism is given as:

$$n(r) = \sum_{\sigma} n(r,\sigma) = \sum_{\sigma} \sum_{i=1}^{N^{\sigma}} \phi_i^{\sigma *}(r)\phi_i^{\sigma}(r) \tag{2.8}$$

The total energy can be written as,

$$\begin{aligned} E_{\mathrm{KS}} &= T_s[n] + \frac{1}{2}\int dr dr' \frac{n(r)n(r')}{|r-r'|} + \int dr V_{\mathrm{ext}}(r)n(r) + E_{\mathrm{xc}}[n] \\ &= T_s[n] + E_{\mathrm{Hartree}}[n] + \int dr V_{\mathrm{ext}}(r)n(r) + E_{\mathrm{xc}}[n] \end{aligned} \tag{2.9}$$

where $E_{\mathrm{Hartree}}$ and $E_{\mathrm{xc}}$ are the Hartree and exchange-correlation energies. $T_s$ is the non-interacting kinetic energy of electrons. The Kohn-Sham non-interacting single particle Hamiltonian is,

$$\begin{aligned} \hat{H}_{\mathrm{KS}} &= -\frac{\hbar^2}{2m_e}\nabla^2 + V_{\mathrm{KS}}(r), \text{where} \\ V_{\mathrm{KS}}(r) &= V_{\mathrm{Hartree}}(r) + V_{\mathrm{ext}}(r) + V_{\mathrm{xc}}[n(r)] \end{aligned} \tag{2.10}$$

The Kohn-Sham equation:

$$\hat{H}_{\mathrm{KS}}\phi_i = \epsilon_i \phi_i \tag{2.11}$$

can be solved to self-consistency as illustrated in Figure 2.1.

The exchange-correlation interaction ($E_{\mathrm{xc}}$) is defined as the difference between the exact energy and the energy from the Hartree model, *i.e.* it contains all non-classical contributions to the electron-electron interaction.

$$E_{\mathrm{xc}}[n(r)] = T[n(r)] - T_s[n] + E_{\mathrm{ee}}[n] - E_{\mathrm{Hartree}} \tag{2.12}$$

The exact form of the exchange-correlation energy functional is not known and is approximated as a local or non-local functional of energy density. These approximations are discussed below.

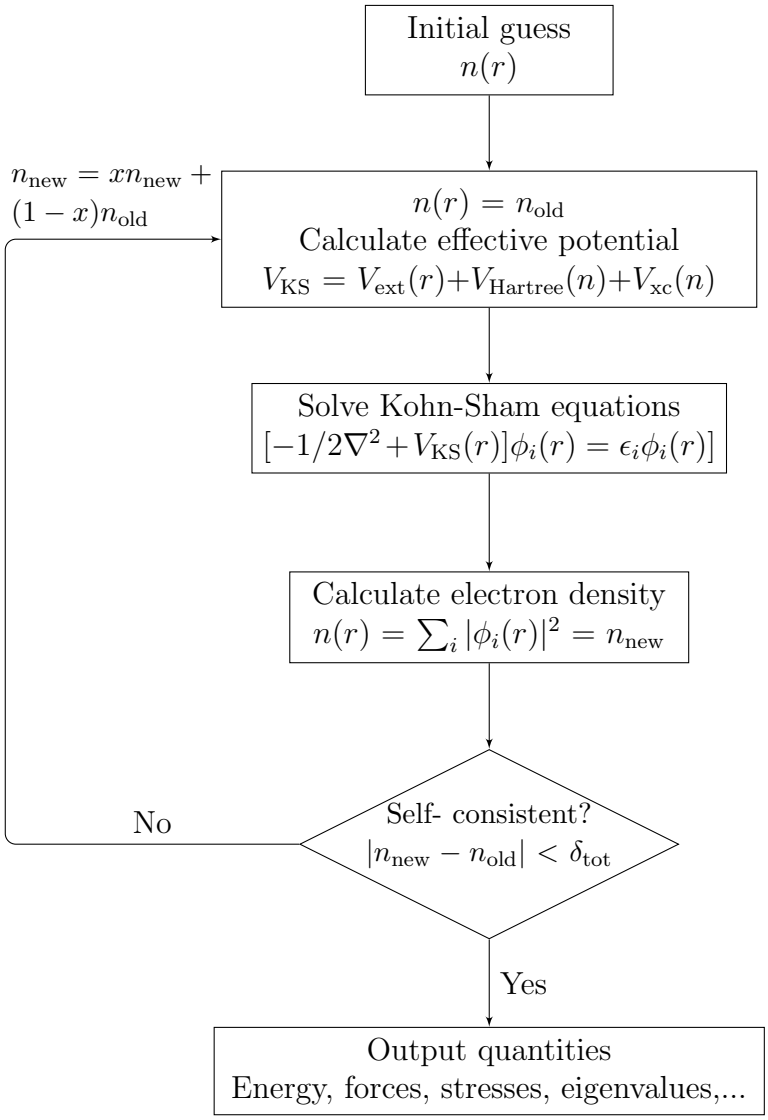


Figure 2.1: Flow chart showing self-consistency loop for the iterative solution of Kohn-Sham equations.

*Local density approximation* (LDA): In this approximation, the exchange-correlation energy density at each point is the same as that of a homogeneous electron gas of the same density

$$E_{\text{xc}}^{\text{LDA}} = \int drn(r)\epsilon_{\text{xc}}^{\text{homo}}(n(r)) \tag{2.13}$$

where $\epsilon_{\text{xc}}^{\text{homo}}(n(r))$ is the exchange-correlation energy per particle of a homogeneous electron gas of density $n(r)$ [2]. However, the corrections to the exchange-correlation energy arising from inhomogeneities in the electron density about $r$ are ignored, LDA describe

many of the properties of weakly correlated systems like semiconductors and homogeneous electron gas fairly well. It fails when charge density changes very abruptly (*e.g.* for molecules).

For inhomogeneous charge densities, the *Generalized gradient approximation* (GGA) is used [70], which includes the information on the spatial variation in the electron density. It overcomes the limitations of LDA by considering the dependence of $\epsilon_{\rm xc}$ on charge density as well as its gradient.

$$E_{\rm XC}^{\rm GGA} = \int drn(r)\epsilon_{\rm XC}(n(r), \nabla n(r)) \tag{2.14}$$

The GGA functional by Perdew, Burke and Ernzerhof (PBE) [70] is the most widely used functional to simulate periodic materials with DFT as it features no empirical fitting parameters. A modification of PBE is the PBEsol [71] functional, which is often used to calculate equilibrium properties of bulk solids and their surfaces. The revised PBE (revPBE) [72] functional is an extension of the PBE functional with some extra fitting parameters and is typically used to simulate liquids, *i.e.* water. Most DFT calculations reported in the present thesis were performed using the PBE functional.

*Hybrid functionals*: It includes a portion of exact exchange from Hartree-Fock (HF) theory with exchange and correlation of DFT, where the exact exchange energy functional is expressed in terms of the Kohn-Sham orbitals rather than density. Hybrid functionals have further improved results than the GGA functionals. In the present thesis, I have used Heyd-Scuseria-Ernzerhof (HSE) functional [73] to determine electronic structures and band gaps. The HSE functional uses an error function screened Coulomb potential to calculate the exchange portion of the energy.

$$E_{\rm XC}^{\rm HSE} = aE_{\rm X}^{\rm HF}(\omega) + (1-a)E_{\rm X}^{\rm PBE,SR}(\omega) + E_{\rm X}^{\rm PBE,LR}(\omega) + E_{\rm C}^{\rm PBE} \tag{2.15}$$

where $a$ is the mixing parameter, $\omega$ is an adjustable parameter controlling the extent of short-range interactions, $E_{\rm X}^{\rm HF,SR}(\omega)$ is the short-range Hartree-Fock exact exchange

functional, $E_{\mathrm{X}}^{\mathrm{PBE,SR}}(\omega)$ and $E_{\mathrm{X}}^{\mathrm{PBE,LR}}(\omega)$ are the short and long range components of the PBE exchange functional, and $E_{\mathrm{C}}^{\mathrm{PBE}}(\omega)$ is the PBE correlation functional. For $\omega = 0$ the HSE exchange-correlation functional reduces to the PBE0 hybrid functional. For most systems, $a = \frac{1}{4}$ and $\omega = 0.2$ (referred to as HSE06), gives accurate results.

## 2.4 DFT with periodic boundary conditions

In the preceding sections, the many-body Hamiltonian is mapped onto an effective single-particle Hamiltonian, making approximations to the electron-electron interaction terms. However, for a solid material, there are effectively an infinite number of electrons in the static potential of an infinite number of nuclei. The translation periodicity of the crystalline solid reduces this to the consideration of one unit cell with periodic boundary conditions, which is explained in the following subsections.

### 2.4.1 Bloch theorem

F. Bloch [74] proved that the solutions of Schrödinger equation for a periodic potential is of the form:

$$\psi_k(r) = u_k(r)e^{ik.r} \tag{2.16}$$

where $u_k(r)$ has the period of the crystal lattice with $u_k(r) = u_k(r + T)$. Here $T$ is the translation vector of the lattice. The wavefunction of a free electron has the form of a plane wave $\psi \sim e^{ik.r}$. The eigenfunctions of the wave equation for a periodic potential are the product of a plane wave $e^{ik.r}$ times a function $u_k(r)$ with the periodicity of the crystal lattice. A monoelectronic wavefunction of the form (Eq. 2.16) is called a Bloch wavefunction. This function can be expanded as any function that is periodic in three dimensions, as a Fourier series in the form:

$$u_k(r) = \sum_G c_{k,G}\ e^{iG.r} \tag{2.17}$$

where the $G$ vectors represent the points in the reciprocal lattice, defined by the condition $e^{iG.T} = 1$. Thus, the wavefunction with index $k + G$ is identical to one wavefunction with index $k$. Therefore, our problem reduces to finding solutions only for the values of $k$ in one unit cell in the reciprocal space, *i.e.*, within the first Brillouin zone.

### 2.4.2 Basis sets

To solve Kohn-Sham equations, a basis set is needed to expand the Kohn-Sham wavefunctions. The most commonly used basis sets are plane waves, atomic orbitals or a combination of both (plane waves + atomic orbitals). In this thesis, I used plane wave basis set. Due to the simplicity and absence of Pulay forces, plane wave basis is widely used for the description of single particle wavefunctions ($\phi_i$) in metals or semiconductors. The Kohn-Sham wavefunction in the plane wave basis is expanded as follows:

$$\phi_i(r) = \sum_{|G|<G_{\text{cut}}} C_{i,(k+G)} e^{i(k+G).r} \tag{2.18}$$

where $G$ is the reciprocal lattice vector and $k$ is the Bloch wavevector. This expansion is infinite in principle and hence needs to be truncated to make it computationally feasible. A kinetic energy cutoff is used to truncate the set of $G$ vectors. Thus, the reciprocal vectors satisfy the condition:

$$\frac{\hbar^2}{2m_e}|k + G|^2 \leq E_{\text{cut}} = \frac{\hbar^2 G_{\text{cut}}^2}{2m_e} \tag{2.19}$$

The value of $E_{\text{cut}}$ is determined by converging total energy with $E_{\text{cut}}$.

## 2.5 Pseudopotentials

The electrons that are tightly bound to the nucleus are called core electrons and have highly localized wavefunctions that oscillate rapidly in space. The core electrons do not take part in chemical bonding. Valence and semi-core electrons are not tightly bound to

nuclei and actively take part in chemical bonding. For an all-electron DFT calculation, one would require a very large number of plane waves for an accurate description of the core states, making it computationally expensive. A *pseudopotential* is thus used, which replaces the potential of core electrons and nucleus of an atom with a hypothetical potential to avoid the explicit treatment of core electrons. Pseudopotentials are constructed by considering a cutoff radius ($r_c$) beyond which the pseudo-wavefunction matches exactly with the true wavefunction [Figure 2.2].

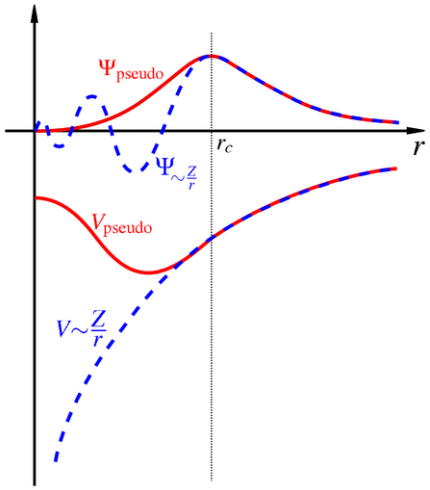


Figure 2.2: Schematic representation of an all electron potential (dotted line) and pseudopotential (solid line) along with corresponsing wavefunctions [75].

If the charge of each pseudo-wavefunction is equal to the charge of actual wavefunction in the region $r < r_c$, the pseudopotential is known as norm-conserving pseudopotential [76]. Outside the core, the pseudo-wavefunction and all electron wavefunction are identical. Ultrasoft pseudopotential includes an augmented charge inside the core region to conserve the total charge while making the potential smooth [77]. Ultrasoft pseudopotentials are computationally more efficient, and maintains the accuracy and transferability.

The information about the core electrons is lost in the pseudopotential method which can be probed by several experimental techniques. The projector augmented wave (PAW) method combines ideas from the pseudopotential method and from the all-electron linear augmented plane-wave (LAPW) method. In the PAW method [78,79], the rapidly oscillating wavefunctions are transformed into smooth wavefunctions providing a way to calculate

all-electron properties from the smooth wavefunctions. It is an all electron method which provides the full wavefunctions, and the potential is determined from the full charge densities. This method is used in performing first-principles molecular dynamics simulations.

## 2.6 Dispersion corrections

Dispersion forces, also referred to as van der Waals (vdW) forces, can be classically visualised as the instantaneous interaction between dipoles induced by charge fluctuations [80,81]. The vdW interactions between atoms and molecules decay rapidly with the distance between interacting particles (as $-1/R^6$) and play an important role in many chemical systems. These interactions are missing in the standard exchange-correlation functional used in DFT and are important to properly describe weakly bonded materials or the adsorption of molecules on surfaces. In recent years, several methods have been developed to include these dispersive interactions in DFT calculations. These interactions are divided into two classes, (1) adding the dispersion interaction as semi-empirical corrections on top of existing local functionals, and (2) to develop non-local exchange-correlation energy functionals that can incorporate vdW interactions [82, 83]. In this thesis, I have used the parametrised DFT-D2 scheme of Grimme [84, 85] for accurate treatment of dispersion interactions at relatively low computational cost. Here, the $\mathrm{E_{disp}}$ is simply added to $\mathrm{E_{KS-DFT}}$ as explained in the first class. The total energy with dispersion correction is given as:

$$E_{\mathrm{DFT-D2}} = E_{\mathrm{KS-DFT}} + E_{\mathrm{disp}} \tag{2.20}$$

where $E_{\mathrm{KS-DFT}}$ being the self-consistent Kohn-Sham energy and $E_{\mathrm{disp}}$ is the empirical dispersion correction given as,

$$E_{\mathrm{disp}} = -s_6 \sum_{i=1}^{N_{at}-1} \sum_{j=i+1}^{N_{\mathrm{at}}} \frac{C_6^{ij}}{R_{ij}^6} f_{\mathrm{damp}}(R_{ij}) \tag{2.21}$$

where $N_{\mathrm{at}}$ are the number of atoms in the system, $C_6$ denotes the dispersion coefficient

for atom pair $(i, j)$, $s_6$ is a global scaling factor that depends only on the approximate functional used in KS-DFT, and $R_{ij}$ is the interatomic distance. To avoid double counting for small $R_{ij}$ (dispersion interactions are already included in the DFT result at very small distances), a damping function ($f_{\text{damp}}$) is used, given as,

$$f_{\text{damp}} = \frac{1}{1 + e^{-d(R_{ij}/R_r - 1)}} \tag{2.22}$$

where $R_r$ is the sum of atomic van der Waals radii and the parameter $d$ determines the dispersion corrections to the total energy and is fixed to 20 by Grimme to give accurate dispersion energies, but still maintaining negligible energies for typical covalent bonding situations. The dispersion coefficient $C_6^{ij}$ for a given pair of atoms $i$ and $j$, is the geometric mean of the individual coefficient.

$$C_6^{ij} = \sqrt{C_6^i C_6^j} \tag{2.23}$$

## 2.7 Phonons

Phonons are collective vibrations of atoms/ions in a crystal. Within the Born-Oppenheimer approximation, the electrons remain in their ground state, and hence the total energy is a function of ionic positions, $E(\{R_I\})$. To determine phonons from first-principles, the most-common approaches are: (1) the frozen-phonon method, and (2) density functional perturbation theory.

### 2.7.1 Frozen phonon approach

In the frozen phonon approach, the total energy and/or forces are calculated by displacing the atoms (*i.e.*, freezing the atomic displacements). The potential energy of the system

on Taylor expansion in $u$ is given by,

$$V = V_0 + \sum_{I,\alpha} \frac{\partial E}{\partial R_{I,\alpha}}\Big|_{u=0} u_{I\alpha} + \frac{1}{2} \sum_{I,J,\alpha,\beta} \frac{\partial^2 E}{\partial R_{I,\alpha} \partial R_{J,\beta}}\Big|_{u=0} u_{I\alpha} u_{J\beta} + O(u^3) \tag{2.24}$$

where, $u_I$ is the displacement of the $I^{\text{th}}$ atom from its equilibrium position ($R_I^0$). At the equilibrium position, forces acting on the atoms are zero, thus, the second term of the Eq. 2.24 is zero. Ignoring the constant terms $V_0$ and $O(u^3)$, force constant matrix $K_{IJ,\alpha\,\beta}$ is given as:

$$\begin{aligned} V &= \frac{1}{2} \sum_{I,J,\alpha,\beta} \frac{\partial^2 E}{\partial R_{I,\alpha} \partial R_{J,\beta}}\Big|_{u=0} u_{I\,\alpha} u_{J\,\beta} \\ &= \frac{1}{2} \sum_{I,J,\alpha,\beta} K_{I\alpha,J\beta}\, u_{I\alpha} u_{J\beta} \end{aligned} \tag{2.25}$$

Solving the equation of motion for harmonic oscillator,

$$M_I \frac{\partial^2 u_{I\alpha}}{\partial t^2} = -\sum_{J,\beta} K_{I\alpha,J\beta} u_{J\beta} \tag{2.26}$$

assuming the time dependence of $u_{I\alpha}$ to be,

$$u_I(t) = u_I e^{i\omega t} \tag{2.27}$$

$$\omega^2 M_I \hat{u}_{I\alpha} = \sum_{J,\beta} K_{I\alpha,J\beta} \hat{u}_{J\beta} \tag{2.28}$$

Solving the above eigenvalue equation, gives phonon frequencies ($\omega$) and eigenvectors ($\hat{u}$). For a given $N$ atom system, the force constant matrix is $3N \times 3N$ dimensional and there will be $3N$ normal mode frequencies. The structural stability of a crystal is determined by the value of the phonon frequencies.

(1) $\omega^2 > 0$, the system is stable, the excitation of any phonon mode with frequency $\omega$ increases the energy of the system.

(2) $\omega^2 < 0$, system is unstable, a finite amplitude of unstable phonon mode results in

lowering of the total energy of the structure.

To determine phonons at $q \neq 0$ ($q$ being phonon wavevector) using the frozen phonon method, we have to consider large supercells commensurate with the $q$-vector and obtain the full phonon dispersion. Thus, it is computationally expensive to compute phonons at $q \neq 0$ with the frozen phonon method. Density functional perturbation theory is a technique which overcomes this drawback of the frozen phonon method.

### 2.7.2 Density functional perturbation theory

Density functional perturbation theory (DFPT) is a linear response theory to compute response functions (physical properties such as force, stress, phonons, dielectric constant and Born effective charges) as the second derivative of total energy with respect to external perturbation ($\lambda_i$). The first and second derivatives of energy are:

$$\begin{aligned} \frac{\partial E}{\partial \lambda_i} &= \frac{\partial E_{\text{ion}-\text{ion}}}{\partial \lambda_i} + \int dr \frac{\partial V_{ext}(r)}{\partial \lambda_i} n(r) \\ \frac{\partial^2 E}{\partial \lambda_i \partial \lambda_j} &= \frac{\partial^2 E_{\text{ion}-\text{ion}}}{\partial \lambda_i \partial \lambda_j} + \int dr \frac{\partial^2 V_{\text{ext}}(r)}{\partial \lambda_i \partial \lambda_j} n(r) + \int dr \frac{\partial n(r)}{\partial \lambda_i} \frac{\partial V_{\text{ext}}(r)}{\partial \lambda_j} \end{aligned} \tag{2.29}$$

To obtain $\partial n(r)/\partial \lambda_i$, we linearize Eq. 2.8

$$\Delta n(r) = 2Re \sum_{i=1}^{N_e/2} \phi_i^*(r) \Delta \phi_i(r) \tag{2.30}$$

Variation in Kohn-Sham wavefunction can be evaluated by solving first-order perturbation theory:

$$(H_{\text{KS}} - \epsilon_i)|\Delta \phi_i\rangle = -(\Delta V_{KS} - \Delta \epsilon_i)|\phi_i\rangle \tag{2.31}$$

where $\Delta \epsilon_i = \langle \phi_i | \Delta V_{KS} | \phi_i \rangle$ is the first-order variation in Kohn-Sham eigenvalues. The change in Kohn-Sham effective potential is given as:

$$\Delta V_{\text{KS}}(r) = \Delta V_{\text{ext}}(r) + e^2 \int dr' \frac{\Delta n(r')}{|r - r'|} + \int dr' \frac{\partial^2 V_{\text{xc}}(r)}{\partial n(r) \partial n(r')} \Delta n(r') \tag{2.32}$$

The response of the electron density to external perturbation depends on the coupling between occupied and empty electronic states, Eq. 2.31 can thus be defined in terms of empty states as,

$$(H_{\mathrm{KS}} - \epsilon_i)|\Delta\phi_i\rangle = -\hat{P}_{empty}\Delta V_{KS}|\phi_i\rangle \tag{2.33}$$

where $\hat{P}_{\mathrm{empty}}$ is the projection onto the empty states manifold and is defined as,

$$\hat{P}_{\mathrm{empty}} = 1 - \hat{P}_{\mathrm{occ}}; \hat{P}_{\mathrm{occ}} = \sum_{i=1}^{N_e} |\phi_i\rangle\langle\phi_i| \tag{2.34}$$

By solving the set of linear equations (Eq. 2.31 and 2.33), one can calculate relevant response properties of the system efficiently and with reasonable accuracy. $K_{I\alpha,J\beta}$ can be evaluated using DFPT by calculating the second derivative of total energy with respect to atomic displacements. The calculations of phonon frequencies at arbitrary $q$-vectors can be performed using DFPT without introducing supercells.

## 2.8 Polarisation

A ferroelectric material is characterised by a spontaneous polarisation whose direction can be switched by an applied electric field. For finite systems such as molecules, the polarisation is determined from the dipole moment $d$, provided that the molecule carries no net charge. The dipole moment, $d$, of a collection of charges, $q_i$, at positions $r_i$ is defined as:

$$d = \sum_i q_i r_i \tag{2.35}$$

However, calculation of the spontaneous polarisation in a periodic solid is not straightforward. Even for the simplest case of one-dimensional chain of alternating cations and anions $\pm q$ (Figure 2.3), the direction of polarisation depends on the choice of unit cell. The multi-valued polarisation is a consequence of the periodicity of the solid. Within the modern theory of polarisation [86], the multivaluedness of polarisation is solved by considering the change in polarization between the polar and non-polar phases which is

uniquely defined for the system. While the absolute value of polarisation in a periodic solid is multi-valued, the change in polarisation is single-valued and well defined. The change in polarisation can be described as:

$$\Delta P = P(1) - P(0) = \int_0^1 d\lambda \frac{dP}{d\lambda} \tag{2.36}$$

where $\lambda$ is a parameter that describes adiabatic change in the structure [87]. For polar materials $\lambda = 1$, and $\lambda = 0$ for the non-polar phase. Thus, the spontaneous polarisation is the difference in polarisation between the final (polarised) and initial (unpolarised) states. For a given crystal system, the total polarisation can be calculated as a sum of ionic and electronic contributions. The ionic contribution is obtained by summing the product of the position of each ion in the unit cell (with a given choice of basis vectors) with the nominal charge of the ionic core. The electronic contribution to the polarisation is calculated as a geometric phase or Berry phase of the electronic Bloch wavefunctions. A complete description on the Berry phase method can be found in Ref. [88].


Figure 2.3: One dimensional chain of alternating cation and anion. The dashed lines show two representative unit cells.

The amount of charge that effectively contributes to the polarisation of the system during the displacement of ions, called the *Born effective charge* (BEC), is calculated as change in polarisation divided by the amount that ion is displaced. BEC is a tensor quantity and its diagonal elements are typically larger than the formal charge of the ion. The BEC tensor for atom $j$, ($\mathrm{Z}^*_{j,\alpha\beta}$) is defined as the derivative of the polarisation $P$ with respect to the atom coordinates (at zero electric field):

$$Z^*_{j,\alpha\beta} = \left.\frac{\partial P_\alpha}{\partial u_{j,\beta}}\right|_{\epsilon=0} \tag{2.37}$$

where $\alpha$ and $\beta$ are Cartesian indices.

## 2.9 Molecular dynamics

For real systems, the natural motion of atoms at finite temperature, and their trajectories are of practical interest. Studying the dynamics of atoms is useful in various fields of science, *i.e.* materials science, condensed matter physics, biophysics, chemical physics, statistical mechanics, etc. In this section, I provide a brief introduction to molecular dynamics theory used to compute equilibrium and thermodynamic properties of system at finite temperature.

The dynamics of the system, characterised by the wave function $\Psi(R, r; t)$ is determined by solving the time-dependent Schrödinger equation:

$$i\hbar\frac{\partial}{\partial t}\Psi(r, R; t) = H(r, R)\Psi(r, R; t) \tag{2.38}$$

where $i = \sqrt{-1}$. The time-independent solution to the Schrödinger equation gives stationary states, with energy $\epsilon(R)$ associated with the electronic wavefunction $\psi_k(r, R)$ and $k$ is a quantum number associated with the eigenstates and eigenvalues.

$$H_e(r, R)\psi_k(r, R) = \epsilon(R)\psi_k(r, R) \tag{2.39}$$

The total wave function can thus be written as a product of time-dependent nuclear wave function $\chi_k(R; t)$ and stationary electronic wave function $\psi_k(r, R)$.

$$\Psi(r, R; t) = \sum_{k=0}^{\infty} \chi_k(R; t)\psi_k(r, R) \tag{2.40}$$

This expansion is exact and does not involve any approximations, which makes it too complex to solve directly. However, using the *Born − Oppenheimer approximation*, the motion of electrons and nuclei can be decoupled because of the huge mass difference

between them, and the *adiabatic approximation* which assumes that the electronic wavefunctions adapt quasi-instantaneously to the variation of the nuclear configuration. The electronic solution is obtained from the DFT (quantum mechanical solution) and nuclei being heavier are approximated using classical Newtonian mechanics. This method is termed as ab initio molecular dynamics (AIMD) since the ground-state electronic energy is computed using DFT for each nuclear configuration. Thus, one has to solve the set of Newton equations of motion with the forces derived from ab initio DFT.

$$M_I \ddot{R}_I = -\frac{\partial \phi}{\partial R_I} \tag{2.41}$$

where $M_I$ are the nuclear masses and the dots indicate the time derivative. In an AIMD trajectory, several nuclear configurations are explored and performing a self consistent calculations on each of the configurations is computationally expensive even for small system sizes.

### 2.9.1 Car-Parrinello molecular dynamics

Car-Parrinello molecular dynamics (CPMD), proposed by Roberto Car and Michele Parrinello [89], was the first method to combine molecular dynamics simulations of atomic and molecular systems with electronic structure calculations. The electronic structure problem and the dynamics of atoms are solved simultaneously by Newton's equations. This method introduces the electronic degrees of freedom as (fictitious) dynamical variables, thereby, replacing the single-particle Kohn-Sham orbitals with fictitious time-dependent classical fields. Therefore, an explicit electronic minimization at each timestep is not required after an initial electronic minimization is performed. The fictitious dynamics of electrons keeps them on the electronic ground state corresponding to each new ionic positions traversed along the dynamics, giving accurate ionic forces. This fictitious dynamics is used to keep the electrons close to the ground state, preventing the computationally expensive self-iterative minimization at each time-step.

### 2.9.2 Born-Oppenheimer molecular dynamics

The Born-Oppenheimer molecular dynamics (BOMD) method is based on the self-consistent field (SCF) methods, based on the Born-Oppenheimer approximation [90]. The nuclear and electronic degrees of freedom are well separated and the forces acting on atoms are calculated at the self-consistent ground state. In BOMD, a full SCF calculation of the wavefunction is therefore conducted at each timestep. The forces acting on each atom are calculated at every timestep, $t$, based on the wavefunction and ionic positions. The geometry at the next timestep, $t + \Delta t$ is determined using Newton's equation of motion, using the Velocity Verlet algorithm. The electron wavefunction is minimised via matrix diagonalization at each step of the trajectory. This procedure requires more computation time than the Car-Parrinello scheme.

In the present thesis, I used CP2K package [91], which is an open source electronic structure and molecular dynamics package to perform AIMD simulation on mixed-cation mixed-anion perovskite $(FAPbI_3)_{0.875}(MAPbBr_3)_{0.125}$ (Chapter 4). For all first-principles DFT simulations, I used Vienna ab initio simulation package (VASP) [92, 93], to calculate the structural and electronic properties of Co-substituted $BiFeO_3$ (Chapter 3) and structural and lattice dynamics in molecular perovskites (Chapter 5).

# Chapter 3

# Electric polarisation effects in inorganic perovskites

## 3.1 Introduction

In this chapter, I focus on inorganic ferroelectric perovskites. Here, I present a detailed analysis on electronic, ferroelectric and thermodynamic properties of pure and Co-substituted $BiFeO_3$, using DFT. At the end of the chapter, there is a short section focusing on relaxor ferroelectric, PMN-PT. Our results on Co-substituted $BiFeO_3$ were written in the form of an article and submitted to *Advanced Theory and Simulations*. Our results on relaxor ferroelectric, PMN-PT were published in an article in *Physical Review Materials*.

Multiferroic materials, which simultaneously exhibit two or more ferroic properties (ferromagnetism or anti-ferromagnetism, ferroelectricity, and ferroelasticity), are promising for a range of functional applications [94]. Bismuth ferrite ($BiFeO_3$) is among the few attractive multiferroic materials with both ferroelectric and (anti)ferromagnetic behaviour at room temperature. It has a high ferroelectric-to-paraelectric transition point (Curie temperature $T_C$ = 1103 K) and an antiferromagnetic-to-paramagnetic transition

point also well above ambient temperature (Néel temperature $T_N$ =643 K) [34]. The crystal structure (Figure 3.1) of $BiFeO_3$ at ambient conditions is rhombohedral (space group R3c), with lattice parameter $a = 5.64$ Å and rhombohedral angle $\alpha = 59.4°$ [88, 95, 96]. The off-centre displacements of the Fe and O atoms with respect to the Bi sub-lattice result in a large spontaneous polarisation along the pseudo-cubic [111] direction, primarily due to Bi translation along this direction [30, 97]. The structure is also piezoelectric at all temperatures below $T_C$ [19]. Its magnetic structure below $T_N$ is, in a first approximation, G-type antiferromagnetic, which means that each $Fe^{3+}$ spin is surrounded by antiparallel spins on nearest-neighbour Fe sites, leading to zero net moment. But there is actually a weak net magnetic moment per unit cell, which results from spin canting due to the symmetry breaking induced by the ferroelectric polarisation [98]. These properties make $BiFeO_3$ a promising room-temperature single-phase multiferroic material, with potential applications in data storage, spin valves, spintronics and sensors [34].

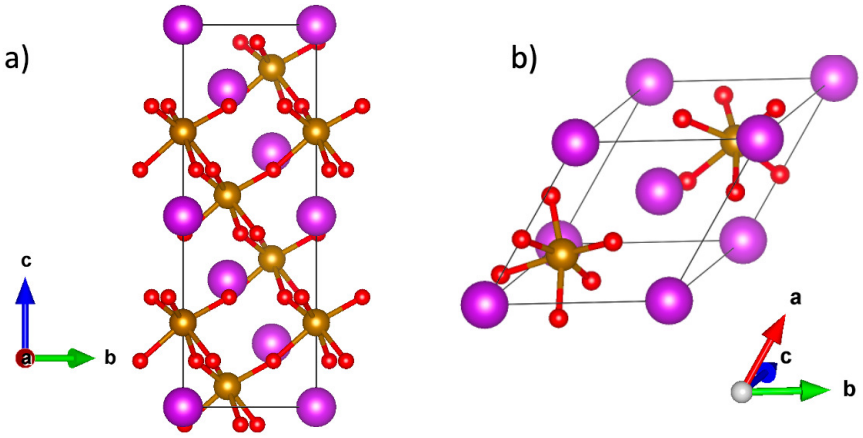


Figure 3.1: Crystal structure of $BiFeO_3$ in a) hexagonal representation, and b) rhombohedral representation (primitive cell). Colour scheme: Bi atoms are purple, Fe atoms are brown and O atoms are red.

Recently, there has also been increasing interest in using $BiFeO_3$ for photovoltaic [99–104] and photocatalytic [105–115] applications. This attention is motivated by the ferroelectric character of this oxide, because its internal electric field can be exploited to aid the separation of oppositely charged photogenerated carriers and/or to engineer the band alignment. Furthermore, $BiFeO_3$ has a relatively narrow band gap (most commonly

reported values for thin films range between 2.6 and 2.8 eV [116]), compared to most other ferroelectric oxides, which makes it especially attractive for optical applications. Since this band gap is still somewhat too wide for optimal visible light absorption, there have been efforts to use chemical substitutions to make it narrower, while retaining or improving the ferroelectric properties of the oxide. Peng *et al.* [117] showed that Co/Fe substitution led to narrower band gaps (*e.g.* from 2.66 eV in pure $BiFeO_3$ to 2.53 eV in $BiCo_{0.1}Fe_{0.9}O_3$). Recent experimental work by Machado *et al.* [102, 103] has shown that, in addition to decreasing the band gap, Co/Fe substitutions can increase the spontaneous polarisation of $BiFeO_3$, which is a bonus for photovoltaic and photocatalytic applications.

We are particularly interested in the applications of $BiFeO_3$ and $BiCo_xFe_{1-x}O_3$ in photocatalysis. Despite having an adequate band gap, pure $BiFeO_3$ does not seem to have the right band alignment and therefore is inactive as a single-semiconductor photocatalyst for the full water splitting reaction [114], but it can still be used for water photo-oxidation biased by sacrificial agents (which are then reduced instead of the protons) [118]. $BiFeO_3$ also shows promising behaviour when used as part of heterojunctions for water splitting photocatalysis. For example, $CdS/BiFeO_3$ heterojunctions forming a Z-scheme have been found to be active as particulate photocatalysts for water splitting without using any sacrificial agents [114]. Khoomortezaei *et al.* have demonstrated that photoanodes made of $WO_3/BiVO_4/BiFeO_3$ [111] or $WO_3/BiFeO_3$ [113] heterojunctions are efficient in photoelectrochemical water splitting. $BiFeO_3$ can also be useful as photocatalyst (or part of them) for other reactions, such as the degradation of organic pollutants (see Ref. [108] for a review). For example, studies involving both pure [106] and doped [112] $BiFeO_3$, as well as $BiFeO_3$–containing heterojunctions (*e.g.* with $C_3N_4$ [109]) have shown that $BiFeO_3$ is an active photocatalyst for degrading rhodamine B, an organic dye that is widely used as a colorant in the textile industry, and can be toxic to humans and animals if not removed from wastewaters. Mushtaq *et al.* have shown that the photocatalytic activity of $BiFeO_3$ in the degradation of rhodamine B can be enhanced under mechanical vibrations

thanks to piezo-photocatalytic effects [110]. In these applications, the ferroelectric character of $BiFeO_3$ is beneficial to the photocatalytic process by aiding the separation of photogenerated carriers. Recent work by Huang *et al.* [115] has shown that the effect can be enhanced by electrically poling (via the application of an external electric field) the $BiFeO_3$ nanoparticles to align the ferroelectric domains, which accelerated the photocatalytic process by a factor of two compared with unpoled $BiFeO_3$. There is also evidence that the orientation of the ferroelectric polarisation can be used to engineer photocatalytic response [107, 119]. The interplay between ferroelectric and photocatalytic properties in this material clearly deserves further research attention at the theoretical level to improve our fundamental understanding of these phenomena, which will help rationalising the design of better $BiFeO_3-$based photocatalysts.

In this chapter, we investigate the incorporation of cobalt in $BiFeO_3$, as a route to engineer its band gap, band alignment, and ferroelectric polarisation. We discuss the thermodynamic aspects of the Co/Fe substitutions, in particular the stability of the solid solution with respect to phase separation. We examine the impact of cobalt substitution on the magnitude of the $BiFeO_3$ spontaneous polarisation, which can improve charge separation and can potentially be used to engineer the band alignment for photocatalysis. We calculate the depolarisation field in a $BiFeO_3$ thin film with surface parallel to the polarisation direction, and discuss the interplay between polarisation and band alignment. In the light of our simulation results, we also discuss conflicting experimental results in the literature about the band gap, band alignment, and polarisation of these materials.

## 3.2 Methodology

The calculations are based on the density functional theory (DFT) as implemented in the Vienna ab initio simulation package (VASP) [92, 93]. For relaxations, substitution thermodynamics, and for the electronic structure calculations, we used a screened hybrid functional, based on the functional by Heyd, Scuseria and Ernzerhof (HSE06) [73] which

admixes the exact non-local exchange from the Hartree-Fock theory, screened at long-range with a screening parameter 0.2 $Å^{-1}$, into the local Perdew-Burke-Ernzerhof functional [70] of the generalized gradient approximation (GGA). In our case, 20% Hartree-Fock exchange (instead of the 25% proposed in the original HSE06 functional) was chosen, following Shimada *et al.* [95], who showed that these settings led to good agreement with experiment in terms of both structural parameters and band gap. In what follows we refer to the screened hybrid functional used here simply as HSE. For the calculation of Born effective charges and polarisations, which is computationally demanding, we used the less expensive GGA+U approach, where Hubbard effective parameters ($U_{\text{eff}}$) of 4 eV and 3.3 eV are applied to the 3d orbitals of Fe and Co, respectively; these values were originally fitted to reproduce the oxidation energies of the corresponding binary transition metal oxides [120], and are found to transfer well to describe the properties of more complex oxides of these metallic elements (*e.g.* Ref. [121, 122]).

The projector augmented wave (PAW) method [78, 79] was used in all calculations to describe the interactions between the valence electrons and frozen cores, by explicitly treating 15 valence electrons for Bi, 8 for Fe, 9 for Co, and 6 for oxygen (these are the VASP-recommended PAW pseudopotentials). We used an energy cutoff of 520 eV to truncate the plane wave expansion of the Kohn-Sham wavefunctions, which is 30% above the default cutoff for the employed PAW potentials, to minimise Pulay errors. Brillouin zone (BZ) integrations were performed by sampling the reciprocal space using a Γ-centred mesh of $4 \times 4 \times 4$ k-points with reference to the rhombohedral unit cell, and commensurate grids for supercells. The only exception were the structural relaxations, using the HSE functional, of the different Co-substitution configurations in the $2 \times 2 \times 2$ supercell, which were performed using Γ-only calculations as they are computationally expensive to perform on a k-mesh. In all cases, the cell parameters were allowed to relax, and the ions were moved towards equilibrium until the Hellmann-Feynman forces were less than 0.01 eV/Å.

The DFT calculations were all spin-polarised, and the G-type antiferromagnetic ordering was assumed, as well as collinear spin arrangements, *i.e.* the small effect of spin canting in $BiFeO_3$ was ignored. Both Fe(III) and Co(III) cations were initialised in high-spin (HS) configurations, which the calculations conserved after convergence. Iron in $BiFeO_3$ is well known to be in HS Fe(III) configuration, unless high pressures are applied, in which case a transition to low-spin (LS) takes place [34,123]. The spin state of Co (III) (a $d^6$ cation) in $BiCo_xFe_{1-x}O_3$ is more disputed in the literature. In the pure-Co end-member, $BiCoO_3$, Co(III) is in HS state at ambient pressure and low temperatures [124]. But Ray *et al.* concluded, from magnetisation measurements, that dilute Co in $BiFeO_3$ at low temperature (below 150 K) and low external magnetic field, was LS [125]. On the other hand, from a combination of magnetic measurements and DFT calculations, Fan *et al.* concluded that at ambient temperature the LS state of Co(III) in this system is unfavoured, and their GGA+U calculations indicated that HS Co(III) was more stable than LS Co(III) in $BiFeO_3$ [126]. Our own test calculations using the HSE functional in the supercell with one Co substitution showed that HS Co(III) is more stable than LS Co(III) in $BiFeO_3$, by $\sim$0.2 eV. Therefore, we have used HS Co(III) in all our calculations.

The symmetrically distinct Co substitution configurations were found using the SOD (Site Occupancy Disorder) program [127,128]. Two configurations are considered equivalent if they are related by a symmetry operator, and the group of symmetry operators of the supercell consists of the original symmetries of the unit cell and their combinations with supercell translations. The DFT energies of the symmetrically independent configurations were used to fit an effective Hamiltonian, to then perform Monte Carlo simulations in a large ($10 \times 10 \times 10$) supercell with the same composition, $BiCo_{0.125}Fe_{0.875}O_3$, using the GULP code [129, 130]. At each step of Monte Carlo simulation, a configuration is created by randomly swapping a pair of atoms, which corresponds to an energy difference $\Delta E$. The new configuration is accepted, following the Metropolis algorithm [131], with probability $p = \min(1, \exp(-\Delta E/k_{\mathrm{B}}T))$, where $k_{\mathrm{B}}$ is Boltzmann's constant and $T$ is the temperature. Forty million steps were used to achieve equilibrium, and the simulations

were performed at $T$ =500 K, 1000 K and 2000 K.

For the alignment of the band edges of $BiFeO_3$ with respect to vacuum, we built periodic slab models with different terminations, separated by a vacuum gap of 15 Å in the periodic supercell. We use the Macrodensity code [132] for calculating the planar averages of the electrostatic potential in planes parallel to the slab surface, to determine the potential difference between the bulk (average in the middle of the slab) and the vacuum level (in the middle of the vacuum gap). For the alignment of the band edges of $BiCo_{0.06}Fe_{0.94}O_3$ we did not create slabs with Co/Fe substitutions, but simply aligned the core levels of bulk Fe atoms far from Co substitutions.

## 3.3 Results and discussion

### 3.3.1 Structural and electronic properties

Calculated structural and electronic parameters of pure $BiFeO_3$ are shown in Table 3.1 in comparison to experimental values. As noted before in Ref. [95], the screened hybrid functional HSE leads to good agreement with experiment in terms of both crystal structure and band gaps. The GGA+U predictions are also reasonable, albeit with a band gap below the most accepted experimental range of 2.6-2.8 eV measured at ambient conditions [116]. Our HSE band gap is slightly above that range. However, it should be noted that there is still a lot of uncertainty about the band gap of $BiFeO_3$, with values as low as ∼2 eV or as high as ∼3 eV reported in the experimental literature for this compound, depending on synthesis conditions, resulting morphology or particle size, and measurement method [116,133]. Smaller nanoparticles tend to have narrower band gaps [134]. The band gap of $BiFeO_3$ also decreases substantially with temperature, *e.g.* from about 2.5 eV at ambient temperature to about 1.5 eV at 550°C in Ref. [135]. The value of 2.9 eV obtained here for bulk $BiFeO_3$ from HSE calculations seems therefore to be a more reasonable zero-Kelvin prediction than the GGA+U value of 2.3 eV.

The band structure (Figure 3.2a) and density of states (DOS) (Figure 3.2b) show

that the contribution of O 2p orbitals dominate the valence band (VB) edge and the contribution of Fe 3d orbitals dominate the conduction band (CB) edge. The bottom of the CB is located at the Z point of the Brillouin zone. The VB has two maxima at roughly the same energy, one between Γ and F, and the other at the Z point (the difference between the two is less than 10 meV). Both spin channels exhibit the same total density of states due to the antiferromagnetic arrangements of the magnetic moments (Fe 3d contributions with opposite spins at the same energy level come from different atoms). There is a large exchange splitting of ∼9 eV between the occupied and empty 3d orbitals of a given Fe atom, therefore the occupied Fe 3d orbitals are not shown in the DOS plot (Figure 3.2b, c).

Table 3.1: Calculated lattice parameters, a and $\alpha$, and band gap $E_g$ for $BiFeO_3$ (R3c phase). Experimental values (obtained at ambient temperature) for the cell parameters [96] and for the band gap [116] are listed for comparison.

| Parameter | Expt. | GGA+U | HSE06 |
|---|---|---|---|
| $a$/Å | 5.64 | 5.69 | 5.68 |
| $\alpha$/deg | 59.42 | 59.0 | 58.8 |
| $E_g$/eV | 2.6-2.8 | 2.3 | 2.9 |

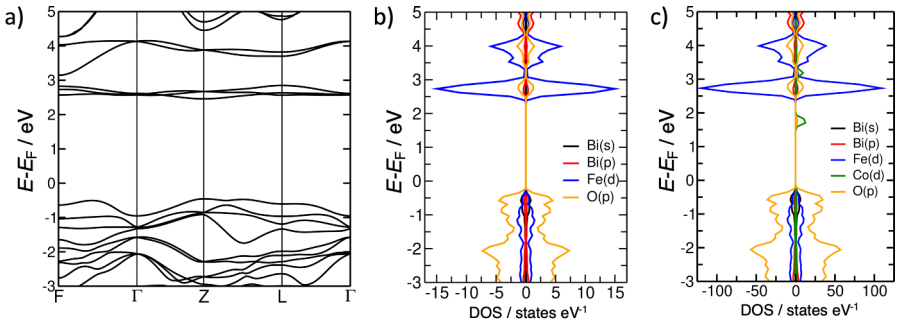


Figure 3.2: a) Band structure and b) projected density of states of pure $BiFeO_3$; and c) projected density of states of $BiCo_{0.06}Fe_{0.94}O_3$.

We then considered the substitution of one or two Fe atoms in the $2 \times 2 \times 2$ supercell by Co, in such a way that the stoichiometry of the solid solution is $BiCo_{0.062}Fe_{0.938}O_3$ or $BiCo_{0.125}Fe_{0.785}O_3$. These compositions are within the range of stability ($0 < x < 0.2$) of the rhombohedral structure for the $BiCo_xFe_{1-x}O_3$ solid solution (upon increasing $x$, the

solid solution transitions to the tetragonal structure of pure $BiCoO_3$, via an intermediate monoclinic structure [136]). The DOS plot for $BiCo_{0.062}Fe_{0.938}O_3$ (Figure 3.2c) shows the presence of an empty impurity level of Co 3d character that reduces the band gap from 2.9 to 2.1 eV. The supercell with composition $BiCo_{0.125}Fe_{0.875}O_3$ (two Co substitutions in the supercell) has only five symmetry inequivalent configurations. The DOS plots for those configurations (Figure 3.3) are very similar to the DOS plots for lower Co concentration, but with larger peaks in the Co 3d gap state, whose energy position do not change appreciably with the relative position of the Co atoms in the structure.

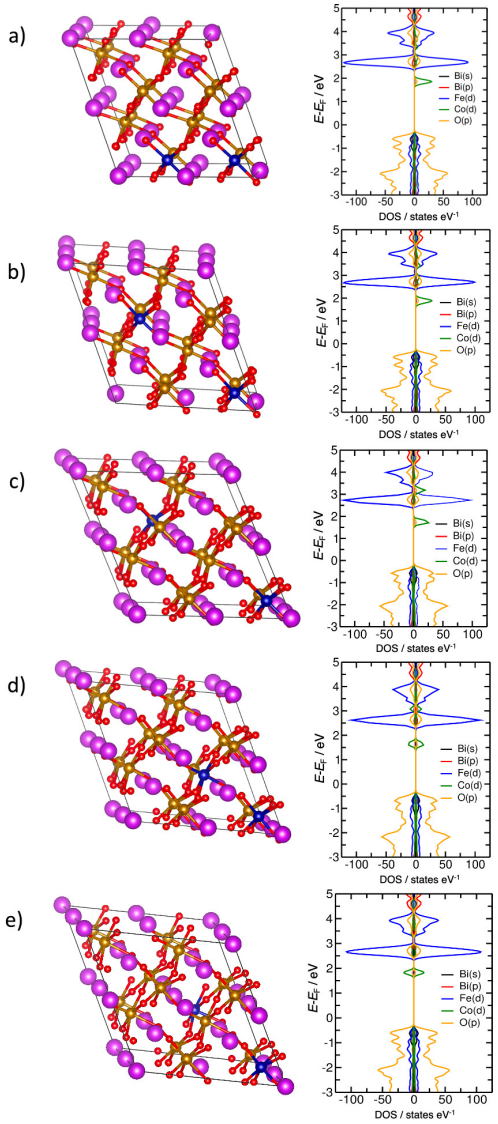


Figure 3.3: Co positions and projected density of states for the five symmetrically distinct configurations of $BiCo_{0.06}Fe_{0.94}O_3$ studied in this chapter. Colour scheme: Bi = purple, Fe = brown, Co = blue, O = red.

In these calculations, the magnetic moments of the Co ions were given the same orientation of the magnetic moments of the Fe ions they replace, thus keeping the G-type antiferromagnetic pattern; this accounts for the different relative orientations of the Co magnetic moments over the configurations (*i.e.* they are parallel in the configurations shown in Figure 3.3a, 3.3b, 3.3c, but antiparallel in 3.3d and 3.3e). In the next section we use the relative energies of these configurations to create a model to investigate the equilibrium distribution of Co substitutions.

### 3.3.2 Thermodynamics of cation distribution

For the thermodynamic analysis of the Co distribution, the DFT total energies of the five distinct configurations of double substitutions were mapped into an Ising-like Hamiltonian:

$$E = E_0 + \sum_{\langle i,j \rangle} J_{ij} S_i S_j \tag{3.1}$$

where the "spin" variable $S_i$=1 if site $i$ is occupied by Co, and $S_i = 0$ if it is occupied by Fe, and the $J_{ij}$ values characterise the strength of Co-Co interactions. Note that the spin variables and the Hamiltonian itself are unrelated to the magnetism of the system but simply describe the interactions between Co impurities. Four $J$ constants, corresponding to four different Co-Co distances, plus the $E_0$ values, are then obtained from the five DFT energies, by solving the system of five linear equations with five variables.

The interaction parameters $J$ as a function of Co-Co distance ($d$) are shown in Figure 3.4a. Clearly, the interaction between impurities is more attractive when the distance between them is shorter. To study the effect of these interactions on the equilibrium cation distribution at specific temperatures, we performed Monte Carlo simulations in a larger $(10 \times 10 \times 10)$ supercell with the same composition, $BiCo_{0.125}Fe_{0.875}O_3$. At $T = 500$ K, Co impurities aggregate as one pure-Co spherical cluster per simulation cell (Figure 3.4b). The formation of such small separate Co clusters is, of course, an artifact from the simulation cell size; using a larger simulation cell would lead to larger and more separated

Co clusters. The result from the Monte Carlo simulation simply indicates that there is a thermodynamic preference for Co aggregation, which would lead to complete phase separation at that temperature. Our simulations at $T$ = 1000 K and 2000 K still led to Co impurity aggregation. Only at unrealistically high temperatures does the equilibrium cation distribution becomes more homogeneous.

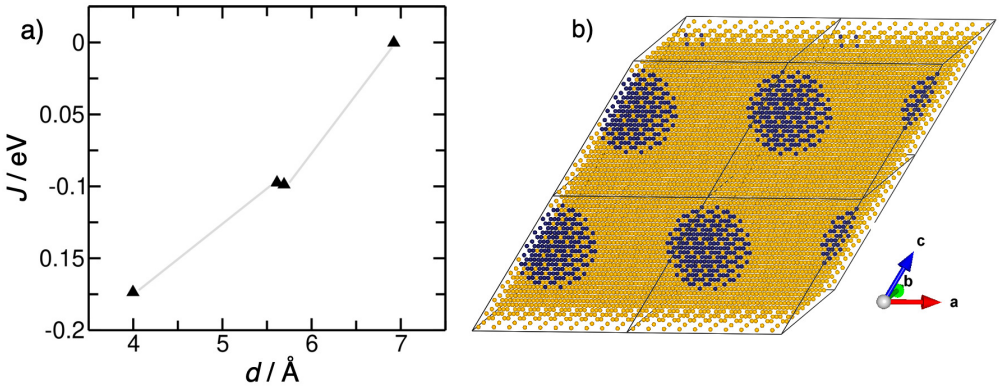


Figure 3.4: a) Interaction parameter ($J$) as a function of Co-Co distance ($d$) for 12.5% Co concentration. The grey line is a guide to the eye. b) Equilibrated distribution of impurities after Monte Carlo simulations at $T$ =500 K. Only Co atoms (in blue) and Fe atoms (in brown) are shown.

While these simulations show that there is a strong thermodynamic drive towards phase separation, they implicitly force the $BiCoO_3$ clusters to remain in the rhombohedral structure of $BiFeO_3$. In reality, it would be thermodynamically favourable for $BiCoO_3$ to separate forming its preferred crystal structure, which is tetragonal [136]. To quantify the thermodynamic stability of the $BiCo_xFe_{1-x}O_3$ solid solution against phase separation to rhombohedral $BiFeO_3$ and tetragonal $BiCoO_3$ phases, we have calculated the enthalpy of mixing per formula unit of $BiFe_{1-x}Co_xO_3$ with respect to the pure compounds using the equation:

$$\Delta H_{\text{mix}} = E[\text{BiFe}_{1-x}\text{Co}_x\text{O}_3] - (1-x)E[\text{BiFeO}_3] - xE[\text{BiCoO}_3], \tag{3.2}$$

where the $E$ values are the DFT energies per formula unit for the corresponding compositions, at their ground-state structures. For $x = 0.0625$, we obtain $\Delta H_{\text{mix}} = 0.027$ eV per

formula unit. As is common in the description of very dilute solid solutions (*e.g.* [137,138]), we can write that for small values of $x$:

$$\Delta H_{\text{mix}} = Wx \tag{3.3}$$

where $W = 0.43$ eV is the solution energy. From this value we can estimate the thermodynamic solubility limit $x_s$ of Co in $BiFeO_3$, as the minimum of the free energy of mixing (including $\Delta H_{\text{mix}}(x)$ and the configurational entropy contribution) at a given temperature, which is:

$$x_s \approx e^{-\frac{W}{k_B T}} \tag{3.4}$$

For example, at $T = 600$ K, $x_s = 0.00026 = 260$ ppm. Therefore, Co substitution in $BiFeO_3$ can be expected to be thermodynamically stable against phase separation only at trace amounts.

However, even when phase separation is thermodynamically preferred, homogeneous solid solutions can still exist, protected by the very slow kinetics of cation diffusion. Cation exchange barriers are well known to be very high, typically ∼2 eV or above for ionic solid solutions. For example, values of 193 kJ/mol, 200 kJ/mol, and 230 kJ/mol have been estimated from experimental measurements of cation exchange kinetics in $(Fe_{0.5}Mn_{0.5})_2SiO_4$ olivines [139], $(Fe_3O_4)_x(MgAl_2O_4)_{1-x}$ magnetite-spinel solid solutions [140], and disordered $MgAl_2O_4$ spinels [141], respectively. These high activation barriers mean that cation exchange typically only starts, at any measurable rate, if samples are heated above ∼700 K, and full equilibrium (involving either ex-solution or ordering) is only reached at much higher temperatures. For Co-substituted $BiFeO_3$, we have not calculated cation exchange activation barriers (such calculations are not trivial, because the mechanism for cation exchange may involve the collective movements of many atoms and/or be mediated by vacancies or other defects), but it can be safely expected that they would be similarly high. Therefore, while there is clearly a thermodynamic driving force for ex-solution in Co-substituted $BiFeO_3$, such separation process would only be observable if samples are

treated at high temperatures. When a homogeneous solid solution is prepared it should remain stable (or more precisely, metastable) if kept at ambient or only moderately high temperatures. An example of such metastable oxide solid solution used as a functional material is $Ce_{1-x}Zr_xO_2$ [142], which is thermodynamically unstable with respect to phase separation into Ce-rich and Zr-rich oxides at most compositions, but still can be synthesised as a homogeneous solid solution that is widely used in catalysis at moderate temperatures [143, 144].

### 3.3.3 Ferroelectric properties

To study the effect of cobalt substitution on ferroelectric properties of $BiFeO_3$, we calculate the spontaneous polarisation $P$ from first principles. The Born effective charge (BEC) tensor for atom $j$, ($Z^*_{j,\alpha\beta}$) is defined as the derivative of the polarisation $P$ with respect to the atom coordinates (at zero electric field):

$$Z^*_{j,\alpha\beta} = \left.\frac{\partial P_\alpha}{\partial u_{j,\beta}}\right|_{\epsilon=0} \tag{3.5}$$

where $\alpha$ and $\beta$ are Cartesian indices, and can be obtained in VASP using density functional perturbation theory [145]. Then, to estimate spontaneous polarisation we compute the Cartesian components of the polarisation $P_\alpha$ as:

$$P_\alpha = \frac{e}{V}\sum_{j\beta} \bar{Z}^*_{j\alpha\beta}\Delta u_{j\beta} \tag{3.6}$$

where

$$\bar{Z}^*_{j\alpha\beta} = \int_0^1 Z^*_{j\alpha\beta}(\xi)d\xi \tag{3.7}$$

is the average of the BEC tensor over the values of the distortion parameter $\xi$ that connects the ferroelectric R3c phase ($\xi$=1) and the reference, centrosymmetric R$\bar{3}$c phase ($\xi$=0); $\Delta u_{j\beta}$ is the displacement of ion $j$ in the Cartesian direction $\beta$. These calculations are performed using the less computationally expensive GGA+U theory and not HSE which

is computationally too demanding to calculate BEC at each distortion parameter. The polarisation calculated at different distortion points is shown in Figure 3.5.

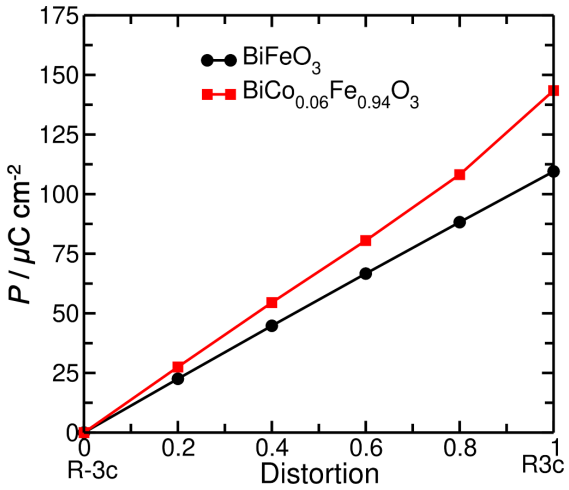


Figure 3.5: Change in polarisation [111] component along a path from the centrosymmetric R$\bar{3}$c structure to polar R3c phase for $BiFeO_3$ and $BiCo_{0.06}Fe_{0.94}O_3$.

For pure $BiFeO_3$, we obtained 109 $\mu C/cm^2$, and it increases to 143 $\mu C/cm^2$ for $BiCo_{0.06}Fe_{0.94}O_3$ (there is only one Co atom per supercell at this composition, and there is only one symmetrically distinct Fe site, so the result does not depend on the substitution site). Let us first discuss the value for the pure compound. It is well known that experimental measurements of polarisation in this material have led to a very wide spread of results (*e.g.* Table I in Ref. [97] lists experimental values from different sources ranging from 2.2 to 158 $\mu C/cm^2$). There are several causes for this spread of polarisation values measured in experiment. Polarisation measurements are often affected by leakage current problems, which might account for some of the very small values reported for $BiFeO_3$. Poor sample quality, or the presence of structural modifications, can also affect the result. Furthermore, the spread of polarization values may also be related to the multi-valued nature of that property, which is well explained by the modern theory of polarisation [86]: polarisation in solids is in fact a "lattice" of values, rather than a single vector. Very different values can then be obtained if the ferroelectric switching behaviour in samples is substantially different. In Ref. [97] it was concluded that the most "natural" value of the polarisation of pure $BiFeO_3$ along the <111> direction should be 90-100 $\mu C/cm^2$, which

was consistent with the most recent thin film measurements. A value of 100 $\mu$C/cm$^2$ is also quoted in the review by Catalan and Scott, as a sensible value [34]. Our theoretical result of 109 $\mu$C/cm$^2$ for pure $BiFeO_3$, is close to these best estimations.

To compare the predicted effect of Co substitution on the $BiFeO_3$ polarisation, we turn to the experimental results presented by Machado *et al.* in Ref. [103]. In that work, pure $BiFeO_3$ was measured to have a polarisation of only 26.1 $\mu$C/cm$^2$, which is low compared to currently accepted values. Therefore, we cannot directly compare our calculated absolute values with their experiments. However, the qualitative effect of Co substitution can be compared: they observed an increase in the polarisation to 60 $\mu$C/cm$^2$ for $Co_{0.1}Bi_{0.9}FeO_3$, in comparison with the pure compound. In our calculations, the behaviour is the same: the incorporation of Co to $BiFeO_3$ significantly enhances its ferroelectric polarisation. The greater BEC of Co compared to Fe (Table 3.2) is consistent with the enhanced polarisation in the substituted system. Interestingly, in Ref. [102], a GGA+U calculation with a higher value of the Hubbard parameter for Co 3d orbitals, $U_{eff} = 6$ eV, compared to the value used in this work, $U_{eff} = 3.3$ eV, did not lead to much difference in polarisation between pure and Co-substituted $BiFeO_3$. We have not been able to reproduce their results exactly (there are other differences in methodology), but we do observe a much smaller enhancement (∼50% of ours) of the polarisation upon Co substitution when using their $U_{eff}$ value. The effect of $U_{eff}$ and other calculation settings on the estimated polarisation deserve further study.

Table 3.2: Born Effective Charges (BECs) (average of diagonal elements for each atom), and polarisation $P$, for $BiFeO_3$ and $BiCo_{0.06}Fe_{0.94}O_3$ in R3c phase.

| | BEC/$e$ | | | | $P/\mu$Ccm$^{-2}$ |
|---|---|---|---|---|---|
| | Bi | Fe | Co | O | |
| $BiFeO_3$ | 4.64 | 3.97 | | -2.87 | 109 |
| $BiCo_{0.06}Fe_{0.94}O_3$ | 4.97 | 4.02 | 5.24 | -2.91 | 143 |

### 3.3.4 Band alignment and applications in photocatalysis

To explore the activity of these compounds in photocatalytic applications, it is important to estimate the positions of the VB maximum and the CB minimum on an absolute scale, for example, relative to the vacuum level. This is necessary to obtain the relative energies of these band edges with respect to half-reaction potentials for the redox reactions of interest, *e.g.* water splitting. However, energy levels obtained from the bulk calculation are given relative to the average electron potential in the solid. To align the electronic structure with reference to the vacuum level, we determine the potential difference $\Delta V$ between the vacuum potential and the pseudo-bulk average using an auxiliary slab calculation. In the first instance, to ignore the effect of ferroelectric polarisation, we have used a symmetric and stoichiometric slab terminated by the non-polar (110) surface, for which the vacuum level is the same at both sides of the slab (Figure 3.6).

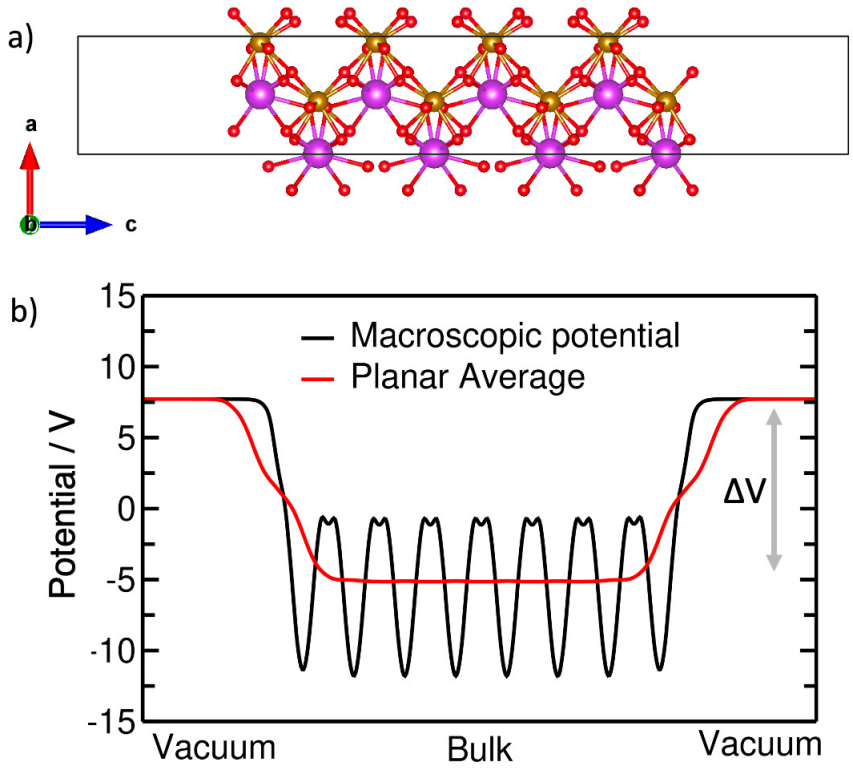


Figure 3.6: (a) $BiFeO_3$ slab along with (110) surface termination and (b) planar average electrostatic potential for that slab.

The calculated positions of the band edges of $BiFeO_3$ and $BiCo_{0.06}Fe_{0.94}O_3$ with respect

to vacuum potential are shown in Figure 3.7. We can compare these with the half-reaction potentials for water splitting, corresponding to the hydrogen evolution reaction (HER) and the oxygen evolution reaction (OER):

$$\begin{aligned} \mathrm{H_2O} &\longleftrightarrow 2\mathrm{H^+_{(aq)}} + \frac{1}{2}\mathrm{O_{2(g)}} + 2\mathrm{e^-} \quad \text{(OER)} \\ 2\mathrm{H^+_{(aq)}} + 2\mathrm{e^-} &\longleftrightarrow \mathrm{H_{2(g)}} \quad \text{(HER)} \end{aligned} \tag{3.8}$$

and other water splitting reactions involving generation of $\dot{\mathrm{O}}\mathrm{H}$ radicals:

$$\begin{aligned} 2\mathrm{H_2O} &\longleftrightarrow 2\mathrm{H^+} + 2\dot{\mathrm{O}}\mathrm{H} + 2\mathrm{e^-} \\ \mathrm{O_2} + 2\mathrm{e^-} + 2\mathrm{H^+} &\longleftrightarrow 2\dot{\mathrm{O}}\mathrm{H} \end{aligned} \tag{3.9}$$

In the vacuum scale and at pH = 0, the HER level is located at -4.44 eV, and the OER level is located at -5.67 eV. At temperature $T$ and pH>0, these energy levels are shifted up by $k_\mathrm{B}T \times \mathrm{pH} \times \ln 10$. For pH = 7 and room temperature, the HER level is then located at $-4.03$ eV and OER level is located at $-5.25$ eV, respectively. For a water splitting photocatalyst made of a single semiconductor, the positions of the CB minimum and the VB maximum should straddle those half-reaction potentials. The band edges of $\mathrm{BiFeO_3}$ and $\mathrm{BiCo_{0.06}Fe_{0.94}O_3}$ and the water redox potentials are shown in Figure 3.7. The calculated band edges are not well aligned with the half-reaction potentials for water splitting, because the CB edges are too negative with respect to the HER level, suggesting that these materials are not suitable as single-semiconductor photocatalysts for the full water splitting reaction.

When comparing our band alignment with experiment, we must recall that to build band alignment diagrams, experimentalists measure or estimate at least two out of four properties: the ionization potential (IP), the electron affinity (EA), the band gap ($E_\mathrm{g}$) and/or the electronegativity (here $\chi = \frac{\mathrm{IP+EA}}{2}$). The relation between these quantities and

the band edges $E_{\mathrm{CB}}$ and $E_{\mathrm{VB}}$ is given by the equations:

$$E_{\mathrm{CB}} = -\mathrm{EA} = -\chi + \frac{1}{2}E_{\mathrm{g}} \tag{3.10}$$

$$E_{\mathrm{VB}} = -\mathrm{IP} = -\chi - \frac{1}{2}E_{\mathrm{g}} \tag{3.11}$$

Usually, the optical band gap is measured, and one of the other three properties is also obtained, to complete the band diagram. Given that there are wide differences in measured band gaps, and that there are various ways to measure or estimate the other properties, strong discrepancies in the band alignments reported for $BiFeO_3$ in the experimental literature are not surprising. For example, Ji *et al.* [107] calculated the IP of $BiFeO_3$ from the ultraviolet photoelectron spectrum (by subtracting the width of the spectrum from the exciting photon energy). Combined with a band gap of 2.74 eV, that measurement led to a CB edge at −3.56 eV and a VB edge at −6.30 eV in the vacuum scale, which *do* straddle the water splitting redox potentials. A similar band alignment for $BiFeO_3$ band edges with vacuum had been proposed before by Wu and Wang [146]. These authors measured an optical band gap of 2.73 eV, and estimated the EA at 3.33 eV following Clark and Robertson [147], who had given that value from a simple comparison with $SrBi_2Ta_2O_9$. That leads to a CB edge at −3.33 eV and a VB edge at −6.06 eV in the vacuum scale, also straddling the water splitting redox potentials. However, the EA of $BiFeO_3$ seems to be significantly underestimated in those studies. A more direct measurement was made by Moniz *et al.* [118] using electrical impedance spectroscopy and a Mott-Schottky plot [148], from where an EA of 4.62 eV was obtained. A CB edge at −4.62 eV in the vacuum scale means that the band edges of $BiFeO_3$ *do not* straddle the water splitting redox potentials, the CB edge being too negative. This result also agrees with the simpler estimation of band positions made by Li *et al.* [105], using the electronegativity $\chi$ of the oxide calculated as the geometric mean of the electronegativities of the constituent atoms, and a measured band gap of 2.19 eV, from where they arrive at an EA of 4.94 eV. The same method has been applied by other authors, using slightly different

band gaps [106,114]. Kolivand and Sharifnia [114] confirmed the value determined by this method (EA = 4.84 eV) with their own Mott-Schottky plot analysis. Interestingly, if we use our HSE band gap, the average electronegativity method leads to almost the same band positions that we obtain from the DFT calculation in the auxiliary slab.

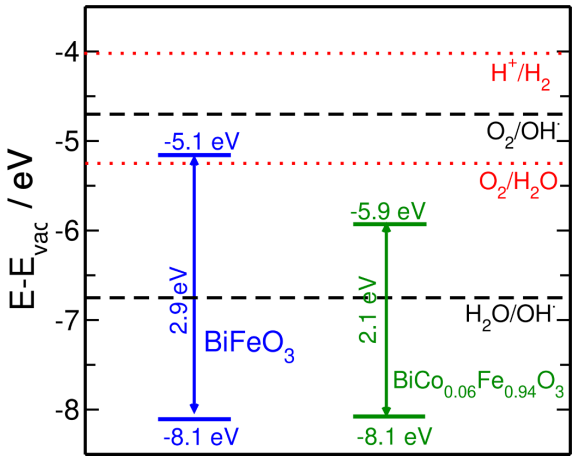


Figure 3.7: CB and VB edges calculated with the HSE functional for $BiFeO_3$ and $BiCo_{0.06}Fe_{0.94}O_3$. The half-reaction potentials for water splitting are represented by dotted red lines, and those for the generation of ȮH radicals are represented by dashed black lines.

Table 3.3 summarises EA estimations from the literature in comparison with our theoretical results. Our results support the higher EA estimations in the literature from Mott-Schottky measurements (albeit with a small overestimation). Thus our findings confirm the conclusion that unmodified $BiFeO_3$ cannot be used as a single-semiconductor photocatalyst for water splitting, because the EA is too high (the CB is too negative) to drive the hydrogen evolution half-reaction. Cobalt substitution does not help on this issue, because the low-lying empty Co 3d levels increase the EA and lower the CB further, as seen in figure 3.7. However, $BiFeO_3$ can also be used for water splitting in heterojunctions with other semiconductors like CdS, as demonstrated by Kolivand and Sharifnia [114]. They showed that pure $BiFeO_3$ was not photocatalytically active for the full water splitting reaction, which is also consistent with our theoretical band alignment. When $BiFeO_3$ is in a heterojunction with CdS, which has a lower EA (they estimate ∼4 eV), a direct Z-scheme [149] band alignment forms, which allows unassisted water splitting without using

any sacrificial agents. For such heterojunctions, Co substitution in $BiFeO_3$ might be advantageous, because the band gap narrowing with respect to the pure compound would allow more efficient visible light absorption at the $BiFeO_3$ end of the heterojunction, while the more negative CB would reduce the losses associated to the interfacial electron-hole recombination.

Table 3.3: Estimations of the electron affinity (EA) of $BiFeO_3$ reported in the literature, in comparison with the values obtained in this work. In some of the original papers, values are reported with respect to the normal hydrogen electrode (NHE), and have been converted here to the vacuum scale for easy comparison.

| Source | EA (eV) | Method |
|---|---|---|
| Clark & Robertson (2007) [147]<br>Wu & Wang (2010) [146] | 3.33 | Comparison with $SrBi_2Ta_2O_9$ |
| Li *et al.* (2009) [105] | 4.94 | Band gap measured and electronegativity estimated from elements |
| Ji *et al.* (2013) [107] | 3.56 | Band gap measured and ionization potential from ultraviolet photoelectron spectrum |
| He *et al.* (2013) [106] | 5.01 | Band gap measured and electronegativity estimated from elements |
| Moniz *et al.* (2014) [118] | 4.62 | Electrical impedance spectroscopy and Mott-Schottky plot |
| Kolivand & Sharifnia (2020) [114] | 4.84 | Band gap measured and electronegativity estimated from elements; Mott-Schottky plot |
| This work | 5.13 | DFT calculations in bulk and auxiliary slab |

Without help from a heterojunction, $BiFeO_3$ and $BiFe_{1-x}Co_xO_3$ could also be used as photocatalysts for other reactions. For example, the production of hydroxyl radicals from water for oxidation of organic pollutants might be a more suitable reaction [150]. These $\dot{O}H$ radicals can be useful for the degradation of effluents from textile and pharmaceutical industries. The relevant redox pairs and the energy levels of the half reactions are also shown in figure 3.7. Our calculated band edges for $BiFeO_3$ do not quite straddle the half-reaction potentials, but because our EA value is likely to be a bit overestimated (as shown by the comparison with a range of experiments), the position of the band edges should be about right for this reaction.

Finally, we discuss the effect of the ferroelectric polarisation on the band alignment, in a very simplified picture. The above band alignment calculation, based on a symmetric

non-polar slab along the [110] direction, ignores any interplay between the band alignment and ferroelectric polarisation effects. We therefore construct another slab, now along the polarisation ([111]) direction. The surface termination of the slab is such that the only dipolar moment comes from the ferroelectric distortion: the slab with equivalent surface termination for the centrosymmetric phase (R-3c) is non-polar (Figure 3.8a). In the slab for the ferroelectric R3c phase (Figure 3.8b), the macroscopic average potential exhibits a gradient $\mathrm{d}V/\mathrm{d}z = 0.064$ V/Å, which represents the depolarisation field that arises to compensate for the surface dipole. Such depolarisation field creates a drive to separate photogenerated charge carriers. Furthermore, it leads to a shift in the band positions in an isolated thin film, which is proportional to the magnitude of the field and to the thickness of the film.

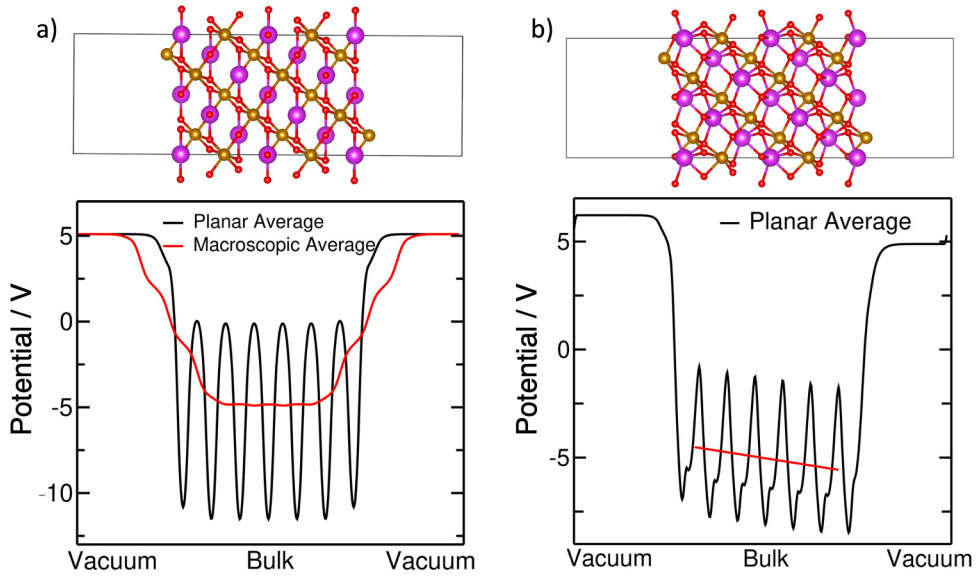


Figure 3.8: $BiFeO_3$ slabs with (111) surface terminations and the planar average electrostatic potential for (a) centrosymmetric (R-3c) phase and (b) polar (R3c) phase.

Given the calculated field intensity of ∼64 mV/Å, a film that is, for example, ∼2 nm thick in the polarisation direction would exhibit a band shift of ∼1.3 eV between its two surfaces. Such shift is more that the misalignment of the CB of $BiFeO_3$ for the HER. In the Co-substituted film, where the polarisation is stronger, the depolarisation field intensity will also be higher, and this effect will be even stronger. In practice, such a film may attract free carriers from the surroundings that would partially or totally compensate

the electric field or surface reconstructions may happen. The present model constitutes an initial approximation to the theoretical modelling of what is undoubtedly a very complex phenomenon.

## 3.4 Polarisation calculations on a relaxor ferroelectric: PMN-PT

I present here another application of the same type of polarisation calculations described earlier in this chapter. The theoretical work presented below was performed to support an experimental study by Dr Gareth Nisbet (Diamond Light Source) [151]. Because our contribution in this case does not represent a full theoretical study, I have added this work as a final section of this chapter, rather than devoting a full thesis chapter to it.

Relaxor ferroelectrics such as $Pb(Mg_{1/3}Nb_{2/3}O_3)$-$x$$PbTiO_3$ (PMN-PT) exhibits a giant piezoelectric (electromechanical) response near the morphotropic phase boundary and thus has been extensively studied due to their use in capacitors and piezoelectric devices [35, 36]. Unlike normal ferroelectrics, which exhibit a very sharp ferroelectric-to-paraelectric phase transition and no frequency dependence for their dielectric response, relaxor ferroelectrics exbihit a diffused phase transition, the ferroelectric-to-paraelectric phase transition proceeds gradually rather than sharply, and frequency dependence of the dielectric constant (*i.e.* dielectric relaxation).

$Pb(Mg_{1/3}Nb_{2/3}O_3)$-$x$$PbTiO_3$ is a solid solution of relaxor $Pb(Mg_{1/3}Nb_{2/3}O_3)$ (PMN) and ferroelectric $PbTiO_3$ (PT). The phase diagram of the solid solution is shown in Figure 3.9. PMN-PT exists in rhombohedral phase at low temperatures up to some PT content. At higher PT concentrations, it undergoes a morphotropic phase transition and becomes tetragonal. A giant piezoelectric response is observed near this transition. The system becomes cubic for all PT concentrations at high temperatures (Figure 3.9).

In the present chapter, the experiments performed by Dr Gareth Nisbet (at Diamond Light Source, Didcot) show a tetragonal to monoclinic phase accompanied by a giant

piezoelectric response. Here, I use density functional theory calculations to relate experimental results to possible microscopic mechanisms to explain the phase transitions involved.

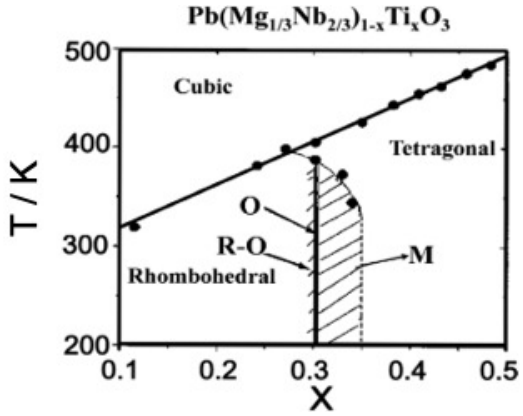


Figure 3.9: Phase diagram of $Pb(Mg_{1/3}Nb_{2/3}O_3)$-$x PbTiO_3$ solid solution system. Reproduced with permission from Ref. [152]. R, O and M refer to rhombohedral, orthorhombic and monoclinic phase, respectively.

We used DFT as implemented in the VASP package [92, 93], to create a preliminary model for the phase transitions observed. We built structural models that match the observed tetragonal and monoclinic phases, albeit with composition $Pb_8Nb_4Mg_2Ti_2O_{24}$, which corresponds to eight $Pb(Nb_{2/3}Mg_{1/3})_{1-x}Ti_xO_3$ formula units, with $x = 0.25$. This is close, but not exactly identical, to the experimental composition, and it has the advantage of allowing the representation of the cation distribution with integer occupancies in a computationally affordable supercell size, as proposed by Tan *et al.* [153]. The exchange-correlation energy of electrons is treated within the generalized gradient approximation (GGA) with the functional by Perdew, Burke and Ernzerhof (PBE) [70]. The projector augmented wave (PAW) method [78,79] was used to describe the interactions between the valence electrons and the frozen cores. We used an energy cutoff of 520 eV to truncate the planewave expansion of the Kohn-Sham wavefunctions. Brillouin zone (BZ) integrations were performed by sampling the reciprocal space using a Γ-centred mesh of 4×4×4 k-points.

We construct models that match the observed tetragonal and monoclinic phases. Using the ISODISTORT package [154] we identify a continuous displacive transition connecting

the monoclinic and tetragonal phases. The tetragonal phase is an average of two monoclinic phases where the distorted angle flips from $\alpha > 90°$ to $\alpha < 90°$ via the tetragonal structure, the energy of the system as a function of this flipping motion is plotted in Figure 3.10(a). The distortion parameter $\eta$ is an interpolation parameter between the two monoclinic structures ($\eta = \pm 1$) and the tetragonal structure ($\eta = 0$). In the absence of an external field the monoclinic phase is ~25 meV/atom more stable than the tetragonal phase. However, factors such as domain wall energies (pinning) can serve to hold the metastable phase in place.

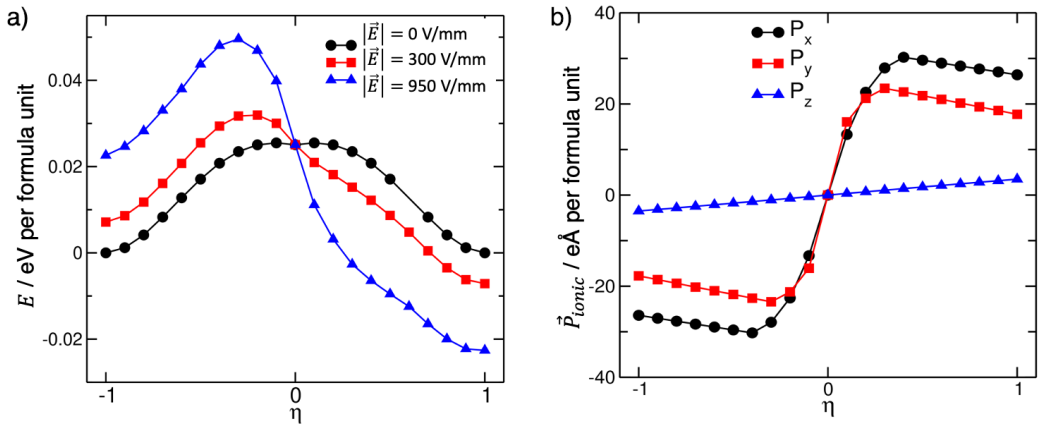


Figure 3.10: (a) Total energy as a function of distortion parameter at different electric field intensities (all energies are given relative to the energy of the monoclinic phase in the absence of field); (b) ionic contribution to total polarisation (relative to the polarisation in the tetragonal phase) as a function of distortion parameter.

When the system is poled by an external electric field, the symmetry between the energies of the monoclinic phases is broken and one phase becomes favoured over the other. We estimate the relative polarization of the phases using calculations based on the modern theory of polarization [86]. The total polarisation for a given crystal system can be calculated as a sum of ionic and electronic contributions. The ionic contribution is obtained by summing the product of the position of each ion in the unit cell (with a given choice of basis vectors) with the nominal charge of the ionic core. The electronic contribution to the polarization is calculated as a Berry phase of the Bloch wavefunctions using the method first developed by King-Smith and Vanderbilt [155]. The dominant contribution to the spontaneous polarization is from the ions; the electronic contribution is

found to be negligible. The polarisation vector of the system as a function of the distortion parameter is plotted in Figure 3.10(b). By adding the dot product of the polarisation vector and the experimentally applied electric field ($E_{\text{dipole}} = -\vec{P}.\vec{E}$) to the ground state DFT energy, we can calculate the total energy of the polarised systems in the presence of the external field. One of the monoclinic phases now becomes significantly more favourable compared to the tetragonal phase ($> 70$ meV/atom). When this change in energy is large enough to overcome the effect of domain wall pinning, then the system would at this point transform from tetragonal to monoclinic phase, with the concomitant large volume changes. The new monoclinic phase gradually switches to the same orientation as the persistent monoclinic phase and the system cannot be reverted to the energetically less stable monoclinic + tetragonal mixture of the original system.

The calculations show that (i) the two phases are relatively close in energy and thus coexistence of both phases (particularly when considering possible domain wall pinning) is thermodynamically reasonable; (ii) there is a continuous displacive path between the phases and no bond breaking is required for the transition; (iii) an external electric field in the right direction will stabilise one of the monoclinic distortions significantly over the other and over the tetragonal phase. While the composition of the model system differs from the experimental setup (due to restrictions in size of simulation), the general trends observed and proposed mechanism should not be affected significantly by changing composition.

## 3.5 Conclusions

I have discussed here the response of the multiferroic material $BiFeO_3$ to Co substitution in Fe positions, considering electronic, magnetic and thermodynamic aspects. Co/Fe substitutions is an interesting strategy to modify the functional behaviour of $BiFeO_3$. The band gap of the system is significantly reduced, from 2.9 eV to around 2.1 eV, as a result of Co substitution, and there is a simultaneous enhancing of the spontaneous polarisation.

This large enhancement of ferroelectricity in this system would further promote effective carrier separation in applications such as photovoltaics or photocatalysis. Our Monte Carlo simulations show that $Co^{3+}$ ions would tend to aggregate at the concentrations studied here if an equilibrium distribution can be reached, although this phase separation is likely to be kinetically limited by cation diffusion barriers at most temperatures of interest for applications. Our calculations confirm that a high electron affinity of $BiFeO_3$ that makes the conduction band too negative in comparison with the level for the hydrogen evolution reaction. Therefore, unmodified $BiFeO_3$ cannot photocatalyse the full water splitting reaction. However, direct Z-schemes with semiconductors with lower electron affinity could be used for this reaction, and we argue that Co/Fe substitutions would improve the performance of $BiFeO_3$ in such composite photocatalyst. We demonstrate how large electric fields form in these materials, associated with the ferroelectric distortion, and how these fields can affect the electronic level positions. $BiCo_xFe_{1-x}O_3$ solid solutions deserve further theoretical and experimental investigation in terms of its photocatalytic applications.

# Chapter 4

# Mixed-cation mixed-anion perovskite $(FAPbI_3)_{0.875}(MAPbBr_3)_{0.125}$: an ab initio molecular dynamics study

## 4.1 Introduction

Hybrid organic-inorganic perovskite (HOIP) solar cells have attracted great attention due to their extraordinary optoelectronic properties such as large absorption coefficient, high electron-hole diffusion length, and high charge-carrier mobility. $CH_3NH_3PbI_3$ were the first perovskites to be used as a light absorber with a photo-conversion efficiency of 15% by 2013 [156]. In this material, the A, B, and X sites of the perovskite structure $ABX_3$ are occupied by the ions $MA^+$, $Pb^{2+}$, and $I^-$, respectively. Other members of the HOIP family are obtained when replacing iodide by other halides, replacing lead by another group IV cation, or replacing $MA^+$ by another organic cation or caesium. The full family includes random alloys of the pure compounds. However, $MAPbI_3$ is barely stable against decomposition into lead iodide and methylamine iodide, causing fast device degradation. There have been significant achievements in the stability by means of interface engineering, [157–159] and by alloying the cations and halides [46]. In the

so-called mixed-cation HOIP, the perovskite A-site is randomly occupied by a combination of different cations, *e.g.*, $MA^+$, $HC(NH_2)^+$ (formamidinium, $FA^+$) or the inorganic cation $Cs^+$. These mixed compounds show remarkable improvement in their stability and are related with the evolution of record PCE [158]. Some of the recent perovskite solar cell (PSC) record efficiencies have been obtained using light absorber perovskites with composition $(FAPbI_3)_{1-x}(MAPbBr_3)_x$, with $x \sim 0.15$ [160, 161] or with $MAPbBr_3$ as a trace [162]. This composition was introduced by Jeon *et al.*, [163] showing that incorporation of $MAPbBr_3$ into $FAPbI_3$ stabilises the perovskite phase of $FAPbI_3$ and improves the PCE, particularly for composition $(FAPbI_3)_{0.85}(MAPbBr_3)_{0.15}$. The understanding of this material, and eventually the PSC development, will benefit from atomic scale simulations of the bulk materials and the interfaces. The first obstacle is the lack of models for the randomly mixed compounds. Models of several binary alloys, with either a cation or lead substituted, have been published recently [164, 165]. In fact, some recent experimental studies of mixed-cation mixed-halide perovskites have been complemented with simulations with one element substituted [166]. In this chapter, I study an atomic scale model of the mixed-cation mixed-halide $(FAPbI_3)_{1-x}(MAPbBr_3)_x$. The mixing ratio $x = 0.125$ is considered for the model, which is computationally convenient and close to the composition used in optimised PSC. The model is based on pseudo-random substitutions of FA and I in $FAPbI_3$, by MA and Br, respectively. I then study the structural and vibrational properties by means of AIMD. The alloy properties are compared with those of the pure compounds $FAPbI_3$ and $MAPbBr_3$. The results presented in this chapter were published in an article in the *Journal of Materials Chemistry A* [167]. The article contains more results than those presented here, because it was a collaborative work with Dr Eduardo Menendez-Proupin's research group in Chile, I have only presented here the results to which I contributed directly.

## 4.2 Computational details

AIMD calculations were performed to investigate the structural, dynamical, and electronic properties of $(FAPbI_3)_{0.875}(MAPbBr_3)_{0.125}$, $FAPbI_3$ and $MAPbBr_3$ using the CP2K package [91]. The simulations were conducted under NVT conditions at temperature $T = 350$ K. The ionic forces were calculated using first-principles DFT. The hybrid Gaussian and plane wave method (GPW), as implemented in the QUICKSTEP module of the CP2K package, [168] has been used. The forces for the molecular dynamics were calculated using the PBE functional [70] with the Grimme correction scheme DFT-D3 [84] to account for the dispersion interactions. The Kohn–Sham orbitals of valence electrons are expanded in a Gaussian basis set (DZVP-MOLOPT for Pb, I, Br, C, N, H) [169]. The effect of core electrons was included by means of dual-space GTH pseudopotentials [170–172]. The functional minimisations were performed using the orbital transformation method [173, 174]. The timestep was set to 1 fs. A Nosé–Hoover chain thermostat of length 3 was used, with a time constant of 10 fs during the initial 2000 steps, and 100 fs for the rest of equilibration and sampling stages. During the initial 2000 steps, each atom had one individual thermostat applied to; this is called a massive thermostat and facilitates a fast thermalisation of systems with too different atomic masses, such as H and Pb. The simulations were extended up to 28, 26, and 23 ps for $FAPbI_3$, $MAPbBr_3$, and $(FAPbI_3)_{0.875}(MAPbBr_3)_{0.125}$, respectively. These systems were considered equilibrated (*i.e.* the average energy over 4 ps was constant within 0.01 eV) after the initial 8, 6, and 5 ps, respectively, while sampling took place for the subsequent time ranges. The full set of atomic coordinates along the MD simulations are available in a public repository [175].

## 4.3 Results and discussion

### 4.3.1 Model generation

Using the structure from ref. [164] for $FAPbI_3$, the 384−atom tetragonal supercell was transformed into a 768−atom $4 \times 4 \times 4$ cubic supercell by means of the lattice transformation $\vec{A}' = \vec{A} + \vec{B}$, $\vec{B}' = \vec{B} - \vec{A}$, where $\vec{A}$, $\vec{B}$ ($\vec{A}'$, $\vec{B}'$) are the initial (final) supercell lattice vectors. The conventional cubic lattice parameter was set at the experimental value $a = 6.3620$ Å [176]. For $MAPbBr_3$, I started from the structure of ref. [177] with lattice parameter $a = 5.9328$ Å. For the 768-atom supercell, the vector lengths are $A' = B' = 4a$. The initial orientation of the MA cations was taken from the $MAPbI_3$ polymorphic model of ref. [178].

The solid solution $(FAPbI_3)_{0.875}(MAPbBr_3)_{0.125}$ was modelled by means of a special quasi-random structure (SQS) [179] which was generated as follows. First, the set of all symmetrically different configurations within a $2 \times 2 \times 2$ perovskite supercell with composition $FA_7MAPb_8Br_3I_{21}$, was obtained using the site occupation disorder method (SOD) [127]. For this purpose, cubic crystal symmetry (space group 221) of the parent lattice was assumed, considering FA and MA as point atoms. For each of the 62 inequivalent configurations, the number of Br atoms (out of eight halides) in the first coordination sphere around MA, is 0, 1, 2 or 3. Eight of these $2 \times 2 \times 2$ supercells were then combined to form a $4 \times 4 \times 4$ supercell configuration that satisfies two conditions: (i) The halide–halide pair correlation function (the average of the products of $S_i$ and $S_j$, where $S_i = 1$ or $-1$, depending on the cation occupying the site) is as close as possible to the expected one for the random distribution, *i.e.* $\langle S_i S_j \rangle = (2x-1)^2 = 0.5625$ [179], considering the fraction of halide sites occupied by Br, $x = 3/24$. For the best SQS configuration, the obtained pair correlation functions are 0.5625, 0.5070, and 0.3958 for the first, second and third coordination spheres, respectively. (ii) The distribution of MA−Br pairs is as close as possible to the binomial distribution expected for the random solution. The probability of finding $n$ Br ions as nearest neighbours to the MA (out of $N = 12$ halides)

is $P(n) = C(N, n)x^n(1-x)^{N-n}$. These numbers must be approximated to fractions $m/8$, as we combine eight $2 \times 2 \times 2$ supercells to form the $4 \times 4 \times 4$ supercell. This condition translates in the requirement of including two $2 \times 2 \times 2$ configurations with $n = 0$, three with $n = 1$, two with $n = 2$, and one with $n = 3$, in the composition of the $4 \times 4 \times 4$ supercell, as shown in Table 4.1. The supercell generated in this way is shown in Figure 4.1a.

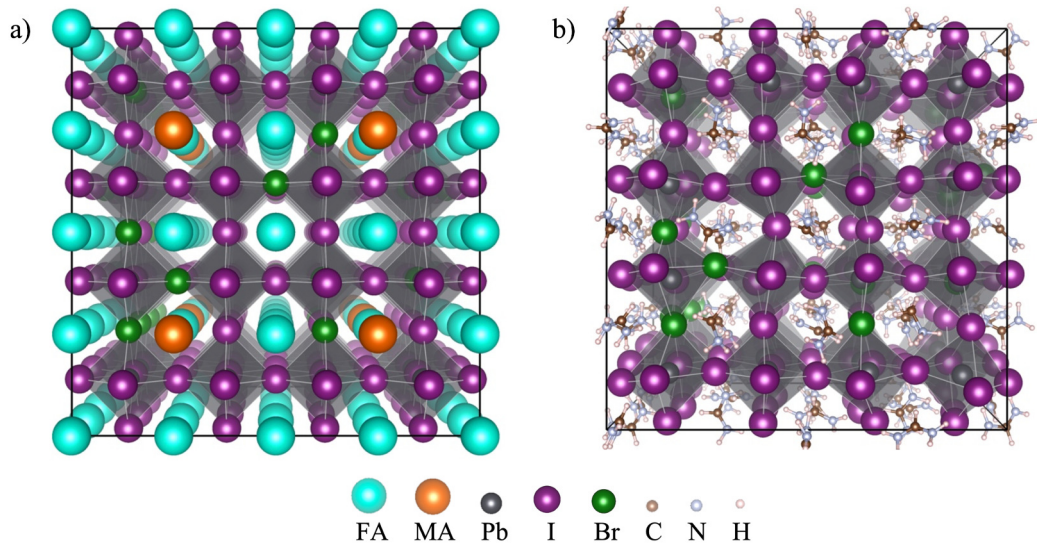


Figure 4.1: Model supercell of $(FAPbI_3)_{0.875}(MAPbBr_3)_{0.125}$ with MA and FA cations represented as point pseudo-atoms, and Br and I anions distributed following the quasi-ransom approach described in the text (all atoms at cubic perovskite symmetric positions). (b) Snapshot of MD simulation at 350 K, with explicit atoms of MA and FA.

Finally, the point-like MA and FA cations were replaced in the obtained $4 \times 4 \times 4$ supercell by the full molecular cations, giving them random initial orientation, and the structure was then thermalised by MD. Figure 4.1b shows the full structure, drawn with the same perspective as Figure 4.1a. The supercell size was set as A = $4a$, with $a$ = 6.3115 Å, that results from linear interpolation of the experimental densities of the end compounds $FAPbI_3$ and $MAPbBr_3$. A theoretical (equilibrium) lattice parameter could have been determined, but this would have needed expensive variable cell MD. Instead, some degree of validation was pursued by means of static variable cell optimisation, enforcing the cubic shape of the supercell, and taking the initial atom coordinates from a random configuration of the MD. With this procedure, the optimised lattice parameter was found

as 6.3125 Å, which is very close to the interpolated value used in the subsequent MD simulations with the NVT ensemble. Applying the same procedure to the end compounds, values 6.37253 Å, and 5.9312 Å, were obtained for $FAPbI_3$ and $MAPbBr_3$, respectively, which are also close to the experimental values mentioned above, used in our subsequent simulations.

Table 4.1: Probability of finding $n$ Br ions as nearest neighbours to the MA (out of $N = 12$ halides in the first coordination sphere around MA). The ideal probability, as given by the binomial distribution $P(n) = C(N, n)x^n(1-x)^{N-n}$, corresponds to random occupation. The model probabilities are limited to fractions of 8, as the $2 \times 2 \times 2$ supercell contains 8 MA cations.

| $n$ | Ideal $P(n)$ | Model P($n$) |
|---|---|---|
| 0 | 0.201 | $2/8 = 0.250$ |
| 1 | 0.345 | $3/8 = 0.375$ |
| 2 | 0.271 | $2/8 = 0.250$ |
| 3 | 0.129 | $1/8 = 0.125$ |
| 4 | 0.042 | 0 |
| 5 | 0.009 | 0 |
| 6 | 0.002 | 0 |
| 7 | 0.0002 | 0 |
| 8 | 0.0001 | 0 |
| 9 | 0.0 | 0 |
| 10 | 0.0 | 0 |
| 11 | 0.0 | 0 |
| 12 | 0.0 | 0 |

### 4.3.2 Structural analysis

I now discuss the structural information derived from the MD simulations. The descriptors of the local structure include pair distribution function, angle distribution functions, and cation orientation, with special attention given to variation induced by the cation and halide substitutions. Figure 4.2 shows the partial pair distribution functions (PDFs) for the solid solution and the end members. The partial pair distribution functions [180] are defined as

$$g_{ij}(r) = \frac{V}{N_i N_j} \sum_{k}^{N_i} \sum_{l}^{N_j} \langle \delta(r - r_{kl}) \rangle \tag{4.1}$$

where $N_i$ and $N_j$ are the number of atoms of the species $i$ and $j$ per volume $V$, containing $N$ atoms of all species. The brakets $\langle ... \rangle$ indicate the statistical average over the MD configurations. The total PDF is given as:

$$g(r) = \sum_{i,j} c_i c_j g_{ij}(r) \tag{4.2}$$

where the species fractional concentrations are $c_i = N_i/N$.

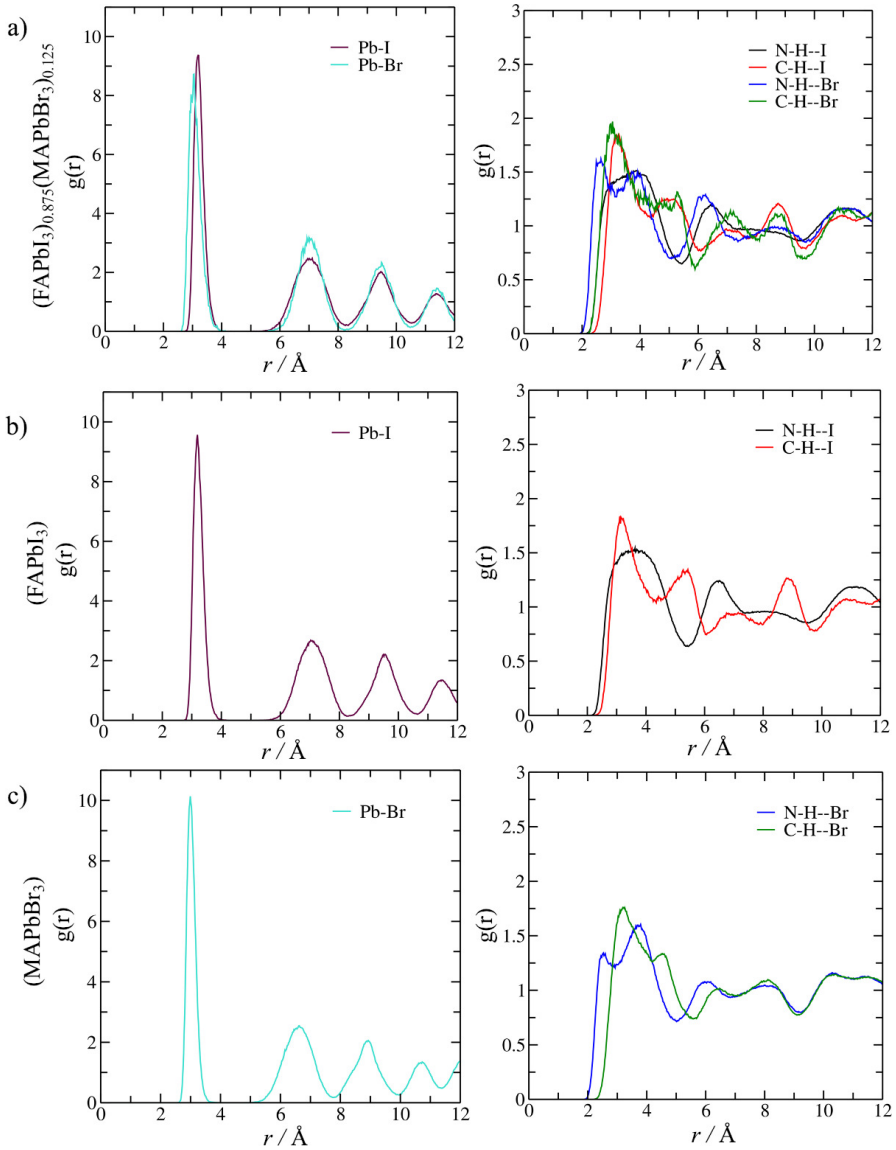


Figure 4.2: Partial pair distribution functions for species Pb-I and Pb-Br (left panel) and H-halide (right panel), differentiating the cases where H is bound to N or C for a) $(FAPbI_3)_{0.875}(MAPbBr_3)_{0.125}$, b) $FAPbI_3$ and c) $MAPbBr_3$

All the simulation supercells considered in this chapter contain 64 A sites (occupied by MA or FA), 64 B sites (occupied by Pb), and 192 X sites (occupied by I or Br). In the simulation cell of $(FAPbI_3)_{0.875}(MAPbBr_3)_{0.125}$ there are 24 Br anions and 8 MA cations. As seen in Figure 4.2a, the Pb-Br PDF at the range of the first coordination shell in the solid solution has the maximum at a similar distance (3.06 Å bond length) to the corresponding in $MAPbBr_3$ (3.01 Å, Figure 4.2c), whereas the Pb-I bond length is the same (3.20 Å) in $FAPbI_3$ and in the solid solution. The shorter Pb-Br bond distance compared with Pb-I bond length implies that Pb-Br-Pb trios are compressed, and the Br moves less freely in the solid solution than in pure $MAPbBr_3$. Figure 4.3 supports this conclusion, showing that the Pb-Br-Pb angles are closer to 180° in the mixture than in pure $MAPbBr_3$, while the Pb-I-Pb angles in the mixture tend to be lower than in $FAPbI_3$.

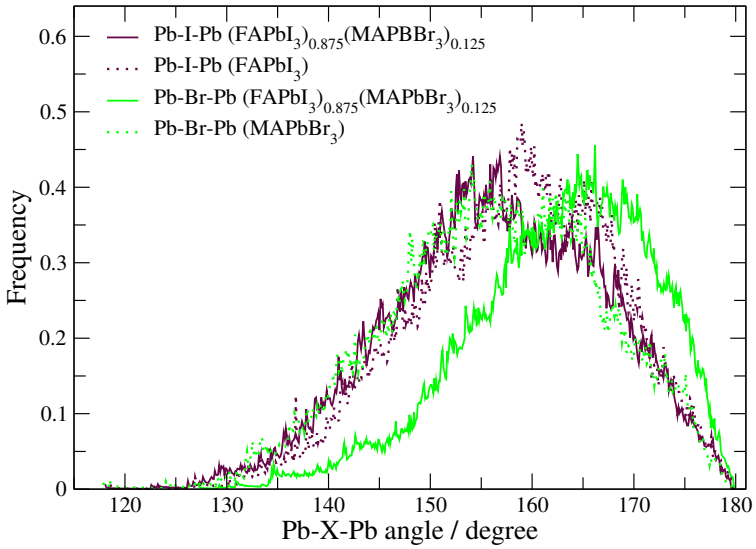


Figure 4.3: Distribution of Pb-X-Pb (X= Br, I) angles in the three compounds. Solid lines correspond to $(FAPbI_3)_{0.875}(MAPbBr_3)_{0.125}$, while dashed lines correspond to $FAPbI_3$ and $MAPbBr_3$.

The heterogeneous distribution of the Pb-X-Pb angles of the solid solution must generate deformations in halogen cages that surround the organic cations, together with disparate Pb-Br and Pb-I bond lengths within each octahedra. Since the generated SQS supercell has a relatively homogeneous distribution of Br atoms, it is expected that these deformations should be present throughout the solid solution. These deformations are expected to disturb in some way the dynamics of the rotations of the organic cations in

the mixture, because the well-known coupling between rotations and the vibrations of the inorganic framework. Also, the rotation of organic cations is guided by their hydrogen bonds interactions with their environment.

In Figure 4.2, the X−H (X = Br, I) PDF marks the difference between the H bonded to N or C. First, there is the double peak structure of the Br−H(N) PDF (Br with the H of the $NH_3$ group in MA) in pure $MAPbBr_3$. The maximum at 2.53 Å signals hydrogen bonds, while the maximum at 3.79 Å indicate non-bonding distances. For $FAPbI_3$, the PDF of I−H(N) (with the H of $NH_2$ end groups in FA) presents a single broad peak. This difference between Br−H(N) and I−H(N) is kept in the solid solution, regardless of the cation to which the N−H species belongs to. The X−H(C) PDFs presents one single maximum at $\sim$ 3 Å. The maximum of the I−H(C) PDF occurs at the same distance in $FAPbI_3$ and the solution. In contrast, the maximum of the Br−H(C) PDF occurs at a slightly higher distance (compared with Br−H(C) PDF) in $MAPbBr_3$, but at a smaller distance in the solution. The Pb−Br PDF first peak in the solid solution is broader than in pure $MAPbBr_3$. For higher coordination shells, the Pb−X PDF attain maxima at the same distance for both X = Br, I, although there are differences in the broadening and height of the PDFs. The Pb−halide distances for the second higher coordination shells are determined by the lattice parameter. The decreased broadening of the Pb−Br PDF compared with Pb−I and with Pb−Br in $MAPbBr_3$ is difficult to interpret, but it may be related with the Pb−Br−Pb angles being closer to 180°, as shown in Figure 4.3. The molecular dynamics shows that MA makes precession and rotations around its axis, with the $NH_3$ always pointing to the central Br (for 8 ps), although at the same time the $CH_3$ group points to other Br atoms. This can be seen in the video Br-1MA.mpg, provided in the dataset [175], which shows a local environment with 3 Br close to one MA. The Br atom at the centre is surrounded by 3 FA and 1 MA. The geometrical parameters are 4.0 Å in distance cutoff, and 30° in angle cutoff. The hydrogen bonds are not permanent but form and break dynamically at this temperature. Thus, the MA cations in the solid solution have the rotation affected by two causes: the deformations of the halogen cage

that surrounds them, and the favourable hydrogen bond interactions (identified from the interatomic distance) towards the Br atoms.

### 4.3.3 Dynamic properties

The orientation dynamics of organic cations is one of the fingerprints of HOIP, modifying the dielectric response, carrier conductivity, and thermodynamic properties, among others. In MD, this information can be obtained from the vector autocorrelation function [181] defined as:

$$c(\tau) = \frac{1}{N}\sum_{n=1}^{N}\langle \hat{n}(t_n).\hat{n}(t_n+\tau)\rangle \tag{4.3}$$

where $N$ is the number of different time origins averaged, the unit vector $\hat{n} = \frac{\vec{u}}{|\vec{u}|}$, and $\vec{u}$ is the relative position vector of pairs of atoms that define molecular orientation. Figure 4.4 shows the $c(\tau)$ functions for the three characteristic vectors: (i) vector C−N in $MA^+$ parallel to molecule dipole (black arrow), (ii) vector C−H in $FA^+$ (red arrow), also parallel to molecule dipole and to the short molecule axis, and vector N−N in $FA^+$ (blue arrow), associated to the so-called tumbling motion that rotates along the long molecule axis [182].

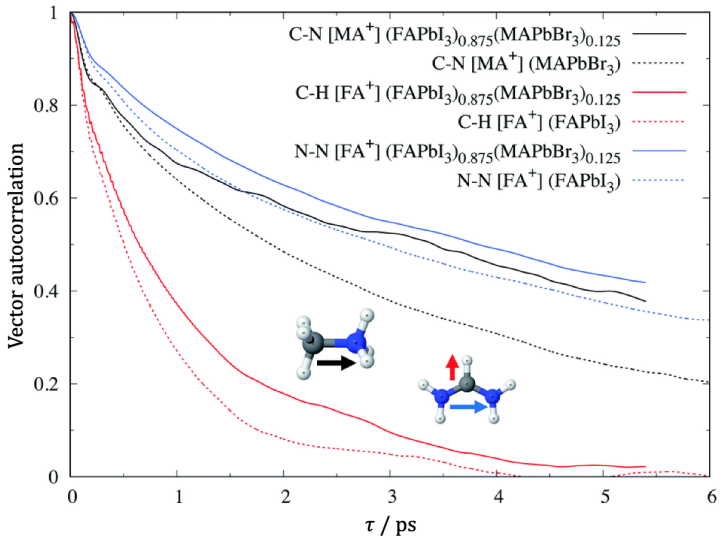


Figure 4.4: Vector autocorrelation of organic cations (rotation). The insets indicate the vectors in $MA^+$ (C–N), and $FA^+$ (C–H and N–N), using the same colours as in the corresponding curves.

In the three cases, the curves decay more slowly in the solid solution (solid lines) than in the pure compounds (dashed lines), indicating that mixing slows down the cation reorientation dynamics of both the MA and the FA cations (although the effect seems stronger for the former than for the latter). The slowing down of FA orientation dynamics after cation mixing has previously been observed in MD simulations of $FA_{0.9}Cs_{0.1}PbI_{0.3}$ in ref. [182].

### 4.3.4 Vibrational properties

Figure 4.5 shows the partial vibrational densities of states (VDOS), determined from the Fourier transform of the velocity autocorrelation function, of $(FAPbI_3)_{0.875}(MAPbI_3)_{0.125}$, $FAPbI_3$ and $MAPbI_3$. The vibrations of the inorganic backbone are in a band in the range $0-200$ cm$^{-1}$. This band also contains important contributions from FA and MA. The band in the range $500-800$ cm$^{-1}$ is due to FA vibrations only, while the band in the range $1000-1800$ cm$^{-1}$ is due to both MA and FA vibrations. The band for frequencies larger than 3000 cm$^{-1}$ is due to the stretching of C−H and N−H bonds in the organic cations [183]. As can be appreciated from Figure 4.5a and 4.5b, the VDOS and the partial VDOS of the solid solution is almost identical to the weighted sum of the DOS of the pure compounds. This observation suggests a possible method for quantification of the composition $x$ in the solution. In particular, the amount of $FA^+$ can be determined from isolated modes in range $1675-1800$ cm$^{-1}$, which are associated to the stretching of the double resonant C=N bond of $FA^+$. The out-of-plane N−H bending modes of $FA^+$, in the range $400-800$ cm$^{-1}$ could also be used. The band of stretching modes should be more effective in practice, because there are no more modes at this high frequency. $MA^+$ modes display isolated bands or peaks in the ranges $900-980$ cm$^{-1}$, 1235 cm$^{-1}$ and $1400-1500$ cm$^{-1}$. The intensity ratios of some of these bands in IR spectra may allow a quantification of the MA/FA content. On the other hand, Br content cannot be easily determined because the VDOS of Br and I overlap in the same spectral region.

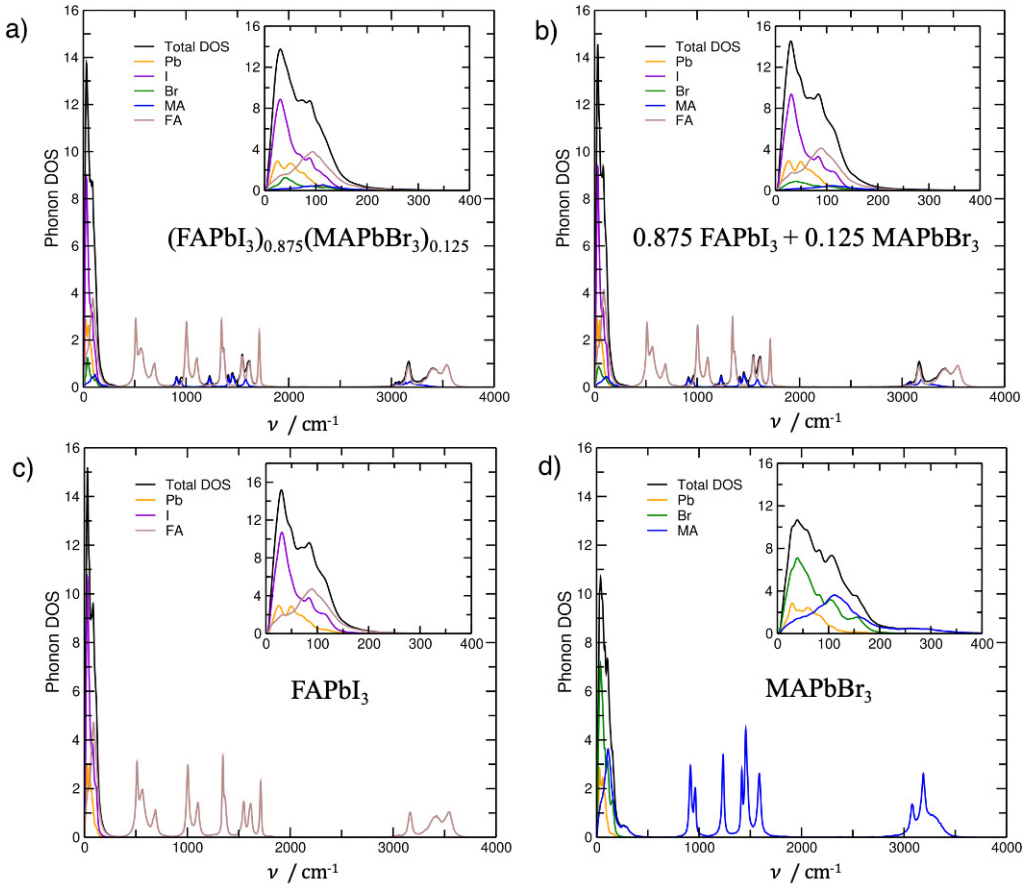


Figure 4.5: Vibrational density of states (VDOS) and contribution of each crystal site to the total VDOS for (a) the solid solution $(FAPbI_3)_{0.875}(MAPbBr_3)_{0.125}$, (b) the linear combination of 0.875 $FAPbI_3$ + 0.125 $MAPbBr_3$, (c) $FAPbI_3$, and (d) $MAPbBr_3$.

The fact that the VDOS of the solid solution is well approximated by the weighted VDOS of the compounds, suggests that the contribution of vibrations to the free energy of mixing is relatively small and can be neglected in a first approximation. This is important because it allows us to analyse the stability of the solid solution considering only energies and configurational entropic effects, as we do in the next section.

### 4.3.5 Thermodynamics of mixing

We have calculated the enthalpy of mixing per formula unit of $(FAPbI_3)_{0.875}(MAPbBr_3)_{0.125}$ with respect to the pure compounds $FAPbI_3$ and $MAPbBr_3$ using the equation:

$$\Delta H_{\text{mix}} = \frac{1}{64}\Big\{E[(\text{FAPbI}_3)_{1-x}(\text{MAPbBr}_3)_x] - (1-x)E[\text{FAPbI}_3] - xE[\text{MAPbI}_3]\Big\} \quad (4.4)$$

where the $E$ values are the average energies for the corresponding supercells from the AIMD, and $x = 0.125$ is the $MAPbBr_3$ molar fraction. We obtain $\Delta H_{\text{mix}} = 1.39$ kJmol$^{-1}$, which means that the mixing is endothermic. However, the configurational entropy

$$S_{\text{conf}} = -4k_B(x\ ln(x) + (1-x)ln(1-x)) \tag{4.5}$$

is large (12.5 Jmol$^{-1}$K$^{-1}$ for $x = 0.125$) due to the factor of 4, which appears because there are four mixed sites (1 MA/FA and 3 Br/I) per formula unit. Assuming that the enthalpy of mixing and the configurational entropy contribution are the dominant effects on the stability, the free energy of mixing is predicted to be negative ($\Delta G$ = -3.00 kJmol$^{-1}$). To assess whether the mixed perovskite can be expected to be stable with respect to phase separation into $MAPbBr_3$-rich and $FAPbI_3$-rich compounds, it is not enough to obtain the mixing free energy at the given composition (which quantifies the stability with respect to the pure phases). We also need to calculate the free energy at the whole range of compositions to assess if the given composition lies within a miscibility gap. AIMD are too computationally expensive to perform for the whole range of compositions, but we can extrapolate our one-point result using the widely used regular solid solution model, [142, 184–186] where the enthalpy of mixing is given by:

$$\Delta H_{\text{mix}} = W_0 x(1-x) \tag{4.6}$$

for which we obtain $W_0$ = 12.7 kJmol$^{-1}$. With this enthalpy parameter, the mixing free energy in the regular solution model is convex for the full range of compositions at 350 K, implying that there is no miscibility gap: with 4 mixed sites per formula unit, the enthalpy parameter $W_0$ would need to be greater than the critical value of $8k_BT$, or $\sim$25 kJmol$^{-1}$ at 350 K, for a miscibility gap to exist. The above analysis suggests that the mixed perovskite is indeed thermodynamically stable against phase separation. Although we have ignored other possible contributions to the thermodynamics of mixing (including vibrational and rotational contributions to the entropy of mixing), the low enthalpy of

mixing in the regular model, well below the critical value for miscibility gaps, suggests that our prediction is not likely to change by including such contributions. Still, this is a point that deserves further investigation. A precise evaluation of vibrational and rotational contributions to the thermodynamics of mixing from MD simulations might become more affordable soon, thanks to progress in accurate machine-learned potentials, including on-the-fly learning schemes for MD [187, 188].

The stability of this solid solution results from the simultaneous mixing in the cation and halide sites. Both substitutions impact the thermodynamic stability (free energy of mixing) through enthalpic and entropic contributions. In terms of the entropy (Equation 4.5), clearly the halide mixing has the strongest effect, because it contributes 3 mixed sites per formula unit, whereas the cation mixing only contributes 1 mixed site per formula unit. But the thermodynamic stability of mixed-cation mixed-halide perovskites is not only due to entropy effects, but also to enthalpy contributions. There are known instabilities in the mixed-halide perovskites $MAPb(I_xBr_{1-x})_3$ and $FAPb(I_xBr_{1-x})_3$, especially segregation into Br-rich and I-rich phases upon exposure to light [46]. In fact, the strategy of two-cation and three-cation mixing was devised as an alternative to improve the stability [163, 189]. Furthermore, cation substitution (*e.g.* of caesium or lighter alkaline dopants) enhances perovskite nucleation and growth, crystal quality, and suppresses ion migration. These parameters are relevant for solar cell durability, although they are not directly linked with thermodynamical stability [190].

## 4.4 Conclusions

An atomic scale model of the random solution $(FAPbI_3)_{0.875}(MAPbBr_3)_{0.125}$ has been proposed. Several computed properties have been shown to reproduce available experimental measurements, such as lattice constant, cation orientation dynamics, and thermodynamic stability. Other physical properties are reported, including distance and angle distribution functions, vibrational and dynamical properties. All these properties of the solid solution

$(FAPbI_3)_{0.875}(MAPbBr_3)_{0.125}$ are compared with those of the end compounds $MAPbBr_3$ and $FAPbI_3$. Our MD simulations of $(FAPbI_3)_{0.875}(MAPbBr_3)_{0.125}$ at 350 K, show a certain locking effect on the organic cations, leading to slower cation orientation dynamics in this solid solution compared with the pure compounds. Thermodynamic calculations suggest there is no miscibility gap for the random alloying of $MAPbBr_3$ and $FAPbI_3$. Our model is therefore useful for the detailed understanding of the physical behavior of this important material, accounting for both disorder and dynamic effects, and will allow future investigation of other bulk properties as well as of the behavior of its surfaces and interfaces.

# Chapter 5

# First-principles modelling of dicyanamide-based molecular perovskites

## 5.1 Introduction

$ABX_3$ molecular perovskites, where A and/or X are molecular moieties, have attracted increased attention in recent years. They show a 3D $[BX_3]^-$ network with the monovalent A-site cation sitting in the void of the $[BX_3]^-$ network for charge balance. The use of molecular anions at the X site increases the size of the pseudocubic $[BX_3]^-$ network, allowing molecular A-site cations with varying chemistries and sizes to be used. Molecular perovskites such as $[(NH_2)_3C]M(HCOO)_3$, $[(CH_3)_2NH_2]M(N_3)_3$, $[(C_2H_5)_3(C_7H_7)N]M(C_2N_3)_3$ and $[(Ph_3P)_2N]M[Au(CN)_2]_3$ with $M^{2+}$ typically being $Mn^{2+}$, $Co^{2+}$, $Ni^{2+}$ and $Zn^{2+}$ [191–196], can then be formed. The use of molecular A and X-site species enhances the structural and chemical diversity in these perovskites, leading to new opportunities for tuning macroscopic material properties. Examples are tilt and shift engineering to impart ferroelectric properties [197, 198], tunability of hydrogen bonding interactions [199] between the A-site cation and the 3D $[BX_3]^-$ network with ramifications on the mechanical

response [200, 201], adjustable phase transition thermodynamics [202, 203] and varying structural complexities [204] amongst others.

An important ramification of using molecular building units to form network materials is the introduction of weak chemical interactions such as dispersion interactions and hydrogen bonds. There are a number of research examples such as glass-type behaviour in $[(CH_3)_2NH_2]Zn(HCOO)_3$ [205], (defect-dependent) mechanical properties in $[(NH_2)_3C]Mn(HCOO)_3$ [206], temperature- and pressure-induced reversible ($[(CH_3)_2NH_2]M(HCOO)_3$) [207] and irreversible ($[(nPr)_4N]Cd(C_2N_3)_3$) [208] phase transitions, and more generally, structural distortions that can be activated by temperature and pressure, that all together point at relatively shallow free energy landscapes [209]. The recent discovery of irreversible phase transitions in the perovskite materials $[(NH_2)_3C]Mn(H_2POO)_3$, $[(C_5H_{10})_2N]Cd(C_2N_3)_3$ and $[(C_4H_9)_3(CH_3)N]Mn(C_2N_3)$ is in full agreement with this perspective [210–212]. For instance, crystal structure analysis for $[(NH_2)_3C]Mn(H_2POO)_3$ has shown that the different polymorphs are related to different tilt systems, *i.e.* the detailed distortion arrangement within the $[Mn(H_2POO)_3]$ network, reminiscent of conformational polymorphism as observed for molecular crystals [70, 213].

The mechanical properties of molecular perovskites have been demonstrated to be tuneable through different components of the material [214]. For instance, the larger elastic moduli and hardness of $[C(NH_2)_3]Mn(HCOO)_3$, compared to $[(CH_2)_3NH_2]Mn(HCOO)_3$, have been attributed to the larger number of hydrogen bonding interactions [215], and similar conclusion can be drawn for the elastic moduli across the A-site solid solution series $[NH_3NH_2]_{1-x}[NH_3OH]Zn(HCOO)_3$ [216]. Looking at the impact of the metal ion, a linear correlation between the elastic moduli and ligand field stabilisation energy has been observed for the series $[(CH_3)_2NH_2]M(HCOO)_3$ with $M^{2+}$ = $Mn^{2+}$, $Co^{2+}$, $Ni^{2+}$ and $Zn^{2+}$ [217]. The impact of B-site metal defects has been studied by comparing $[C(NH_2)_3]Mn(HCOO)_3$ with its defective analogue $[C(NH_2)_3]Fe_{2/3}\square_{1/3}(HCOO)_3$, ($\square$ = vacancy), which exhibits a bulk modulus that is nearly 30% lower [206]. This body of work demonstrates the potential for tailoring mechanical properties in hybrid and molecular

perovskites, depending on a clear understanding of the chemical and physical principles that affect them. More recently, molecular perovskites such as $[(C_4H_9)_4N]Mn(C_2N_3)_3$ and $[(C_4H_9)_4N]Cd(C_2N_3)_3$ have emerged as model systems in barocalorics, where their modular building principle enables to search for crystal chemistry factors that determine a materials' performance in solid-state cooling [203, 204]. A relation between the compressibility and the barocaloric performance has recently been implied [218], an intuitive link when considering the barocaloric coefficient $dT_C/dp$ as a proxy. A softer material is expected to exhibit a larger barocaloric coefficient, an important guideline to manipulate the barocaloric performance in the future. Therefore, the identification of crystal chemistry principles that determine a molecular perovskite's mechanical response, *i.e.* its structural response to pressure such as compressibility or similarly the bulk modulus, is an important step forward in the search for intuitive material design guidelines.

This chapter focuses on the molecular perovskite series $[(nPr)_3(CH_3)N]M(C_2N_3)_3$ with M = Mn, Co, Ni, nPr = n−propyl and $C_2N_3^-$ = dicyanamide anion (figure 5.1a and 5.1b), which exhibits an irreversible perovskite-to-perovskite phase transition above room temperature.

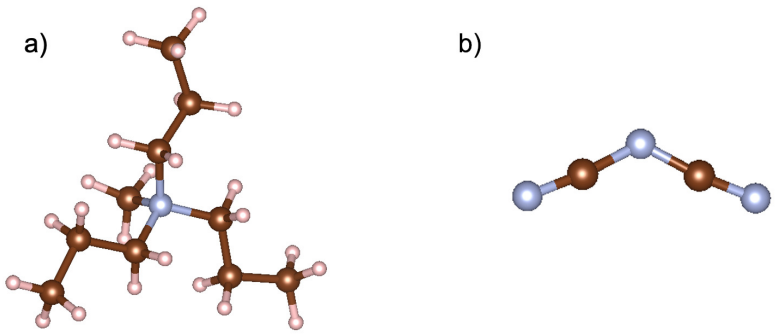


Figure 5.1: Structure of A and X site of perovskite $[(nPr)_3(CH_3)N]Ni(C_2N_3)_3$, a) $(nPr)_3(CH_3)N$ and b) $(C_2N_3)_3$. Colour scheme: C atoms are brown, N atoms are blue and H atoms are pink.

The first two sections of the results section focuses on the structural and thermodynamic nature of these phase transitions. In the latter sections, I focus on the thermodynamically stable rhombohedral phase and calculate the mechanical properties of the molecular perovskite series $[(nPr)_3(CH_3)N]M(C_2N_3)_3$, M = Mn, Co, Fe, Ni, Zn, Cd, Ba, Sr, Ca, Hg, or Mg) using DFT. We find a clear inverse relationship between the bulk modulus and B site Shannon radius, and the B-X bond length, with higher order perturbations to this dominant trend from ligand field stabilisation energy.

## 5.2 Computational details

The calculations are based on DFT as implemented in the VASP package [92, 93]. The exchange-correlation energy of electrons is treated within the generalized gradient approximation (GGA) with the functional by Perdew, Burke and Ernzerhof (PBE) [70]. In order to account for the limitations of the GGA to describe the d-orbitals of transition metals, we included Hubbard corrections for these orbitals (GGA+U), following the formalism introduced by Dudarev *et al.* [213]. Like in Chapter 3, the $U_{\text{eff}}$ parameters for Mn (4.0 eV), Co (3.3 eV), Fe (4.0 eV) and Ni (6.4 eV) were taken from the work by Wang *et al.* [120], where they were fitted so that GGA+U could reproduce the experimental oxidation energies in transition metal oxides. We also included dispersion corrections following Grimme's D3 scheme [84]. The projector augmented wave (PAW) method [78, 79] was used to describe the interactions between the valence electrons and the frozen cores, which consisted of orbitals up to 2p for C and N, and up to 3d for the transition metals. We used an energy cut-off of 520 eV to truncate the planewave expansion of the Kohn-Sham wavefunctions, which was 30% above the default cut-off for the employed PAW potentials, to minimise Pulay errors. Brillouin zone (BZ) integrations were performed by sampling the reciprocal space using $\Gamma-$ centred meshes of $4\times3\times2$ k-points with reference to orthorhombic unit cell and of $4 \times 4 \times 4$ k-points with reference to rhombohedral unit cell, which give similarly dense grids. Spin polarisation was allowed in all calculations to

properly describe the magnetic transition metal cations. Given the large size of the crystallographic unit cells, phonon dispersion and vibrational density of states were obtained from force constants calculated by systematic displacements of ionic positions only within the unit cell, via the Phonopy code [219].

## 5.3 Results and discussion

### 5.3.1 Experimental observations

The experiments in this work were performed by Dr. Gregor Kieslich's group at Technical University of Munich, Germany. They are summarised here to provide a reference for my computational work. $[N(C_3H_7)_3CH_3]Ni(C_2N_3)_3$ crystallises in the orthorhombic space group (*Pnma*) and is referred to as P(Ni)-I. The material crystallises in a perovskite structure where the metal centres are in an octahedral coordination with $[Ni(C_2N_3)_3]^-$ anions and the molecular A-site cation $[(C_3H_7)_3(CH_3)N]^+$ sits in the void of the pseudocubic $[Ni(C_2N_3)_3]^-$ network for charge balance. Positional disorder is observed for the A-site cation $[N(C_3H_7)_3CH_3]Ni(C_2N_3)_3$, with each propyl and methyl group disordered over two sites.

Subsequently, differential scanning calorimetry (DSC) was performed to screen for phase transitions (Figure 5.2). An irreversible crystalline-to-crystalline phase transition was observed from polymorph P(Ni)-I into a material referred to as P(Ni)-IIb at $T = 365$ K. An isostructural behavior was found along the series $[N(C_3H_7)_3CH_3]M(C_2N_3)_3$ with increasing transition temperature from manganese to nickel. Such an irreversible phase transition was observed for $[(NH_2)_3C]Mn(H_2POO)_3$, $((C_4H_9)_3(CH_3)N)Mn(C_2N_3)_3$ and $[(C_5H_{10})_2N]Cd(C_2N_3)_3$ [210]. For $[(NH_2)_3C]Mn(H_2POO)_3$, a single-crystal-to-single-crystal phase transition allowed for structure solution, showing an irreversible rearrangement of X-site molecules within the 3D $[Mn(H_2POO)_3]^-$ network as the underlying process [210]. Single crystals of P(Ni)-I break into a polycrystalline powder during the phase

transition. A high temperature crystallisation method at 370 K inspired by existing high-entropy nucleation routes [220] was applied to obtain single crystals of P(Ni)-IIb. P(Ni)-IIb adopts the perovskite structure in the rhombohedral space group $R\bar{3}c$. In P(Ni)-IIb, the A-site cation shows positional disorder, with all carbon atoms of the three propyl groups disordered over four positions and the methyl group disordered over two positions. The phase transition from P(Ni)-I to P(Ni)-IIb represents an irreversible perovskite-to-perovskite phase transition. The two polymorphs P(Ni)-I and P(Ni)-IIb differ in the disorder of the A-site cation.

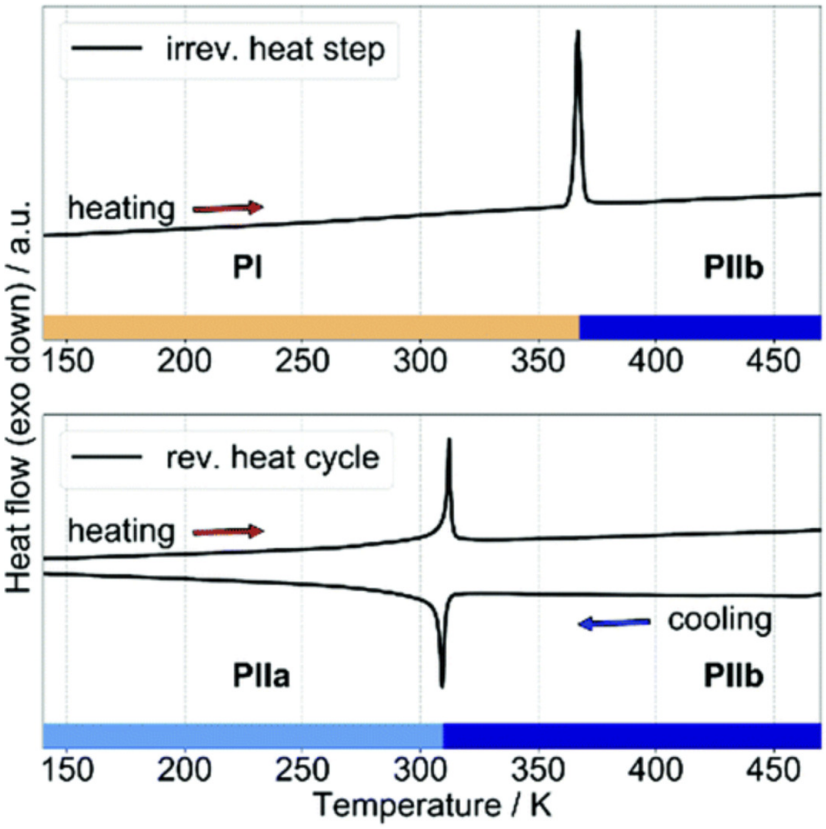


Figure 5.2: DSC traces of $[(nPr)_3(CH_3)N]Ni(C_2N_3)_3$. Shown are the heating step (top) and subsequent reversible cooling/heating cycle (bottom), highlighting the temperature range for the low-temperature and high-temperature phases with colour bars, respectively.

Following the traces of the DSC experiment, the irreversible heat event is followed by heat events that show existence of a reversible phase transition. Therefore, P(Ni)-IIb represents a high-temperature phase of $[[N(C_3H_7)_3CH_3]Ni(C_2N_3)_3]$ with a reversible phase

transition to a low-temperature phase assigned here as P(Ni)-IIa. P(Ni)-IIa crystallises in the polar space group R3c, with a completely ordered A-site, showing that the reversible phase transition, P(Ni)-IIa to P(Ni)-IIb is an order-disorder phase transition related to A-site cation. Such polar-to-nonpolar phase transitions, where A-site disorder introduces inversion symmetry, are well known for molecular perovskites [16, 221]. A complete description of the structural differences between the polymorphs and their tilt and shift patterns can be found in the article published [222]. In the next section of the chapter, I use first-principles simulations to underpin these experimental observations.

### 5.3.2 Relative phase stabilities

To explain the experimental observations, DFT calculations combined with lattice dynamic (LD) calculations were performed, probing the relative stabilities of the different perovskite polymorphs. At 0 K, *i.e.* in the absence of any entropic contributions, a comparison of relative stabilities between rhombohedral and orthorhombic phases shows that the rhombohedral polymorph P(M)-IIa is the thermodynamically stable phase when compared to P(M)-I (Figure 5.3a).

Adding zero-point vibrational contributions to the energy differences reinforces the stability of the rhombohedral *vs.* the orthorhombic phase. Since vibrational entropy can reverse thermodynamic stabilities at finite temperature [202, 209, 223], we calculate the vibrational free energy in the temperature range $T = 0{-}400$ K for all P(M)-I and P(M)-IIa phases. The phonon dispersion curves (Figure 5.4) show some imaginary frequencies which are normally associated with dynamic instabilities; however, a more in-depth analysis reveals that these imaginary frequencies are a numerical artefact from cell size effects for the LD simulations. The use of a single unit cell in the simulations, together with the softness of the low-frequency modes, led to numerical noise which translated into artificial imaginary modes in the phonon dispersion curves, away from the Brillouin centre.

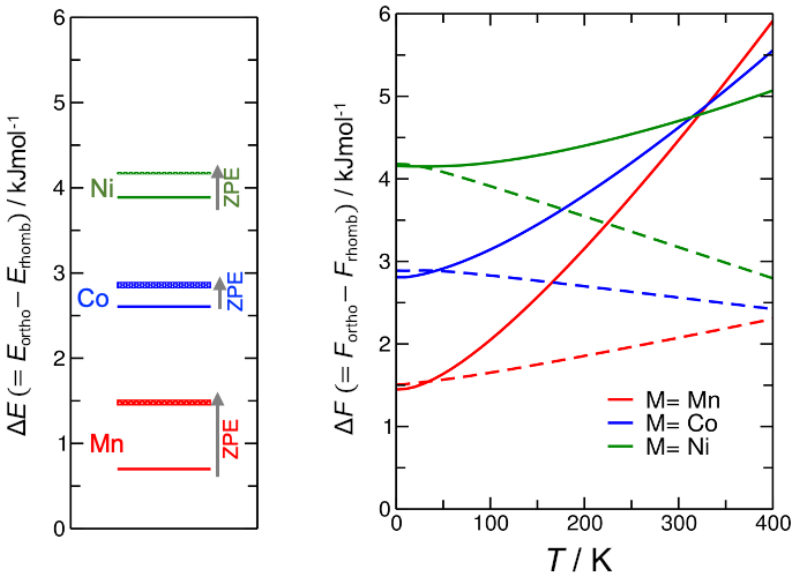


Figure 5.3: (a) Energy differences between orthorhombic and rhombohedral phases for each composition, with and without zero-point energy (ZPE) corrections. (b) Vibrational free energy differences between the phases vs. temperature. The width of the ZPE-corrected lines in (a) and the two types of line in (b) reflect the different results from two ways of dealing with the (spurious) imaginary modes: ignoring the imaginary contributions (solid lines), or counting them as real contributions (dashed lines).

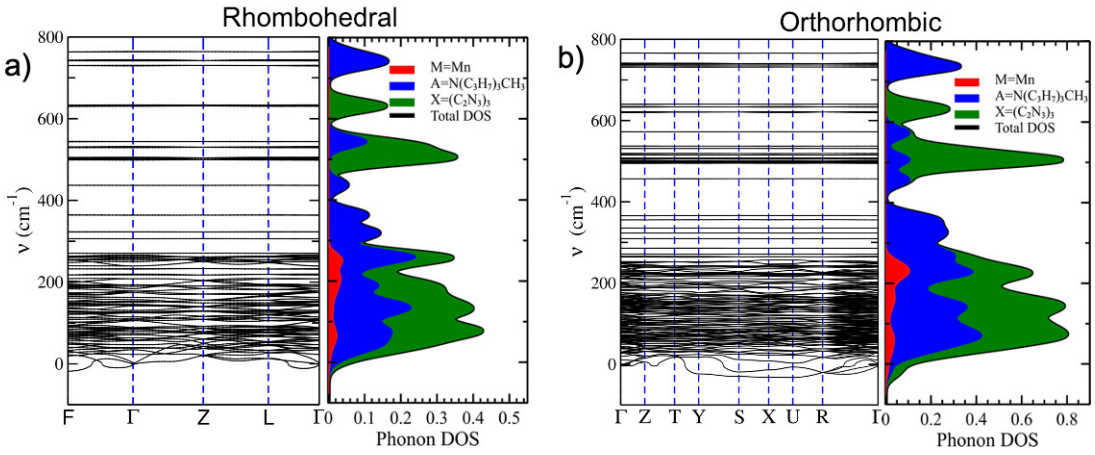


Figure 5.4: Phonon dispersion curves and partial density of states in the low-frequency region for the Mn-containing materials in a) the rhombohedral and b) the orthorhombic phase, calculated using a unit cell.

These imaginary frequencies could not be resolved by following the imaginary modes with ionic displacement in larger supercells (using the ModeMap code by Skelton *et al.* [224]). For example, the potential energy surfaces obtained by displacing the ions in the

direction of eigenvectors for lowest-frequency bands at the F point for the rhombohedral phase, or for the U point for the orthorhombic phase, using appropriate supercells, showed normal convexity with a minimum at the optimised structures for both phases (Figure 5.5). Tests performed on other high symmetry points gave similar results. We therefore conclude that both structures are dynamically stable, representing local minima of the potential energy surface, and phase transitions between these phases are required to go through a high-energy intermediate rather than occurring via a simple displacive mechanism.

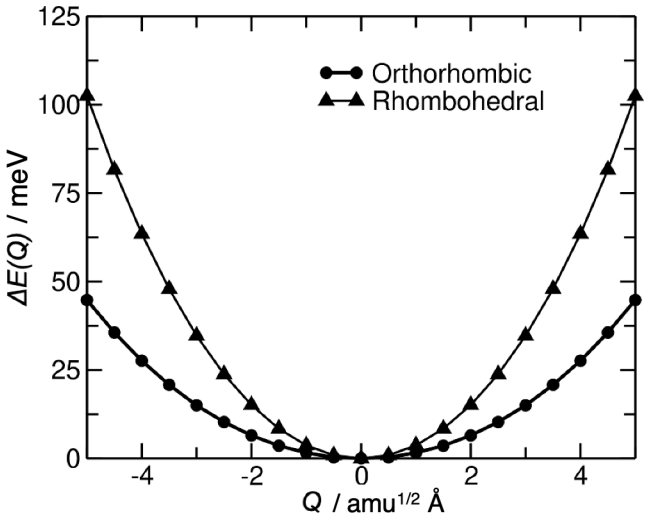


Figure 5.5: Potential energy surfaces in the direction of eigenvectors for lowest-frequency bands at the F point for the rhombohedral phase, and U point for the orthorhombic phase, using appropriate supercells.

Due to the spurious imaginary modes, which could not be renormalised, we make two approximations for obtaining vibrational entropies: one to ignore the modes in the expression for free energy, the other to treat the negative modes as their positive inverse. Figure 5.3b shows unequivocally that the rhombohedral phase is more stable across the range of temperature of interest here, regardless of how we consider the contribution from the artificial imaginary modes. Therefore, P(M)-II is the thermodynamically stable polymorph over the temperature range studied here, in excellent agreement with experimental observation, *i.e.* with the observation of crystallisation of this polymorph at higher temperature. Therefore, P(M)-I is the kinetic polymorph and its crystallisation seems to be

kinetically favoured at ambient temperatures. In the subsequent sections of this chapter, I focus on the thermodynamically stable rhombohedral phase (Figure 5.6). The comparison of DFT optimised lattice parameters of P(M)-II phase with those from experiments are shown in Table 5.1. The lattice parameters are in reasonable agreement with the experimental values, with the inclusion of the Hubbard U correction improving the outcomes to errors below 2%.

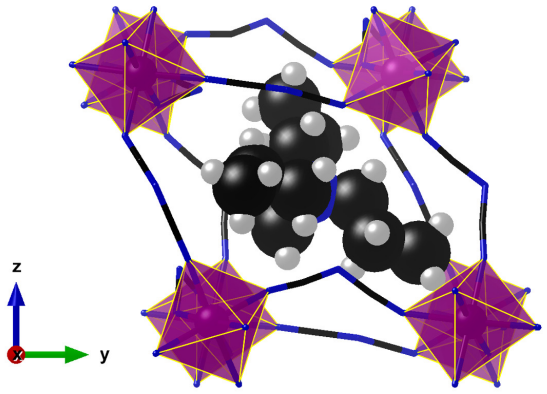


Figure 5.6: Crystal structure of $[N(C_3H_7)_3CH_3]M(C_2N_3)_3$ perovskite in rhombohedral phase (pseudocubic representation shown here), where M = Mn, Co or Ni, A site: $[N(C_3H_7)_3CH_3]$ and X: $(C_2N_3)$. Colour scheme: C atoms are black, N atoms are blue, H atoms are grey and M atoms are purple.

Table 5.1: Comparison of experimental and DFT geometries for the rhombohedral structure. Experimental values were measured at 100 K whereas the calculations ignore vibrational effects and therefore are formally at 0 K.

| | $M$ = Mn | | | $M$ = Co | | | $M$ = Ni | | |
|---|---|---|---|---|---|---|---|---|---|
| Parameter | Exp. | Theory | Error | Exp. | Theory | Error | Exp. | Theory | Error |
| $a$/Å | 10.36 | 10.28 | -0.77% | 10.26 | 10.19 | -0.68% | 10.22 | 10.16 | -0.58% |
| $\alpha$/deg | 76.47 | 77.24 | -1.0% | 76.28 | 77.13 | -1.11% | 76.01 | 76.76 | 0.98% |
| $V$/Å$^3$ | 1033.54 | 1017.39 | -1.56% | 1001.57 | 988.71 | -1.28% | 986.49 | 976.46 | -1.02% |

### 5.3.3 Mechanical properties

To calculate bulk modulus of the series $[(nPr)_3(CH_3)N]M(C_2N_3)_3$ with M= Mn, Co and Ni in rhombohedral R3c phase, we use a third-order Birch-Murnaghan equation of state

model [225, 226], with the pressure ($P$) and ($E$) variations as functions of volume ($V$):

$$P(V) = \frac{3B}{2}\left[\left(\frac{V_0}{V}\right)^{\frac{7}{3}} - \left(\frac{V_0}{V}\right)^{\frac{5}{3}}\right]\left\{1 + \frac{3}{4}(B' - 4)\left[\left(\frac{V_0}{V}\right)^{\frac{2}{3}} - 1\right]\right\} \tag{5.1}$$

$$E(V) = E_0 + \frac{9V_0B}{16}\left\{\left[\left(\frac{V_0}{V}\right)^{\frac{2}{3}} - 1\right]^3 B' + \left[\left(\frac{V_0}{V}\right)^{\frac{2}{3}} - 1\right]^2\left[6 - 4\left(\frac{V_0}{V}\right)^{\frac{2}{3}}\right]\right\} \tag{5.2}$$

where $V_0$ is the equilibrium volume, $B$ is the bulk modulus, $B'$ is the derivative of the bulk modulus with respect to pressure, and $E_0$ is the energy at the equilibrium volume. The bulk moduli was computed by fitting the DFT energy ($E$) and volume ($V$). The fitting of energy vs. volume points for Mn, Co and Ni containing system is shown in figure 5.7. For each point the structure was relaxed by optimising cell parameters and ionic coordinates at fixed volume. The fitting was largely insensitive to the value of pressure derivative, which was then fixed to $B' = 4.0$ for all compositions. The bulk moduli obtained at each composition are listed in Table 5.2. The calculations capture the experimental trend with slightly increasing value monotonically with atomic number from Mn to Ni. The difference between experimental and theoretical values of bulk modulus might be due to the underestimation of lattice parameters within the GGA+U theory, with the more tightly packed structures showing slightly greater moduli. The experimental lattice parameters are taken from structures at 100 K, while lattice parameters from DFT are formally at 0 K, ignoring any zero-point vibrational effects. Thus, the overestimation of bulk modulus is likely to be a consequence of the inverse relationship between total energy and volume.

Table 5.2: Bulk modulus ($B$) from theory and experiment. The experimental values ($T = 100$ K) were obtained by Kieslich's group.

| $B$/GPa | M = Mn | M = Co | M = Ni |
|---|---|---|---|
| *Theory* | 11.01±0.1 | 12.5±0.1 | 13.4±0.1 |
| *Expt.* | 6.00±0.27 | 8.02±0.38 | 10.31±0.55 |

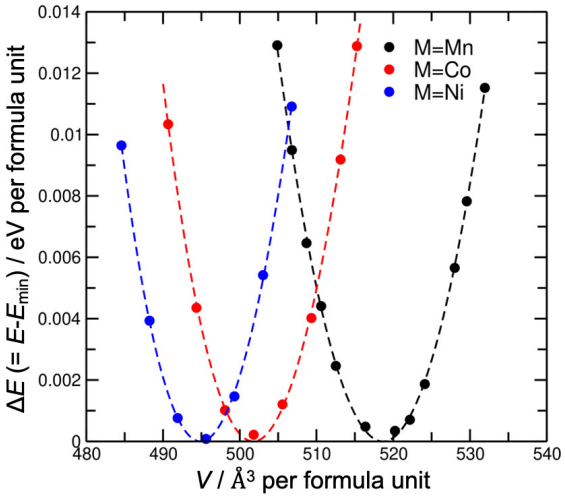


Figure 5.7: Fitted energy-volume curves from DFT calculations for $[N(C_3H_7)_3CH_3]M(C_2N_3)_3$ perovskites (M=Mn, Co and Ni).

### 5.3.4 Vibrational properties

The phonon density of states were calculated to get a deeper insight to the structural and chemical origins of the macroscopic trends in the bulk moduli. Figure 5.8a shows the phonon density of states (pDOS) for the three compositions, where the pDOS is decomposed into contributions from each of the A-site cation, the B-site metal and X-site linker anion. The three materials have qualitatively similar DOS, with the metal centre contribution only observed at low frequencies (up to 300 $cm^{-1}$) which is related to higher atomic mass of the M compared to the other species in the material. From the zone-centre vibrational frequencies, a clear hardening of the soft optical modes $\nu < 100$ $cm^{-1}$ is observed from Mn to Co and Ni (Figure 5.8b).

Figure 5.8c examines the contributions to the pDOS of the framework and A-site cation in order to better understand the origin of the differences. The soft modes are dominated by the M+X framework and not the A cations. Figure 5.8c clearly shows that the Mn-based material has the greatest pDOS at low frequency, followed by Co and then Ni. This trend in the low-frequency pDOS matches well with the trend in bulk modulus and supports the assertion that altering the framework by metal cation substitution provides a precise handle for tuning mechanical properties. This finding agrees with previous

work on the effects of B-X bonding on the mechanical properties of hybrid and molecular perovskites. It has previously been shown that stiffer B-X bonds achieved through greater ligand-field stabilisation [217, 227] or through greater electronegativity differences [201, 228, 229] result in stiffer materials. The direct effect of B-X bonding on the bulk modulus means that it is now interesting to establish how crystal chemistry can be used to alter the mechanical properties across a range different chemical environment.

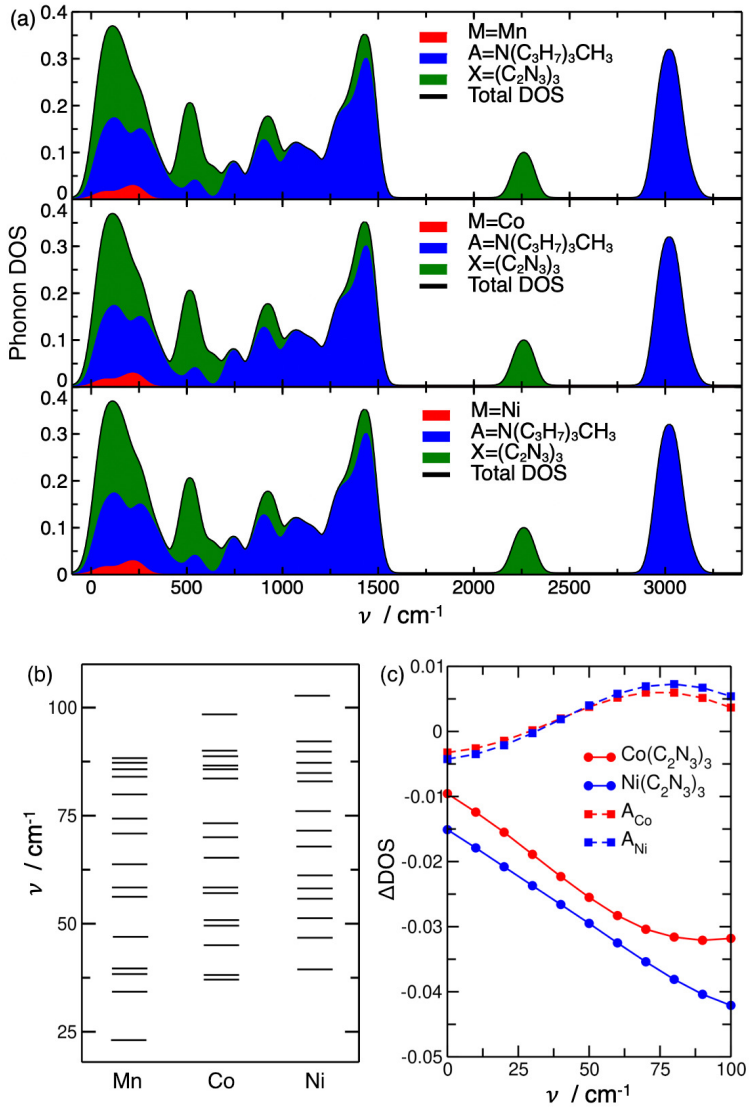


Figure 5.8: Vibrational properties of $[N(C_3H_7)_3CH_3]M(C_2N_3)_3$ perovskites (M = Mn, Co and Ni). (a) Phonon density of states, (b) zone-centre vibrational frequency of the soft modes for the three compositions, (c) $\Delta$DOS of the $Co(C_2N_3)_3$ and $Ni(C_2N_3)_3$ framework with $Mn(C_2N_3)_3$ framework as reference and $\Delta$DOS from the $A$ site of Co and Ni substituted system with respect to Mn containing system.

Having established the importance of the nature of the metal cation in determining the mechanical and vibrational properties in these molecular perovskite systems, the next question is whether this trend extends to other metal species and if examining more systems can allow us to draw stronger inferences about the origin of the effect. We have explored a range of hypothetical materials where the mechanical properties can be modified by cation substitution at the M site. We extend our study to systems containing other metals: Fe, Zn, Cd, Ba, Sr, Ca, Hg, or Mg, and determine their bulk modulus using DFT calculations. This is possible computationally as we can constrain the symmetry of the system so that the metal forms an octahedral complex with the $C_2N_3$ linker anion. Figure 5.9 shows the variation in bulk modulus for various metal systems. The Ba containing system has the lowest bulk modulus (8.27 GPa) with highest value of 13.39 GPa for Ni containing system among the systems of interest considered here. To examine the geometric factors determining the mechanical behavior in this molecular perovskite series, we see the variation in bulk modulus as a function of M-N bond length (metal-linker bond distance), $d$. This shows that larger the M-N bond distance, smaller the bulk modulus (Figure 5.9a). We further look at the variation in bulk modulus as a function of Shannon radius ($r$) of the M cation (Figure 5.9b). Aside from the very direct relation between cation Shannon radius and mechanical properties, we also see some secondary effects as perturbations in the major trend. For example, the bulk modulus of the Co material is significantly greater (5.4%) than that of the Zn material, despite their comparable Shannon radii. This observation can be linked to ligand field stabilisation energy (LFSE) – in $d^{10}$ Zn(II) the LFSE is zero, but in $d^5$ Co (II) it is 71.5 kJ/mol [200] and is also reflected in a shortened Co-X bond. This finding is similar to the situation in double perovskites where M-X bonding is directly proportional to the Young's modulus [228]. However, it is different to what is observed in pure halide perovskites where the Young's modulus is inversely related to the Pb-X bond distance, but is more affected by electronegativity differences [228].

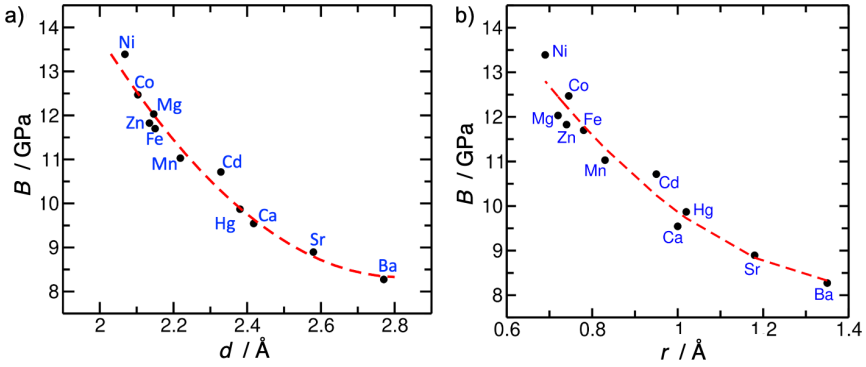


Figure 5.9: Bulk modulus, $B$, as a function of (a) equilibrium metal-linker bond distance, $d$, and (b) Shannon radius, $r$, of $M$ cations for $[N(C_3H_7)_3CH_3]M(C_2N_3)_3$ perovskites.

## 5.4 Conclusion

In this chapter, I explored the molecular perovskite series $[(nPr)_3(CH_3)N]M(C_2N_3)_3$ with M = Mn, Co, Ni. Depending on the synthetic conditions, different perovskite polymorphs can be obtained, and thermal treatment of the metastable polymorph P(M)-I leads to an irreversible perovskite-to-perovskite phase transition to P(M)-II. The P(M)-II polymorph exhibits a reversible order–disorder phase transition (PIIa–PIIb), which shows promising characteristics in terms of barocaloric properties. Density functional theory calculations show that for the whole stability temperature range the rhombohedral polymorph P(M)-II represents the thermodynamically more stable phase. The absence of actual imaginary modes further suggests that the transformation goes through a high-energy transition state as underlying mechanism of the irreversible phase transition.

The mechanical and vibrational properties of the molecular perovskite series are calculated, which are of importance for the potential application of these materials for barocaloric applications. The bulk modulus depends on the phonon density of states of the M+X framework and specially the metal-linker bond. Our analysis shows that the material with softest phonon modes corresponds to the material with lowest bulk modulus. Given the importance of the metal cation in determining the vibrational and mechanical properties we extend our study to a series of hypothetical materials with other metals in oxidation state II: Fe, Zn, Cd, Ba, Sr, Ca, Hg, and Mg. These calculations reveal clear

relationship between the metal-linker bond length and the bulk modulus. Furthermore, we show that the Shannon radius of a metal, which can be known *a priori*, without calculations or experiments, is a good descriptor for how the bulk modulus will depend on composition, with some modifications possible from ligand-field stabilisation energy for example.

The results presented in figure 5.9b provide a starting for rational materials design of molecular perovskites with tailored mechanical properties. Other factors such as the preferred crystal structure, presence of defects, microstructure and vibrational properties will also contribute to the overall mechanical properties of the systems. However, to a first order it should be possible to carefully change the mechanical properties by metal substitution. We also emphasise that metal does not need to be substituted completely; solid solutions are a powerful approach to continuously tailoring material properties and we expect that in these systems solid solutions could be a promising materials design strategy.

# Chapter 6

# Conclusions and Future work

## 6.1 Conclusions from previous chapters

In this thesis, I have presented a first-principles modelling study of several functional perovskites. The perovskites studied here are not only of technological importance, but also fundamentally interesting as they exhibit unusual phenomena involving fascinating physics. I explore and develop a thorough understanding of inorganic ($BiCo_xFe_{1-x}O_3$ and PMN-PT), HOIP ($(FAPbI_3)_{0.875}(MAPbBr_3)_{0.125}$) and molecular ($[(nPr)_3(CH_3N)]M(C_2N_3)_3$ with nPr= n-propyl) perovskites. I have modelled a wide range of properties, including band structure and alignment, phonon dispersion, ferroelectric polarisation, cation disorder, and bulk moduli. To achieve this, I have employed a combination of first-principles calculations based on DFT and AIMD.

This thesis illustrates the amazing chemical versatility of the perovskite $ABX_3$ structure, which is able to accommodate wildly different species in the cation (A, B) and anion (X) sites. The species can be just atomic like in the inorganic perovskites $BiFeO_3$ or $PbMg_{1/3}Nb_{2/3}O_3$ (Chapter 3), molecular like in the $[(nPr)_3(CH_3)N]M(C_2N_3)_3$ materials explored in Chapter 5, or hybrid like the $MAPbBr_3$ and $FAPbI_3$ compounds considered in Chapter 4. In Chapter 3, the response of the multiferroic perovskite $BiFeO_3$ to Co

substitution was discussed in detail considering the structural, electronic, magnetic, ferroelectric and thermodynamic aspects using DFT. Co substitution in $BiFeO_3$ significantly reduces the band gap of the system, from 2.9 eV to ∼2.1 eV simultaneously enhancing the spontaneous polarisation. This large enhancement of ferroelectricity would further promote effective charge carrier separation in applications such as photocatalysis or photovoltaics. The potential of Co-substituted $BiFeO_3$ in photocatalytic applications is briefly discussed by calculating the band alignment. The final section of this chapter focused on the ferroelectric properties of a relaxor ferroelectric perovskite, PMN-PT which exhibits a tetragonal-monoclinic phase transition accompanied by a giant piezoelectric response.

Following this, I focused on the HOIPs which have gained attention over the past decades for the high power conversion efficiency of the perovskite solar cells. Chapter 4 employs methods of AIMD to calculate the structural, electronic, thermodynamic and vibrational properties of mixed-cation mixed-anion perovskite, $(FAPbI_3)_{0.875}(MAPbBr_3)_{0.125}$. An atomic scale model of the solid solution is proposed and all the properties are compared to the end compounds $MAPbBr_3$ and $FAPbI_3$. The computed properties have been shown to reproduce the available experimental measurements, such as bandgaps, lattice constant, cation orientation dynamics, and thermodynamic stability. A detailed understanding of $(FAPbI_3)_{0.875}(MAPbBr_3)_{0.125}$ perovskite solid solution is thus obtained.

In Chapter 5, I explored the molecular perovskite series $[(nPr)_3(CH_3)N]M(C_2N_3)_3$ with M = Mn, Co, Ni which shows promising characteristics in terms of barocaloric properties. Using DFT, the phase stability is computed at the temperatures of interest and it is established that the rhombohedral phase is the thermodynamically stable phase. The mechanical and vibrational properties of the molecular perovskite series are calculated which shows the dependence of bulk modulus on the phonon density of states of M+X framework and especially the metal-linker bond. The material with the softest phonon modes corresponds to the material with lowest bulk modulus. A clear relationship between between the metal-linker bond length and the bulk modulus is established using a series of hypothetical materials with different metal ($M^{2+}$) centres. The relationship between

bulk modulus and Shannon radius provides a starting point for rational material design with tailored mechanical properties.

While the materials examined in the chapters of this thesis are different in chemical properties, they all exhibit a rich interplay between structure, symmetry, and dynamics. The compositional ratios and the 3D topology of corner-sharing octahedra are common, but the distortions from the high-symmetry cubic perovskite structure are often crucial to the functional properties. In $BiFeO_3$ and PMN-PT, the non-centrosymmetric space groups are essential for the ferroelectric behaviour. Although I did not discuss electric polarisation in the hybrid organic-inorganic halide perovskites of Chapter 4, it is known that polarisation may play an important role in the high performance of those perovskites in photovoltaic cells [230]. Similarly, the pressure-induced symmetry transitions in the molecular perovskites of Chapter 5 are key to their barocaloric applications. Our results also show how the vibrational and dynamic behaviour are important to understand the properties of perovskites. In the work presented in Chapter 4, for example, we showed that the rotation of the organic cations is more strongly hindered in the mixed structure in comparison with the pure compounds, a phenomenon that might affect the stability of these important solid solutions. In Chapter 5, careful consideration of the vibrational dynamics of the perovskites was essential to understand the relationship between the phases. The study of $BiFeO_3$, $(FAPbI_3)_{0.875}(MAPbBr_3)_{0.125}$, and $PbMg_{1/3}Nb_{2/3}O_3{-}PbTiO_3$ solid solutions have illustrated an additional degree of freedom (the composition $x$) to tune the properties of these materials. If the configurational thermodynamics is important, like in the case of investigating phase separation in Co-substituted $BiFeO_3$, one must explicitly evaluate configurational energies in an ensemble, and in this case the vibrational contributions must be ignored to keep the computational cost manageable. If dynamic aspects must be taken into account, the computational study of such solid solutions has to be simplified by using representative structures, for example the SQS used to model $(FAPbI_3)_{0.875}(MAPbBr_3)_{0.125}$. The simultaneous consideration of different dimensions of complexity is perhaps the greatest challenge in the computer simulation of functional

perovskites.

## 6.2 Future work

In the study of Co-substituted $BiFeO_3$, one aspect that remained pending for future investigation is how the $U_{\text{eff}}$ correction applied in the GGA+U method affects the predicted ferroelectric polarisation. The polarisation calculations using hybrid functionals for this system were computationally expensive. Hence, the effect of different $U_{\text{eff}}$ parameters on the polarisation of the system needs to be explored. This is important to reconcile different theoretical studies. Using the same approach, the ferroelectric properties of the $(FAPbI_3)_{0.875}(MAPbBr_3)_{0.125}$ solid solution can be explored as the ferroelectric properties of these hybrid perovskites are important for photovoltaic applications.

Having established the efficacy of DFT calculations in predicting the bulk modulus of molecular perovskites with different $M^{2+}$ cation, I plan to extend this idea to predict the bulk modulus of perovskite materials using machine learning (ML). ML has emerged as a powerful tool in material science [231, 232] as it accelerates the search for materials with desired targeted properties. Although we are initially interested in the prediction of bulk moduli, ML techniques can be also used to accelerate the prediction of other properties of relevance for this thesis, for example, bandgaps or phonon related properties, as illustrated by recent work in our research group [233–235]. The high computational cost incurred by DFT-based simulations requires access to high-performance computers. ML based methods has the potential to reduce computational cost by several orders of magnitude compared to the DFT based methods [236–238]. I have done some preliminary work, which I would like to extend in the future, using MatErials Graph Network (MEGNet) developed by Chen *et al.* [239] for accurate prediction of bulk modulus of perovskite materials. MEGNet can be trained by using the crystal structure of materials alone. I used the available data of bulk modulus of materials from JARVIS database [240]. The dataset comprises a collection of compounds with their structural parameters and bulk

moduli (19441 compounds whose bulk modulus is known). The dataset is divided into three parts, training, validation and test. For initial calculations, 60% of the dataset was used for training and the remaining were equally divided into validation and test dataset. The MEGNet model was trained on the training set and the validation loss is monitored during training. The training is stopped when the validation loss does not improve for 150 consecutive epochs (Figure 6.1(a)). The convergence was achieved within 500 epochs. The trained model is used to predict the bulk modulus of the test set. Figure 6.1(b) shows the plot of predicted *vs.* true data for the test set (3987 structures). The materials with small bulk modulus had larger error. These are preliminary results and require further investigation which I plan to do in future. A complete plan of the future work on this project is given below:

- Use unlockGNN with the trained MEGNet model to obtain learned representations of the perovskite materials.
- Split the perovskite dataset into a training set and a exploration set.
- Train a Gaussian process (GP) model using the learned representations to predict the bulk moduli (on the training set of perovskite materials).
- Using the trained GP, do Bayesian optimisation of the exploration set.

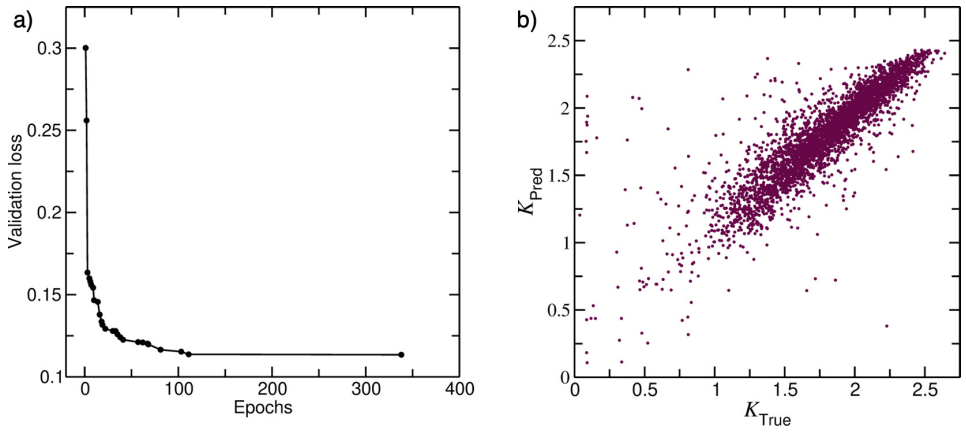


Figure 6.1: (a) Validation loss vs. epochs for the training set, (b) Predicted vs. true value of bulk modulus for the test set. The values are in log10(GPa) scale.

As mentioned above, there is large computational cost barrier in the simulation of the complexity of perovskites materials. I believe that ML will be an essential ingredient to overcome that barrier in future computational studies of these fascinating materials.

# Bibliography


[1] P. Hohenberg and W. Kohn, "Inhomogeneous electron gas", *Phys. Rev.* **136**, pp. B864–B871 (1964).

[2] W. Kohn and L. J. Sham, "Self-consistent equations including exchange and correlation effects", *Phys. Rev.* **140**, pp. A1133–A1138 (1965).

[3] David P. Landau and K. Binder, *A Guide to Monte Carlo Simulations in Statistical Physics*, Cambridge University Press Cambridge (2014).

[4] R. Iftimie, P. Minary, and M. E. Tuckerman, "Ab initio molecular dynamics: Concepts, recent developments, and future trends", *Proceedings of the National Academy of Sciences* **102**, pp. 6654–6659 (2005).

[5] R. Ali and M. Yashima, "Space group and crystal structure of the perovskite $CaTiO_3$ from 296 to 1720 K", *Journal of Solid State Chemistry* **178**, pp. 2867–2872 (2005).

[6] V. M. Goldschmidt, "Die gesetze der krystallochemie", *Naturwissenschaften* **14**, pp. 477–485 (1926).

[7] Y. A. Abramov, V. G. Tsirelson, V. E. Zavodnik, S. A. Ivanov, and Brown I. D., "The chemical bond and atomic displacements in $SrTiO_3$ from X-ray diffraction analysis", *Acta Crystallographica Section B* **51**, pp. 942–951 (1995).

[8] A. Okazaki and Y. Suemune, "The crystal structure of $KCuF_3$", *Journal of the Physical Society of Japan* **16**, pp. 176–183 (1961).

[9] B. C. Frazer, H. R. Danner, and R. Pepinsky, "Single-crystal neutron analysis of tetragonal $BaTiO_3$", *Phys. Rev.* **100**, pp. 745–746 (1955).

[10] H. D. Megaw and J. D. Bernal, "Temperature changes in the crystal structure of barium titanium oxide", *Proceedings of the Royal Society of London. Series A. Mathematical and Physical Sciences* **189**, pp. 261–283 (1947).

[11] I. B. Bersuker, "Pseudo Jahn-Teller origin of perovskite multiferroics, magnetic-ferroelectric crossover, and magnetoelectric effects: The $d^0-d^{10}$ problem", *Phys. Rev. Lett.* **108**, pp. 137202 (2012).

[12] N. W. Thomas, "Crystal structure–physical property relationships in perovskites", *Acta Crystallographica Section B* **45**, pp. 337–344 (1989).

[13] N. W. Thomas, "A new global parameterization of perovskite structures", *Acta Crystallographica Section B* **54**, pp. 585–599 (1998).

[14] M. Johnsson and P. Lemmens, *Crystallography and Chemistry of Perovskites*, John Wiley & Sons, Ltd (2007).

[15] X. Liu, R. Hong, and C. Tian, "Tolerance factor and the stability discussion of $ABO_3$-type ilmenite", *Journal of Materials Science-materials in Electronics* **20**, pp. 323–327 (2009).

[16] A. M. Glazer, "The classification of tilted octahedra in perovskites", *Acta Crystallographica Section B* **28**, pp. 3384–3392 (1972).

[17] S. Sasaki, C. T. Prewitt, J. D. Bass, and W. A. Schulze, "Orthorhombic perovskite $CaTiO_3$ and $CdTiO_3$: structure and space group", *Acta Crystallographica Section C* **43**, pp. 1668–1674 (1987).

[18] T. Asada and Y. Koyama, "Coexistence of ferroelectricity and antiferroelectricity in lead zirconate titanate", *Phys. Rev. B* **70**, pp. 104105 (2004).

[19] J. Wang, J. B. Neaton, H. Zheng, V. Nagarajan, S. B. Ogale, B. Liu, D. Viehland, V. Vaithyanathan, D. G. Schlom, U. V. Waghmare, N. A. Spaldin, K. M. Rabe, M. Wuttig, and R. Ramesh, "Epitaxial $BiFeO_3$ multiferroic thin film heterostructures", *Science* **299**, pp. 1719–1722 (2003).

[20] H. Jaffe, "Titanate ceramics for electromechanical purposes", *Industrial & Engineering Chemistry* **42**, pp. 264–268 (1950).

[21] J. Rouquette, J. Haines, V. Bornand, M. Pintard, Ph. Papet, C. Bousquet, L. Konczewicz, F. A. Gorelli, and S. Hull, "Pressure tuning of the morphotropic phase boundary in piezoelectric lead zirconate titanate", *Phys. Rev. B* **70**, pp. 014108 (2004).

[22] Y. Moritomo, A. Asamitsu, H. Kuwahara, and Y. Tokura, "Giant magnetoresistance of manganese oxides with a layered perovskite structure", *Nature* **380**, pp. 141–144 (1996).

[23] J. Loudon, N. Mathur, and P. Midgley, "Charge-ordered ferromagnetic phase in $La_{0.5}Ca_{0.5}MnO_3$", *Nature* **420**, pp. 797–800 (2002).

[24] D. Sun, Y. Zhang, D. Wang, W. Song, X. Liu, J. Pang, D. Geng, Y. Sang, and H. Liu, "Microstructure and domain engineering of lithium niobate crystal films for integrated photonic applications", *Light: Science Applications* **9**, pp. 197 (2020).

[25] E.L. Wooten, K.M. Kissa, A. Yi-Yan, E.J. Murphy, D.A. Lafaw, P.F. Hallemeier, D. Maack, D.V. Attanasio, D.J. Fritz, G.J. McBrien, and D.E. Bossi, "A review of lithium niobate modulators for fiber-optic communications systems", *IEEE Journal of Selected Topics in Quantum Electronics* **6**, pp. 69–82 (2000).

[26] A. Filippetti and N. A. Hill, "First principles study of structural, electronic and magnetic interplay in ferroelectromagnetic yttrium manganite", *Journal of Magnetism and Magnetic Materials* **236**, pp. 176–189 (2001).

[27] M. Fiebig, T. Lottermoser, D. Fröhlich, A. Goltsev, and R. Pisarev, "Observation of coupled magnetic and electric domains", *Nature* **419**, pp. 818–20 (2002).

[28] N. Fujimura, T. Ishida, T. Yoshimura, and T. Ito, "Epitaxially grown $YMnO_3$ film: New candidate for nonvolatile memory devices", *Applied Physics Letters* **69**, pp. 1011–1013 (1996).

[29] N. A. Hill and K. M. Rabe, "First-principles investigation of ferromagnetism and ferroelectricity in bismuth manganite", *Phys. Rev. B* **59**, pp. 8759–8769 (1999).

[30] R. Seshadri and N. A. Hill, "Visualizing the role of Bi 6s "lone pairs" in the off-center distortion in ferromagnetic $BiMnO_3$", *Chemistry of Materials* **13**, pp. 2892–2899 (2001).

[31] A. Moreira dos Santos, S. Parashar, A.R. Raju, Y.S. Zhao, A.K. Cheetham, and C.N.R. Rao, "Evidence for the likely occurrence of magnetoferroelectricity in the simple perovskite, $BiMnO_3$", *Solid State Communications* **122**, pp. 49–52 (2002).

[32] J. Y. Son, Bog G. Kim, C. H. Kim, and J. H. Cho, "Writing polarization bits on the multiferroic $BiMnO_3$ thin film using kelvin probe force microscope", *Applied Physics Letters* **84**, pp. 4971–4973 (2004).

[33] H Béa, M Gajek, M Bibes, and A Barthélémy, "Spintronics with multiferroics", *Journal of Physics: Condensed Matter* **20**, pp. 434221 (2008).

[34] G. Catalan and J. F. Scott, "Physics and applications of bismuth ferrite", *Advanced Materials* **21**, pp. 2463–2485 (2009).

[35] S. Zhang and F. Li, "High performance ferroelectric relaxor-$PbTiO_3$ single crystals: Status and perspective", *Journal of Applied Physics* **111**, pp. 031341 (2012).

[36] E. Sun and W. Cao, "Relaxor-based ferroelectric single crystals: Growth, domain engineering, characterization and applications", *Progress in Materials Science* **65**, pp. 124–210 (2014).

[37] R. D. Shannon, "Revised effective ionic radii and systematic studies of interatomic distances in halides and chalcogenides", *Acta Crystallographica Section A* **32**, pp. 751–767 (1976).

[38] H. Zhou, Q. Chen, G. Li, S. Luo, T.-b. Song, H.-S. Duan, Z. Hong, J. You, Y. Liu, and Y. Yang, "Interface engineering of highly efficient perovskite solar cells", *Science* **345**, pp. 542–546 (2014).

[39] G. Xing, N. Mathews, S. Sun, S. S. Lim, Y. M. Lam, M. Grätzel, S. Mhaisalkar, and T. C. Sum, "Long-range balanced electron- and hole-transport lengths in organic-inorganic $CH_3NH_3PbI_3$", *Science* **342**, pp. 344–347 (2013).

[40] S. D. Stranks, G. E. Eperon, G. Grancini, C. Menelaou, M. J. P. Alcocer, T. Leijtens, L. M. Herz, A. Petrozza, and H. J. Snaith, "Electron-hole diffusion lengths exceeding 1 micrometer in an organometal trihalide perovskite absorber", *Science* **342**, pp. 341–344 (2013).

[41] T. Baikie, Y. Fang, J. M. Kadro, M. Schreyer, F. Wei, S. G. Mhaisalkar, M. Graetzel, and T. J. White, "Synthesis and crystal chemistry of the hybrid perovskite $(CH_3NH_3)PbI_3$ for solid-state sensitised solar cell applications", *J. Mater. Chem. A* **1**, pp. 5628–5641 (2013).

[42] A. Halder, D. Choudhury, S. Ghosh, A. S. Subbiah, and S. K. Sarkar, "Exploring thermochromic behavior of hydrated hybrid perovskites in solar cells", *The Journal of Physical Chemistry Letters* **6**(16), pp. 3180–3184 (2015).

[43] T.-B. Song, Q. Chen, H. Zhou, C. Jiang, H.-H. Wang, Y. (Michael) Yang, Y. Liu, J. You, and Y. Yang, "Perovskite solar cells: film formation and properties", *J. Mater. Chem. A* **3**, pp. 9032–9050 (2015).

[44] M. K. Gangishetty, R. W. J. Scott, and T. L. Kelly, "Effect of relative humidity on crystal growth, device performance and hysteresis in planar heterojunction perovskite solar cells", *Nanoscale* **8**, pp. 6300–6307 (2016).

[45] Z. Song, N. Shrestha, S. C. Watthage, G. K. Liyanage, Z. S. Almutawah, R. H. Ahangharnejhad, A. B. Phillips, R. J. Ellingson, and M. J. Heben, "Impact of moisture on photoexcited charge carrier dynamics in methylammonium lead halide perovskites", *The Journal of Physical Chemistry Letters* **9**, pp. 6312–6320 (2018).

[46] L. K. Ono, E. J. Juarez-Perez, and Y. Qi, "Progress on perovskite materials and solar cells with mixed cations and halide anions", *ACS Applied Materials & Interfaces* **9**, pp. 30197–30246 (2017).

[47] W.-J. Xu, S.-L. Chen, Z.-T. Hu, R.-B. Lin, Y.-J. Su, W.-X. Zhang, and X.-M. Chen, "The cation-dependent structural phase transition and dielectric response in a family of cyano-bridged perovskite-like coordination polymers", *Dalton Trans.* **45**, pp. 4224–4229 (2016).

[48] M. Maczka, I. E. Collings, F. F. Leite, and W. Paraguassu, "Raman and single-crystal x-ray diffraction evidence of pressure-induced phase transitions in a perovskite-like framework of $[(C_3H_7)_4N]$ $[Mn(N(CN)_2)_3]$", *Dalton Trans.* **48**, pp. 9072–9078 (2019).

[49] A. Kudo and Y. Miseki, "Heterogeneous photocatalyst materials for water splitting", *Chem. Soc. Rev.* **38**, pp. 253–278 (2009).

[50] Y. Huang, J. Liu, Y. Deng, Y. Qian, X. Jia, M. Ma, C. Yang, K. Liu, Z. Wang, S. Qu, and Z. Wang, "The application of perovskite materials in solar water splitting", *Journal of Semiconductors* **41**, pp. 011701 (2020).

[51] K. Iwashina and A. Kudo, "Rh-doped $SrTiO_3$ photocatalyst electrode showing cathodic photocurrent for water splitting under visible-light irradiation", *Journal of the American Chemical Society* **133**, pp. 13272–13275 (2011).

[52] Md Moniruddin, B. Ilyassov, X. Zhao, E. Smith, T. Serikov, N. Ibrayev, R. Asmatulu, and N. Nuraje, "Recent progress on perovskite materials in photovoltaic and water splitting applications", *Materials Today Energy* **7**, pp. 246–259 (2018).

[53] M.A. Khan, M.A. Nadeem, and H. Idriss, "Ferroelectric polarization effect on surface chemistry and photo-catalytic activity: A review", *Surface Science Reports* **71**, pp. 1–31 (2016).

[54] W. Yang, Y. Yu, M. B. Starr, X. Yin, Z. Li, A. Kvit, S. Wang, P. Zhao, and X. Wang, "Ferroelectric polarization-enhanced photoelectrochemical water splitting in $TiO_2$–$BaTiO_3$ core–shell nanowire photoanodes", *Nano Letters* **15**, pp. 7574–7580 (2015).

[55] NREL cell efficiency chart, "https://www.nrel.gov/pv/cell-efficiency.html".

[56] A. Kojima, K. Teshima, Y. Shirai, and T. Miyasaka, "Organometal halide perovskites as visible-light sensitizers for photovoltaic cells", *Journal of the American Chemical Society* **131**, pp. 6050–6051 (2009).

[57] Z. Chen, Q. Dong, Y. Liu, C. Bao, Y. Fang, Y. Lin, S. Tang, Q. Wang, X. Xiao, Y. Bai, Y. Deng, and J. Huang, "Thin single crystal perovskite solar cells to harvest below-bandgap light absorption", *Nature Communications* **8** (2017).

[58] M. Baranowski and P. Plochocka, "Excitons in metal-halide perovskites", *Advanced Energy Materials* **10**, pp. 1903659 (2020).

[59] J. J. Yoo, S. S. Shin, and J. Seo, "Toward efficient perovskite solar cells: Progress, strategies, and perspectives", *ACS Energy Letters* **7**(6), pp. 2084–2091 (2022).

[60] A. Fakharuddin, F. De Rossi, T. M. Watson, L. Schmidt-Mende, and R. Jose, "Research update: Behind the high efficiency of hybrid perovskite solar cells", *APL Materials* **4**(9), pp. 091505 (2016).

[61] X Moya, S Kar-Narayan, and N Mathur, "Caloric materials near ferroic phase transitions", *Nature materials* **13**, pp. 439–50 (2014).

[62] L. Mañosa and A. Planes, "Materials with giant mechanocaloric effects: Cooling by strength", *Advanced Materials* **29**, pp. 1603607 (2017).

[63] E. Bonnot, R. Romero, L. Mañosa, E. Vives, and A. Planes, "Elastocaloric effect associated with the martensitic transition in shape-memory alloys", *Phys. Rev. Lett.* **100**, pp. 125901 (2008).

[64] Pol Lloveras, Enric Stern-Taulats, Maria Barrio, Josep Tamarit, S Crossley, W Li, V Pomjakushin, Antoni Planes, Ll Mañosa, N Mathur, and X Moya, "Giant barocaloric effect at low pressure in ferrielectric ammonium sulphate", *Nature communications* **6**, pp. 8801 (2015).

[65] A. S. Mischenko, Q. Zhang, J. F. Scott, R. W. Whatmore, and N. D. Mathur, "Giant electrocaloric effect in thin-film $PbZr_{0.95}Ti_{0.05}O_3$", *Science* **311**, pp. 1270–1271 (2006).

[66] B. Neese, B. Chu, S.-G. Lu, Y. Wang, E. Furman, and Q. M. Zhang, "Large electrocaloric effect in ferroelectric polymers near room temperature", *Science* **321**, pp. 821–823 (2008).

[67] V. K. Pecharsky and K. A. Gschneidner, Jr., "Giant magnetocaloric effect in $Gd_5(Si_2Ge_2)$", *Phys. Rev. Lett.* **78**, pp. 4494–4497 (1997).

[68] J. Bermúdez-García, M. Sánchez Andújar, S. Castro-Garcia, J. López Beceiro, R. Artiaga, and M. Senaris-Rodriguez, "Giant barocaloric effect in the ferroic organic-inorganic hybrid [TPrA][$Mn(dca)_3$] perovskite under easily accessible pressures", *Nature Communications* **8**, pp. 15715 (2017).

[69] J. Salgado-Beceiro, A. Nonato, R. X. Silva, A. García-Fernández, M. Sánchez-Andújar, S. Castro-García, E. Stern-Taulats, M. A. Señarís-Rodríguez, X. Moya, and J. M. Bermúdez-García, "Near-room-temperature reversible giant barocaloric effects in $[(CH_3)_4N]Mn[N_3]_3$ hybrid perovskite", *Mater. Adv.* **1**, pp. 3167–3170 (2020).

[70] J. P. Perdew, K. Burke, and M. Ernzerhof, "Generalized gradient approximation made simple", *Phys. Rev. Lett.* **77**, pp. 3865–3868 (1996).

[71] J. P. Perdew, A. Ruzsinszky, G. I. Csonka, O. A. Vydrov, G. E. Scuseria, L. A. Constantin, X. Zhou, and K. Burke, "Restoring the density-gradient expansion for exchange in solids and surfaces", *Phys. Rev. Lett.* **100**, pp. 136406 (2008).

[72] B. Hammer, L. B. Hansen, and J. K. Nørskov, "Improved adsorption energetics within density-functional theory using revised perdew-burke-ernzerhof functionals", *Phys. Rev. B* **59**, pp. 7413–7421 (1999).

[73] J. Heyd, G. E. Scuseria, and M. Ernzerhof, "Hybrid functionals based on a screened coulomb potential", *J. Chem. Phys.* **118**, pp. 8207–8215 (2003).

[74] F. Bloch, "Über die Quantenmechanik der Elektronen in Kristallgittern", *Zeitschrift fur Physik* **52**, pp. 555–600 (1929).

[75] W. Sun, *Heavy metal compounds and hydrogen storage materials from ab initio calculations*, PhD thesis (2013).

[76] D. R. Hamann, M. Schlüter, and C. Chiang, "Norm-conserving pseudopotentials", *Phys. Rev. Lett.* **43**, pp. 1494–1497 (1979).

[77] D. Vanderbilt, "Soft self-consistent pseudopotentials in a generalized eigenvalue formalism", *Phys. Rev. B* **41**, pp. 7892–7895 (1990).

[78] G. Kresse and D. Joubert, "From ultrasoft pseudopotentials to the projector augmented-wave method", *Phys. Rev. B* **59**, pp. 1758–1775 (1999).

[79] P. E. Blöchl, "Projector augmented-wave method", *Phys. Rev. B* **50**, pp. 17953–17979 (1994).

[80] P. Hobza, J. šponer, and T. Reschel, "Density functional theory and molecular clusters", *J. Comput. Chem.* **16**, pp. 1315–1325 (1995).

[81] M. J. Allen and D. J. Tozer, "Helium dimer dispersion forces and correlation potentials in density functional theory.", *J. Chem. Phys.* **117**, pp. 11113–11120 (2002).

[82] S. Grimme, "Semiempirical GGA-type density functional constructed with a long-range dispersion correction", *J. Comput. Chem.* **27**, pp. 1787–1799 (2006).

[83] A. Tkatchenko and M. Scheffler, "Accurate molecular van der waals interactions from ground-state electron density and free-atom reference data", *Phys. Rev. Lett.* **102**, pp. 073005 (2009).

[84] S. Grimme, J. Antony, S. Ehrlich, and H. Krieg, "A consistent and accurate ab initio parametrization of density functional dispersion correction (DFT-D) for the 94 elements H-Pu", *J. Chem. Phys.* **132**(15) (2010).

[85] S. Grimme, S. Ehrlich, and L. Goerigk, "Effect of the damping function in dispersion corrected density functional theory", *J. Comput. Chem.* **32**, pp. 1456–1465 (2011).

[86] N. A. Spaldin, "A beginner's guide to the modern theory of polarization", *Journal of Solid State Chemistry* **195**, pp. 2–10 (2012).

[87] K. M. Rabe, C. Ahn, and J.-M. Triscone, *Physics of ferroelectrics : a modern perspective*, Springer Berlin (2007).

[88] C. Michel, J. M. Moreau, G. D. Achenbach, R. Gerson, and W. J. James, "The atomic structure of $BiFeO_3$", *Solid State Communications* **7**, pp. 701–704 (1969).

[89] R. Car and M. Parrinello, "Unified approach for molecular dynamics and density-functional theory", *Phys. Rev. Lett.* **55**, pp. 2471–2474 (1985).

[90] M. Born and R. Oppenheimer, "Zur quantentheorie der molekeln", *Annalen der Physik* **389**, pp. 457–484 (1927).

[91] T. D. Kühne, M. Iannuzzi, M. Del Ben, V. V. Rybkin, P. Seewald, F. Stein, T. Laino, R. Z. Khaliullin, O. Schütt, F. Schiffmann, D. Golze, J. Wilhelm, S. Chulkov, M. H. Bani-Hashemian, V. Weber, U. Borštnik, M. Taillefumier, A. S. Jakobovits, A. Lazzaro, H. Pabst, T. Müller, R. Schade, M. Guidon, S. Andermatt, N. Holmberg, G. K. Schenter, A. Hehn, A. Bussy, F. Belleflamme, G. Tabacchi, A. Glöß, M. Lass,

I. Bethune, C. J. Mundy, C. Plessl, M. Watkins, J. VandeVondele, M. Krack, and J. Hutter, "Cp2k: An electronic structure and molecular dynamics software package - quickstep: Efficient and accurate electronic structure calculations", *J. Chem. Phys.* **152**, pp. 194103 (2020).

[92] G. Kresse and J. Furthmüller, "Efficient iterative schemes for ab initio total-energy calculations using a plane-wave basis set", *Phys. Rev. B* **54**, pp. 11169–11186 (1996).

[93] G. Kresse and J. Furthmüller, "Efficiency of ab-initio total energy calculations for metals and semiconductors using a plane-wave basis set", *Comput. Mater. Sci.* **6**, pp. 15–50 (1996).

[94] H. Schmid, "Multi-ferroic magnetoelectrics", *Ferroelectrics* **162**, pp. 317–338 (1994).

[95] T. Shimada, T. Matsui, T. Xu, K. Arisue, Y. Zhang, J. Wang, and T. Kitamura, "Multiferroic nature of intrinsic point defects in $BiFeO_3$: A hybrid Hartree-Fock density functional study", *Phys. Rev. B* **93**, pp. 174107 (2016).

[96] F. Kubel and H. Schmid, "Structure of a ferroelectric and ferroelastic monodomain crystal of the perovskite $BiFeO_3$", *Acta Crystallographica Section B* **46**(6), pp. 698–702 (1990).

[97] J. B. Neaton, C. Ederer, U. V. Waghmare, N. A. Spaldin, and K. M. Rabe, "First-principles study of spontaneous polarization in multiferroic $BiFeO_3$", *Phys. Rev. B* **71**, pp. 014113 (2005).

[98] A. M. Kadomtseva, A. K. Zvezdin, Y. F. Popov, A. P. Pyatakov, and G. P. Vorobév, "Space-time parity violation and magnetoelectric interactions in antiferromagnets", *Journal of Experimental and Theoretical Physics Letters* **79**, pp. 571–581 (2004).

[99] T. Choi, S. Lee, Y. J. Choi, V. Kiryukhin, and S.-W. Cheong, "Switchable ferroelectric diode and photovoltaic effect in $BiFeO_3$", *Science* **324**, pp. 63–66 (2009).

[100] G. Chen, J. Chen, W. Pei, Y. Lu, Q. Zhang, Q. Zhang, and Y. He, "Bismuth ferrite materials for solar cells: Current status and prospects", *Materials Research Bulletin* **110**, pp. 39–49 (2019).

[101] S. M. Young, F. Zheng, and A. M. Rappe, "First-principles calculation of the bulk photovoltaic effect in bismuth ferrite", *Phys. Rev. Lett.* **109**, pp. 236601 (2012).

[102] P. Machado, I. Caño, C. Menéndez, C. Cazorla, H. Tan, I. Fina, M. Campoy-Quiles, C. Escudero, M. Tallarida, and M. Coll, "Enhancement of phase stability

and optoelectronic performance of $BiFeO_3$ thin films via cation co-substitution", *J. Mater. Chem. C* **9**, pp. 330–339 (2021).

[103] P. Machado, M. Scigaj, J. Gazquez, E. Rueda, A. Sánchez-Díaz, I. Fina, M. Gibert-Roca, T. Puig, X. Obradors, M. Campoy-Quiles, and M. Coll, "Band gap tuning of solution-processed ferroelectric perovskite $BiFe_{1-x}Co_xO_3$ thin films", *Chemistry of Materials* **31**, pp. 947–954 (2019).

[104] S. Y. Yang, L. W. Martin, S. J. Byrnes, T. E. Conry, S. R. Basu, D. Paran, L. Reichertz, J. Ihlefeld, C. Adamo, A. Melville, Y.-H. Chu, C.-H. Yang, J. L. Musfeldt, D. G. Schlom, J. W. Ager, and R. Ramesh, "Photovoltaic effects in $BiFeO_3$", *Applied Physics Letters* **95**, pp. 062909 (2009).

[105] S. Li, Y.-H. Lin, B.-P. Zhang, J.-F. Li, and C.-W. Nan, "$BiFeO_3/TiO_2$ core-shell structured nanocomposites as visible-active photocatalysts and their optical response mechanism", *Journal of Applied Physics* **105**, pp. 054310 (2009).

[106] J. He, R. Guo, L. Fang, W. Dong, F. Zheng, and M. Shen, "Characterization and visible light photocatalytic mechanism of size-controlled $BiFeO_3$ nanoparticles", *Materials Research Bulletin* **48**, pp. 3017–3024 (2013).

[107] W. Ji, K. Yao, Y.-F. Lim, Y. C. Liang, and A. Suwardi, "Epitaxial ferroelectric $BiFeO_3$ thin films for unassisted photocatalytic water splitting", *Applied Physics Letters* **103**, pp. 062901 (2013).

[108] C. Ponraj, V. G, and J. Daniel, "A review on the visible light active $BiFeO_3$ nanostructures as suitable photocatalyst in the degradation of different textile dyes", *Environmental Nanotechnology, Monitoring Management* **7**, pp. 110–120 (2017).

[109] X.-Z. Deng, C. Song, Y.-L. Tong, G. Yuan, F. Gao, D.-Q. Liu, and S.-T. Zhang, "Enhanced photocatalytic efficiency of $C_3N_4/BiFeO_3$ heterojunctions: the synergistic effects of band alignment and ferroelectricity", *Phys. Chem. Chem. Phys.* **20**, pp. 3648–3657 (2018).

[110] F. Mushtaq, X. Chen, M. Hoop, H. Torlakcik, E. Pellicer, J. Sort, C. Gattinoni, B. J. Nelson, and S. Pané, "Piezoelectrically enhanced photocatalysis with $BiFeO_3$ nanostructures for efficient water remediation", *iScience* **4**, pp. 236–246 (2018).

[111] S. Khoomortezaei, H. Abdizadeh, and M. R. Golobostanfard, "Triple layer heterojunction $WO_3/BiVO_4/BiFeO_3$ porous photoanode for efficient photoelectrochemical water splitting", *ACS Applied Energy Materials* **2**, pp. 6428–6439 (2019).

[112] A. Haruna, I. Abdulkadir, and S. O. Idris, "Photocatalytic activity and doping effects of $BiFeO_3$ nanoparticles in model organic dyes", *Heliyon* **6**, pp. e03237 (2020).

[113] S. Khoomortezaei, H. Abdizadeh, and M. R. Golobostanfard, "Ferro-photocatalytic enhancement of photoelectrochemical water splitting using the $WO_3/BiFeO_3$ heterojunction", *Energy & Fuels* **35**, pp. 9623–9634 (2021).

[114] A. Kolivand and S. Sharifnia, "Enhanced photocatalytic hydrogen evolution from water splitting by Z-scheme $CdS/BiFeO_3$ heterojunction without using sacrificial agent", *International Journal of Energy Research* **45**, pp. 2739–2752 (2021).

[115] G. Huang, G. Zhang, Z. Gao, J. Cao, D. Li, H. Yun, and T. Zeng, "Enhanced visible-light-driven photocatalytic activity of $BiFeO_3$ via electric-field control of spontaneous polarization", *Journal of Alloys and Compounds* **783**, pp. 943–951 (2019).

[116] D. Sando, C. Carrétéro, M. N. Grisolia, A. Barthélémy, V. Nagarajan, and M. Bibes, "Revisiting the optical band gap in epitaxial $BiFeO_3$ thin films", *Advanced Optical Materials* **6**, pp. 1700836 (2018).

[117] L. Peng, H. Deng, J. Tian, Q. Ren, C. Peng, Z. Huang, P. Yang, and J. Chu, "Influence of Co doping on structural, optical and magnetic properties of $BiFeO_3$ films deposited on quartz substrates by sol–gel method", *Applied Surface Science* **268**, pp. 146–150 (2013).

[118] S. J. A. Moniz, R. Quesada-Cabrera, C. S. Blackman, J. Tang, P. Southern, P. M. Weaver, and C. J. Carmalt, "A simple, low-cost CVD route to thin films of $BiFeO_3$ for efficient water photo-oxidation", *J. Mater. Chem. A* **2**, pp. 2922–2927 (2014).

[119] D. Cao, Z. Wang, Nasori, L. Wen, Y. Mi, and Y. Lei, "Switchable charge-transfer in the photoelectrochemical energy-conversion process of ferroelectric $BiFeO_3$ photoelectrodes", *Angewandte Chemie International Edition* **53**, pp. 11027–11031 (2014).

[120] L. Wang, T. Maxisch, and G. Ceder, "Oxidation energies of transition metal oxides within the GGA + U framework", *Phys. Rev. B* **73**, pp. 195107 (2006).

[121] R. Grau-Crespo, F. Corà, A. A. Sokol, N. H. de Leeuw, and C. R. A. Catlow, "Electronic structure and magnetic coupling in $FeSbO_4$: A DFT study using hybrid functionals and GGA + U methods", *Phys. Rev. B* **73**, pp. 035116 (2006).

[122] C. Collins, M. S. Dyer, A. Demont, P. A. Chater, M. F. Thomas, G. R. Darling, J. B. Claridge, and M. J. Rosseinsky, "Computational prediction and experimental confirmation of B-site doping in $YBa_2Fe_3O_8$", *Chem. Sci.* **5**, pp. 1493–1505 (2014).

[123] I. Lyubutin, A. Gavriliuk, and V. Struzhkin, "High-spin-low-spin transition and the sequence of the phase transformations in the $BiFeO_3$ crystal at high pressures", *JETP Letters* **88**, pp. 524–530 (2008).

[124] K. Oka, M. Azuma, W.-t. Chen, H. Yusa, A. A. Belik, E. Takayama-Muromachi, M. Mizumaki, N. Ishimatsu, N. Hiraoka, M. Tsujimoto, M. G. Tucker, J. P. Attfield, and Y. Shimakawa, "Pressure-induced spin-state transition in $BiCoO_3$", *Journal of the American Chemical Society* **132**, pp. 9438–9443 (2010).

[125] J. Ray, A. K. Biswal, S. Acharya, V. Ganesan, D. K. Pradhan, and P. N. Vishwakarma, "Effect of Co substitution on the magnetic properties of $BiFeO_3$", *Journal of Magnetism and Magnetic Materials* **324**, pp. 4084–4089 (2012).

[126] Y. Fan, Y. Zhou, M. Shen, X. Xu, Z. Wang, W. Mao, J. Zhang, J. Yang, Y. Pu, and X. Li, "Low-spin $Co^{3+}$ make great contributions to the magnetism of $BiFeO_3$", *Journal of Materials Science: Materials in Electronics* **29**, pp. 18593–18599 (2018).

[127] R. Grau-Crespo, S. Hamad, C. R. A. Catlow, and N. H. de Leeuw, "Symmetry-adapted configurational modelling of fractional site occupancy in solids", *Journal of Physics: Condensed Matter* **19**, pp. 256201 (2007).

[128] R. Grau-Crespo and U. Waghmare, *Simulation of Crystals with Chemical Disorder at Lattice Sites, in Molecular Modeling for the Design of Novel Performance Chemicals and Materials* , pp. 303–326, Taylor and Francis (2012).

[129] J. D. Gale and A. L. Rohl, "The general utility lattice program (GULP)", *Molecular Simulation* **29**, pp. 291–341 (2003).

[130] J. D. Gale, "GULP: A computer program for the symmetry-adapted simulation of solids", *J. Chem. Soc., Faraday Trans.* **93**, pp. 629–637 (1997).

[131] N. Metropolis, A. W. Rosenbluth, M. N. Rosenbluth, A. H. Teller, and E. Teller, "Equation of state calculations by fast computing machines", *The Journal of Chemical Physics* **21**, pp. 1087–1092 (1953).

[132] K. T. Butler, C. H. Hendon, and A. Walsh, "Electronic chemical potentials of porous metal–organic frameworks", *Journal of the American Chemical Society* **136**, pp. 2703–2706 (2014).

[133] S. Sharma and M. Kumar, "Band gap tuning and optical properties of $BiFeO_3$ nanoparticles", *Materials Today: Proceedings* **28**, pp. 168–171 (2020).

[134] P. S. V. Mocherla, C. Karthik, R. Ubic, M. S. Ramachandra Rao, and C. Sudakar, "Tunable bandgap in $BiFeO_3$ nanoparticles: The role of microstrain and oxygen defects", *Applied Physics Letters* **103**(2), pp. 022910 (2013).

[135] R. Palai, R. S. Katiyar, H. Schmid, P. Tissot, S. J. Clark, J. Robertson, S. A. T. Redfern, G. Catalan, and J. F. Scott, "$\beta$ phase and $\gamma-\beta$ metal-insulator transition in multiferroic $BiFeO_3$", *Phys. Rev. B* **77**, pp. 014110 (2008).

[136] M. Azuma, S. Niitaka, N. Hayashi, K. Oka, M. Takano, H. Funakubo, and Y. Shimakawa, "Rhombohedral–Tetragonal phase boundary with high Curie temperature in (1-$x$)$BiCoO_3$–$x$$BiFeO_3$ solid solution", *Japanese Journal of Applied Physics* **47**(9), pp. 7579–7581 (2008).

[137] S. D. Midgley, J. O. Taylor, D. Fleitmann, and R. Grau-Crespo, "Molybdenum and sulfur incorporation as oxyanion substitutional impurities in calcium carbonate minerals: A computational investigation", *Chemical Geology* **553**, pp. 119796 (2020).

[138] S. D. Midgley, D. Fleitmann, and R. Grau-Crespo, "Bromate incorporation in calcite and aragonite", *Geochimica et Cosmochimica Acta* **324**, pp. 17–25 (2022).

[139] S. A. T. Redfern, C. M. B. Henderson, B. J. Wood, R. J. Harrison, and K. S. Knight, "Determination of olivine cooling rates from metal-cation ordering", *Nature* **381**(6581), pp. 407–409 (1996).

[140] R. J. Harrison and A. Putnis, "Magnetic properties of the magnetite-spinel solid solution; curie temperatures, magnetic susceptibilities, and cation ordering", *American Mineralogist* **81**, pp. 375–384 (1996).

[141] S. A. T. Redfern, R. J. Harrison, H. St.C. O'Neill, and D. R. Wood, "Thermodynamics and kinetics of cation ordering in $MgAl_2O_4$ spinel up to 1600 C from in situ neutron diffraction", *American Mineralogist* **84**, pp. 299–310 (1999).

[142] R. Grau-Crespo, N. H. de Leeuw, S. Hamad, and U. V. Waghmare, "Phase separation and surface segregation in ceria-zirconia solid solutions", *Proceedings of the Royal Society A: Mathematical, Physical and Engineering Sciences* **467**, pp. 1925–1938 (2011).

[143] A. Cabañas, J. A. Darr, E. Lester, and M. Poliakoff, "A continuous and clean one-step synthesis of nano-particulate $Ce_{1-x}Zr_xO_2$ solid solutions in near-critical water", *Chemical Communications* , pp. 901–902 (2000).

[144] A. Cabañas, J. A. Darr, E. Lester, and M. Poliakoff, "Continuous hydrothermal synthesis of inorganic materials in a near-critical water flow reactor; the one-step synthesis of nano-particulate $Ce_{1-x}Zr_xO_2$ ($x$ =0−1) solid solutions", *J. Mater. Chem.* **11**, pp. 561–568 (2001).

[145] M. Gajdoš, K. Hummer, G. Kresse, J. Furthmüller, and F. Bechstedt, "Linear optical properties in the projector-augmented wave methodology", *Phys. Rev. B* **73**, pp. 045112 (2006).

[146] J. Wu and J. Wang, "Diodelike and resistive hysteresis behavior of heterolayered $BiFeO_3$/ZnO ferroelectric thin films", *Journal of Applied Physics* **108**, pp. 094107 (2010).

[147] S. J. Clark and J. Robertson, "Band gap and schottky barrier heights of multiferroic $BiFeO_3$", *Applied Physics Letters* **90**(13), pp. 132903 (2007).

[148] K. Gelderman, L. Lee, and S. W. Donne, "Flat-band potential of a semiconductor: Using the Mott–Schottky equation", *Journal of Chemical Education* **84**, pp. 685 (2007).

[149] J. Low, C. Jiang, B. Cheng, S. Wageh, A. A. Al-Ghamdi, and J. Yu, "A review of direct Z-scheme photocatalysts", *Small Methods* **1**, pp. 1700080 (2017).

[150] S. Wang, D. Chen, F. Niu, N. Zhang, L. Qin, and Y. Huang, "Pd cocatalyst on sm-doped $BiFeO_3$ nanoparticles: synergetic effect of a pd cocatalyst and samarium doping on photocatalysis", *RSC Adv.* **6**, pp. 34574–34587 (2016).

[151] A. G. A. Nisbet, F. Fabrizi, S. C. Vecchini, M. Stewart, M. G. Cain, T. Hase, P. Finkel, S. Grover, R. Grau-Crespo, and S. P. Collins, "Intrinsic and extrinsic nature of the giant piezoelectric effect in the initial poling of PMN-PT", *Phys. Rev. Materials* **5**, pp. L120601 (2021).

[152] Y. Guo, H. Luo, K. Chen, H. Xu, X. Zhang, and Z. Yin, "Effect of composition and poling field on the properties and ferroelectric phase-stability of $Pb(Mg_{1/3}Nb_{2/3})O_3$–$PbTiO_3$ crystals", *Journal of Applied Physics* **92**, pp. 6134–6138 (2002).

[153] H. Tan, H. Takenaka, C. Xu, W. Duan, I. Grinberg, and A. M. Rappe, "First-principles studies of the local structure and relaxor behavior of $Pb(Mg_{1/3}Nb_{2/3})O_3$-$PbTiO_3$-derived ferroelectric perovskite solid solutions", *Phys. Rev. B* **97**, pp. 174101 (2018).

[154] B. J. Campbell, H. T. Stokes, D. E. Tanner, and D. M. Hatch, "*ISODISPLACE*: a web-based tool for exploring structural distortions", *Journal of Applied Crystallography* **39**, pp. 607–614 (2006).

[155] R. D. King-Smith and David Vanderbilt, "Theory of polarization of crystalline solids", *Phys. Rev. B* **47**, pp. 1651–1654 (1993).

[156] M. Liu, M. B. Johnston, and H. J. Snaith, "Efficient planar heterojunction perovskite solar cells by vapour deposition", *Nature* **501**, pp. 395–398 (2013).

[157] J. Christians, P. Schulz, J. Tinkham, T. Schloemer, S. Harvey, B. Tremolet de Villers, A. Sellinger, J. Berry, and J. Luther, "Tailored interfaces of unencapsulated perovskite solar cells for >1,000 hour operational stability", *Nature Energy* **3**, pp. 68–74 (2018).

[158] Y. Hassan, J. Park, M. Crawford, A. Sadhanala, J. Lee, J. Sadighian, E. Mosconi, R. Shivanna, E. Radicchi, M. Jeong, C. Yang, H. Choi, S. H. Park, M. H. Song, F. Angelis, C. Wong, R. Friend, B. R. Lee, and H. Snaith, "Ligand-engineered bandgap stability in mixed-halide perovskite LEDs", *Nature* **591**, pp. 72–77 (2021).

[159] J. Jeong, M. Kim, J. Seo, H. Lu, P. Ahlawat, A. Mishra, Y. Yang, M. Hope, F. Eickemeyer, M. Kim, Y. Yoon, I. Choi, B. Darwich, S. Choi, Y. Jo, J. Lee, B. Walker, S. Zakeeruddin, L. Emsley, and J. Y. Kim, "Pseudo-halide anion engineering for -fapbi3 perovskite solar cells", *Nature* **592**, pp. 1–5 (2021).

[160] E. Jung, N. Jeon, E. Park, C. Moon, T. Shin, T.-Y. Yang, J. Noh, and J. Seo, "Efficient, stable and scalable perovskite solar cells using poly(3-hexylthiophene)", *Nature* **567**, pp. 511–515 (2019).

[161] J. J. Yoo, S. Wieghold, M. C. Sponseller, M. R. Chua, S. N. Bertram, N. T. P. Hartono, J. S. Tresback, E. C. Hansen, J.-P. Correa-Baena, V. Bulović, T. Buonassisi, S. S. Shin, and M. G. Bawendi, "An interface stabilized perovskite solar cell with high stabilized efficiency and low voltage loss", *Energy Environ. Sci.* **12**, pp. 2192–2199 (2019).

[162] J. J. Yoo, G. Seo, M. R. Chua, T. G. Park, Y. Lu, F. Rotermund, Y.-K. Kim, C. S. Moon, N. J. Jeon, J.-P. Correa-Baena, V. Bulović, S. S. Shin, M. G. Bawendi, and

J. Seo, "Efficient perovskite solar cells via improved carrier management", *Nature* **590**, pp. 587—593 (2021).

[163] N. J. Jeon, J. H. Noh, W. S. Yang, Y. C. Kim, S. Ryu, J. Seo, and S. I. Seok, "Compositional engineering of perovskite materials for high-performance solar cells", *Nature* **517**, pp. 476–480 (2015).

[164] G. M. Dalpian, X.-G. Zhao, L. Kazmerski, and A. Zunger, "Formation and composition-dependent properties of alloys of cubic halide perovskites", *Chemistry of Materials* **31**, pp. 2497–2506 (2019).

[165] M. Senno and S. Tinte, "Mixed formamidinium–methylammonium lead iodide perovskite from first-principles: hydrogen-bonding impact on the electronic properties", *Phys. Chem. Chem. Phys.* **23**, pp. 7376–7385 (2021).

[166] H. Grüninger, M. Bokdam, N. Leupold, P. Tinnemans, R. Moos, G. A. De Wijs, F. Panzer, and A. P. M. Kentgens, "Microscopic (dis)order and dynamics of cations in mixed FA/MA lead halide perovskites", *The Journal of Physical Chemistry C* **125**, pp. 1742–1753 (2021).

[167] E. Menéndez-Proupin, S. Grover, A. L. Montero-Alejo, S. D. Midgley, K. T. Butler, and R. Grau-Crespo, "Mixed-anion mixed-cation perovskite $(FAPbI_3)_{0.875}(MAPbBr_3)_{0.125}$: an ab initio molecular dynamics study", *J. Mater. Chem. A* **10**, pp. 9592–9603 (2022).

[168] J. VandeVondele, M. Krack, F. Mohamed, M. Parrinello, T. Chassaing, and J. Hutter, "Quickstep: Fast and accurate density functional calculations using a mixed gaussian and plane waves approach", *Computer Physics Communications* **167**, pp. 103–128 (2005).

[169] J. VandeVondele and J. Hutter, "Gaussian basis sets for accurate calculations on molecular systems in gas and condensed phases", *The Journal of Chemical Physics* **127**, pp. 114105 (2007).

[170] S. Goedecker, M. Teter, and J. Hutter, "Separable dual-space gaussian pseudopotentials", *Phys. Rev. B* **54**, pp. 1703–1710 (1996).

[171] C. Hartwigsen, S. Goedecker, and J. Hutter, "Relativistic separable dual-space gaussian pseudopotentials from h to rn", *Phys. Rev. B* **58**, pp. 3641–3662 (1998).

[172] M. Krack, "Pseudopotentials for H to Kr optimized for gradient-corrected exchange-correlation functionals", *Theoretical Chemistry Accounts* **114**, pp. 145–152 (2005).

[173] J. VandeVondele and J. Hutter, "An efficient orbital transformation method for electronic structure calculations", *The Journal of Chemical Physics* **118**, pp. 4365–4369 (2003).

[174] V. Weber, J. VandeVondele, J. Hutter, and A. M. N. Niklasson, "Direct energy functional minimization under orthogonality constraints", *The Journal of Chemical Physics* **128**, pp. 084113 (2008).

[175] E. Menéndez-Proupin, S. Grover, A. L. Montero-Alejo, S. D. Midgley, K. T. Butler, and R. Grau-Crespo, "Data supporting mixed-anion mixed-cation perovskite $(FAPbI_3)_{0.875}(MAPbBr_3)_{0.125}$: an ab initio molecular dynamics study", *Repositorio de datos de investigación de la Universidad de Chile* (2021).

[176] M. T. Weller, O. J. Weber, J. M. Frost, and A. Walsh, "Cubic perovskite structure of black formamidinium lead iodide, $\alpha$-$[HC(NH_2)_2]PbI_3$, at 298 K", *The Journal of Physical Chemistry Letters* **6**, pp. 3209–3212 (2015).

[177] A. Jaffe, Y. Lin, C. M. Beavers, J. Voss, W. L. Mao, and H. I. Karunadasa, "High-pressure single-crystal structures of 3D lead-halide hybrid perovskites and pressure effects on their electronic and optical properties", *ACS Central Science* **2**, pp. 201–209 (2016).

[178] X.-G. Zhao, G. M. Dalpian, Z. Wang, and A. Zunger, "Polymorphous nature of cubic halide perovskites", *Phys. Rev. B* **101**, pp. 155137 (2020).

[179] A. Zunger, S.-H. Wei, L. G. Ferreira, and James E. Bernard, "Special quasirandom structures", *Phys. Rev. Lett.* **65**, pp. 353–356 (1990).

[180] N. E. Cusack, *The physics of structurally disordered matter: an introduction*, Hilger Bristol (1988).

[181] M. Brehm, M. Thomas, S. Gehrke, and B. Kirchner, "TRAVIS—a free analyzer for trajectories from molecular simulation", *The Journal of Chemical Physics* **152**, pp. 164105 (2020).

[182] D Ghosh, P. Walsh Atkins, M. S. Islam, A. B. Walker, and C. Eames, "Good vibrations: Locking of octahedral tilting in mixed-cation iodide perovskites for solar cells", *ACS Energy Letters* **2**, pp. 2424–2429 (2017).

[183] A Mattoni, A. Filippetti, and C. Caddeo, "Modeling hybrid perovskites by molecular dynamics", *Journal of Physics: Condensed Matter* **29**, pp. 043001 (2016).

[184] J. Ganguly, *Thermodynamics in Earth and Planetary Sciences*, Springer Berlin, Heidelberg (2008).

[185] M. Prieto, "Thermodynamics of solid solution-aqueous solution systems", *Reviews in Mineralogy and Geochemistry* **70**, pp. 47–85 (2009).

[186] R. F. Moran, D. McKay, P. C. Tornstrom, A. Aziz, A. Fernandes, R. Grau-Crespo, and S. E. Ashbrook, "Ensemble-based modeling of the nmr spectra of solid solutions: Cation disorder in $Y_2(Sn,Ti)_2O_7$", *Journal of the American Chemical Society* **141**, pp. 17838–17846 (2019).

[187] R. Jinnouchi, F. Karsai, and G. Kresse, "On-the-fly machine learning force field generation: Application to melting points", *Phys. Rev. B* **100**, pp. 014105 (2019).

[188] R. Jinnouchi, F. Karsai, C. Verdi, R. Asahi, and G. Kresse, "Descriptors representing two- and three-body atomic distributions and their effects on the accuracy of machine-learned inter-atomic potentials", *The Journal of Chemical Physics* **152**, pp. 234102 (2020).

[189] M. Saliba, T. Matsui, J.-Y. Seo, K. Domanski, J.-P. Correa-Baena, M. K. Nazeeruddin, S. M. Zakeeruddin, W. Tress, A. Abate, A. Hagfeldt, and M. Grätzel, "Cesium-containing triple cation perovskite solar cells: improved stability, reproducibility and high efficiency", *Energy Environ. Sci.* **9**, pp. 1989–1997 (2016).

[190] C. Zhang, Y. Wang, X. Lin, T. Wu, Q. Han, Y. Zhang, and L. Han, "Effects of a site doping on the crystallization of perovskite films", *J. Mater. Chem. A* **9**, pp. 1372–1394 (2021).

[191] K.-L. Hu, M. Kurmoo, Z. Wang, and S. Gao, "Metal–organic perovskites: Synthesis, structures, and magnetic properties of $[C(NH_2)_3][M^{II}(HCOO)_3]$ (M=Mn, Fe, Co, Ni, Cu, and Zn; $C(NH_2)_3$= Guanidinium)", *Chemistry – A European Journal* **15**(44), pp. 12050–12064 (2009).

[192] X.-H. Zhao, X.-C. Huang, S.-L. Zhang, D. Shao, H.-Y. Wei, and X.-Y. Wang, "Cation-dependent magnetic ordering and room-temperature bistability in Azido-Bridged perovskite-type compounds", *Journal of the American Chemical Society* **135**, pp. 16006–16009 (2013).

[193] M.-L. Tong, J. Ru, Y.-M. Wu, X.-M. Chen, H.-C. Chang, K. Mochizuki, and S. Kitagawa, "Cation-templated construction of three-dimensional $\alpha$-Po cubic-type $[M(dca)_3]$ networks. syntheses, structures and magnetic properties of $A[M(dca)_3]$ (dca=dicyanamide; for a=benzyltributylammonium, M=$Mn^{2+}$, $Co^{2+}$;

for a=benzyltriethylammonium, M=$Mn^{2+}$, $Fe^{2+}$)", *New J. Chem.* **27**, pp. 779–782 (2003).

[194] J. Lefebvre, D. Chartrand, and D. B. Leznoff, "Synthesis, structure and magnetic properties of 2-D and 3-D [cation]M[$Au(CN)_2]_3$ (M=Ni,Co) coordination polymers", *Polyhedron* **26**, pp. 2189–2199 (2007).

[195] J. A. Hill, A. L. Thompson, and A. L. Goodwin, "Dicyanometallates as model extended frameworks", *Journal of the American Chemical Society* **138**, pp. 5886–5896 (2016).

[196] Z.-Y. Du, T.-T. Xu, B. Huang, Y.-J. Su, W. Xue, C.-T. He, W.-X. Zhang, and X.-M. Chen, "Switchable guest molecular dynamics in a perovskite-like coordination polymer toward sensitive thermoresponsive dielectric materials", *Angewandte Chemie International Edition* **54**, pp. 914–918 (2015).

[197] H. Boström, M. Senn, and A. Goodwin, "Recipes for improper ferroelectricity in molecular perovskites", *Nature Communications* **9**, pp. 2380 (2018).

[198] H. L. B. Boström, "Tilts and shifts in molecular perovskites", *CrystEngComm* **22**, pp. 961–968 (2020).

[199] K. L. Svane, A. C. Forse, C. P. Grey, G. Kieslich, A. K. Cheetham, A. Walsh, and K. T. Butler, "How strong is the hydrogen bond in hybrid perovskites?", *The Journal of Physical Chemistry Letters* **8**, pp. 6154–6159 (2017).

[200] L.-J. Ji, S. Sun, Y. Qin, K. Li, and W. Li, "Mechanical properties of hybrid organic-inorganic perovskites", *Coordination Chemistry Reviews* **391**, pp. 15–29 (2019).

[201] J. Feng, "Mechanical properties of hybrid organic-inorganic $CH_3NH_3BX_3$ (B = Sn, Pb; X = Br, I) perovskites for solar cell absorbers", *APL Materials* **2**, pp. 081801 (2014).

[202] K. T. Butler, K. Svane, G. Kieslich, A. K. Cheetham, and A. Walsh, "Microscopic origin of entropy-driven polymorphism in hybrid organic-inorganic perovskite materials", *Phys. Rev. B* **94**, pp. 180103 (2016).

[203] G. Kieslich, J. M. Skelton, J. Armstrong, Y. Wu, F. Wei, K. L. Svane, A. Walsh, and K. T. Butler, "Hydrogen bonding versus entropy: Revealing the underlying thermodynamics of the hybrid organic–inorganic perovskite $[CH_3NH_3]PbBr_3$", *Chemistry of Materials* **30**, pp. 8782–8788 (2018).

[204] S. A. Hallweger, C. Kaußler, and G. Kieslich, "The structural complexity of perovskites", *Phys. Chem. Chem. Phys.* **24**, pp. 9196–9202 (2022).

[205] T. Besara, P. Jain, N. S. Dalal, P. L. Kuhns, A. P. Reyes, H. W. Kroto, and A. K. Cheetham, "Mechanism of the order-disorder phase transition, and glassy behavior in the metal-organic framework $[(CH_3)_2NH_2]Zn(HCOO)_3$", *Proceedings of the National Academy of Sciences* **108**, pp. 6828–6832 (2011).

[206] H. L. B. Boström and G. Kieslich, "Influence of metal defects on the mechanical properties of $ABX_3$ perovskite-type metal-formate frameworks", *The Journal of Physical Chemistry C* **125**, pp. 1467–1471 (2021).

[207] I. E. Collings, M. Bykov, E. Bykova, M. Hanfland, S. van Smaalen, L. Dubrovinsky, and N. Dubrovinskaia, "Disorder–order transitions in the perovskite metal–organic frameworks $[(CH_3)_2NH_2][M(HCOO)_3]$ at high pressure", *CrystEngComm* **20**, pp. 3512–3521 (2018).

[208] M. Maczka, Anna Gagor, M. Ptak, D. Stefańska, and A. Sieradzki, "Temperature-dependent studies of a new two-dimensional cadmium dicyanamide framework exhibiting an unusual temperature-induced irreversible phase transition into a three-dimensional perovskite-like framework", *Phys. Chem. Chem. Phys.* **20**, pp. 29951–29958 (2018).

[209] G. Kieslich, S. Kumagai, K. T. Butler, T. Okamura, C. H. Hendon, S. Sun, M. Yamashita, A. Walsh, and A. K. Cheetham, "Role of entropic effects in controlling the polymorphism in formate $ABX_3$ metal–organic frameworks", *Chem. Commun.* **51**, pp. 15538–15541 (2015).

[210] Y. Wu, S. Shaker, F. Brivio, R. Murugavel, P. D. Bristowe, and A. K. Cheetham, "$[Am]Mn(H_2POO)_3$: A new family of hybrid perovskites based on the Hypophosphite Ligand", *Journal of the American Chemical Society* **139**, pp. 16999–17002 (2017).

[211] S. Burger, S. Kronawitter, H. L. B. Boström, J. K. Zareba, and G. Kieslich, "A new polar perovskite coordination network with azaspiroundecane as a-site cation", *Dalton Trans.* **49**, pp. 10740–10744 (2020).

[212] Mirosław Maczka, Anna Gagor, Maciej Ptak, Dagmara Stefańska, Lucyna Macalik, Adam Pikul, and Adam Sieradzki, "Structural, phonon, magnetic and optical properties of novel perovskite-like frameworks of $TriBuMe[M(dca)_3]$ (TriBuMe = tributylmethylammonium; dca = dicyanamide; M = $Mn^{2+}$, $Fe^{2+}$, $Co^{2+}$, $Ni^{2+}$)", *Dalton Trans.* **48**, pp. 13006–13016 (2019).

[213] S. L. Dudarev, G. A. Botton, S. Y. Savrasov, C. J. Humphreys, and A. P. Sutton, "Electron-energy-loss spectra and the structural stability of nickel oxide: An LSDA+U study", *Phys. Rev. B* **57**, pp. 1505–1509 (1998).

[214] W. Li, S. Henke, and A. K. Cheetham, "Research update: Mechanical properties of metal-organic frameworks – influence of structure and chemical bonding", *APL Materials* **2**, pp. 123902 (2014).

[215] W. Li, A. Thirumurugan, P. T. Barton, Z. Lin, S. Henke, H. H.-M. Yeung, M. T. Wharmby, E. G. Bithell, C. J. Howard, and A. K. Cheetham, "Mechanical tunability via hydrogen bonding in metal–organic frameworks with the perovskite architecture", *Journal of the American Chemical Society* **136**, pp. 7801–7804 (2014).

[216] G. Kieslich, S. Kumagai, A. C. Forse, S. Sun, S. Henke, M. Yamashita, C. P. Grey, and A. K. Cheetham, "Tuneable mechanical and dynamical properties in the ferroelectric perovskite solid solution $[NH_3NH_2]_{1x}[NH_3OH]_xZn(HCOO)_3$", *Chem. Sci.* **7**, pp. 5108–5112 (2016).

[217] J.-C. Tan, P. Jain, and A. K. Cheetham, "Influence of ligand field stabilization energy on the elastic properties of multiferroic mofs with the perovskite architecture", *Dalton Trans.* **41**, pp. 3949—3952 (2012).

[218] B. Li, Y. Kawakita, S. Ohira-Kawamura, T. Sugahara, H. Wang, J. Wang, Y. Chen, S. I. Kawaguchi, S. Kawaguchi, K. Ohara, K. Li, D. Yu, R. Mole, T. Hattori, T. Kikuchi, S.-I. Yano, Z. Zhang, Z. Zhang, W. Ren, S. Lin, O. Sakata, K. Nakajima, and Z. Zhang, "Colossal barocaloric effects in plastic crystals", *Nature* **567**, pp. 506—510 (2019).

[219] A. Togo and I. Tanaka, "First principles phonon calculations in materials science", *Scripta Materialia* **108**, pp. 1–5 (2015).

[220] S. Sobczak, P. Ratajczyk, and A. Katrusiak, "High-pressure nucleation of low-density polymorphs", *Chemistry – A European Journal* **27**, pp. 7069–7073 (2021).

[221] M. Maczka, A. Gagor, M. Ptak, W. Paraguassu, T. A. da Silva, A. Sieradzki, and A. Pikul, "Phase transitions and coexistence of magnetic and electric orders in the methylhydrazinium metal formate frameworks", *Chemistry of Materials* **29**, pp. 2264–2275 (2017).

[222] S. Burger, S. Grover, K. T. Butler, H. L. B. Boström, R. Grau-Crespo, and G. Kieslich, "Tilt and shift polymorphism in molecular perovskites", *Mater. Horiz.* **8**, pp. 2444–2450 (2021).

[223] K. T. Butler, P. Vervoorts, M. G. Ehrenreich, J. Armstrong, J. M. Skelton, and G. Kieslich, "Experimental evidence for vibrational entropy as driving parameter of flexibility in the metal–organic framework ZIF-4(Zn)", *Chemistry of Materials* **31**, pp. 8366–8372 (2019).

[224] J. M. Skelton, L. A. Burton, F. Oba, and A. Walsh, "Metastable cubic tin sulfide: A novel phonon-stable chiral semiconductor", *APL Materials* **5**, pp. 036101 (2017).

[225] F. D. Murnaghan, "The compressibility of media under extreme pressures", *Proceedings of the National Academy of Sciences* **30**, pp. 244–247 (1944).

[226] F. Birch, "Finite elastic strain of cubic crystals", *Phys. Rev.* **71**, pp. 809–824 (1947).

[227] G. Feng, D. Gui, and W. Li, "Structural and chemical bonding dependence of mechanical properties in a family of metal-formate coordination polymers", *Crystal Growth & Design* **18**, pp. 4890–4895 (2018).

[228] S. Sun, F. H. Isikgor, Z. Deng, F. Wei, G. Kieslich, P. D. Bristowe, J. Ouyang, and A. K. Cheetham, "Factors influencing the mechanical properties of formamidinium lead halides and related hybrid perovskites", *ChemSusChem* **10**, pp. 3740–3745 (2017).

[229] S. Sun, Y. Fang, G. Kieslich, T. J. White, and A. K. Cheetham, "Mechanical properties of organic–inorganic halide perovskites, $CH_3NH_3PbX_3$ (X = I, Br and Cl), by nanoindentation", *J. Mater. Chem. A* **3**, pp. 18450–18455 (2015).

[230] J. M. Frost, K. T. Butler, F. Brivio, C. H. Hendon, M. van Schilfgaarde, and A. Walsh, "Atomistic origins of high-performance in hybrid halide perovskite solar cells", *Nano Letters* **14**(5), pp. 2584–2590 (2014).

[231] T. Mueller, A. G. Kusne, and R. Ramprasad, *Machine Learning in Materials Science* chapter 4, , pp. 186–273, John Wiley & Sons, Ltd (2016).

[232] G. Pilania, C. Wang, X. Jiang, S. Rajasekaran, and R. Ramprasad, "Accelerating materials property predictions using machine learning", *Scientific reports* **3**, pp. 2810 (2013).

[233] S. D. Midgley, S. Hamad, K. T. Butler, and R. Grau-Crespo, "Bandgap engineering in the configurational space of solid solutions via machine learning: (Mg,Zn)O case study", *The Journal of Physical Chemistry Letters* **12**, pp. 5163–5168 (2021).

[234] J. J. Plata, V. Posligua, A. M. Márquez, J. Fernandez Sanz, and R. Grau-Crespo, "Charting the lattice thermal conductivities of I–III–$VI_2$ chalcopyrite semiconductors", *Chemistry of Materials* **34**, pp. 2833–2841 (2022).

[235] L. Antunes, R. Grau-Crespo, and K. Butler, "Distributed representations of atoms and materials for machine learning", *npj Computational Materials* **8**, pp. 44 (2022).

[236] Y. Hong, B. Hou, H. Jiang, and J. Zhang, "Machine learning and artificial neural network accelerated computational discoveries in materials science", *WIREs Computational Molecular Science* **10**, pp. e1450 (2020).

[237] A. Agrawal and A. Choudhary, "Deep materials informatics: Applications of deep learning in materials science", *MRS Communications* **9**, pp. 1–14 (2019).

[238] T. Xie and J. C. Grossman, "Crystal graph convolutional neural networks for an accurate and interpretable prediction of material properties", *Phys. Rev. Lett.* **120**, pp. 145301 (2018).

[239] C. Chen, W. Ye, Y. Zuo, C. Zheng, and S. P. Ong, "Graph networks as a universal machine learning framework for molecules and crystals", *Chemistry of Materials* **31**, pp. 3564–3572 (2019).

[240] K. Choudhary, K. Garrity, A. Reid, B. DeCost, A. Biacchi, A. Hight Walker, Z. Trautt, J. Hattrick-Simpers, A. Kusne, A. Centrone, A. Davydov, J. Jiang, R. Pachter, G. Cheon, E. Reed, A. Agrawal, X. Qian, V. Sharma, H. Zhuang, and F. Tavazza, "The joint automated repository for various integrated simulations (JARVIS) for data-driven materials design", *npj Computational Materials* **6**, pp. 1–13 (2020).